The Later Stages of Transition over a NACA0018 Airfoil at a Low Reynolds Number

by

Thomas M. Kirk

A thesis
presented to the University of Waterloo
in fulfilment of the
thesis requirement for the degree of
Master of Applied Science
in
Mechanical Engineering

Waterloo, Ontario, Canada, 2014

© Thomas M. Kirk 2014

I hereby declare that I am the sole author of this thesis. This is a true copy of the thesis, including any required final revisions, as accepted by my examiners.

I understand that my thesis may be made electronically available to the public.

Abstract

The later stages of separated shear layer transition within separation bubbles developing over a NACA0018 airfoil operating at a chord Reynolds number of 10^5 and at angles of attack of 0, 5, 8, and 10 degrees were investigated experimentally in a wind tunnel. Several experimental tools, including a rake of six boundary-layer hot-wire anemometers, were used to perform measurements over the model.

Novel high-speed flow visualization performed with a smoke-wire placed within the separated shear layer showed that roll-up vortices are shed within separation bubbles forming on the suction side of the airfoil. The structures were found to convect downstream and eventually break down during laminar-to-turbulent transition. Top view visualizations revealed that, at angles of attack of 0, 5, and 8 degrees, roll-up vortices form coherently across the span and undergo significant spanwise deformations prior to breaking down. At angles of attack of 5 and 8 degrees, rows of streamwise-oriented structures were observed to form during vortex breakdown.

Statistics regarding the formation and development of shear layer roll-up vortices were extracted from high-speed flow visualization sequences and compared to the results of boundary layer measurements. It was found that, on the average, roll-up vortices form following the initial exponential growth of unstable disturbances within the separated shear layer and initiate the later stages of transition. The onset of these nonlinear stages was found to occur when the amplitude of velocity disturbances reached approximately 10% of the free-stream velocity. The rate of vortex shedding was found to fall within the frequency band of the unstable disturbances and lie near the central frequency of this band. The formation of vortices has been linked to the generation of harmonics of these unstable disturbances in velocity signals acquired ahead of mean transition. Once shed, vortices were found to drift at speeds between 33% and 44% of the edge velocity.

Vortex merging at an angle of attack of 5° was investigated. It was found that the majority of roll-up vortices proceed to merge with either one or two other vortices. Vortex merging between two and three vortices was found to occur periodically in a process similar to vortex merging in plane mixing layers undergoing subharmonic forcing of the most amplified disturbance.

The flapping motion of the separated shear layer was investigated by performing a cross-correlation analysis on the high-speed flow visualization sequences to extract vertical displacement signals of the smoke within the shear layer. The frequency of flapping was found to correspond to the unstable disturbance band. At an angle of attack of 5°, it was found that the separated shear layer has a low-frequency component of flapping that matches a strong peak in velocity and surface pressure spectra that lies outside the unstable disturbance frequency band.

The spanwise development of disturbances was assessed in the aft portion of the separation bubbles by performing a cross-correlation analysis on signals acquired simultaneously across the span with the rake of hot-wires. The spanwise correlations between signals was found to be well-correlated ahead of shear layer roll-up, after which disturbances became rapidly uncorrelated ahead of mean reattachment. These results were found to be linked to the coherent roll-up and subsequent breakdown of roll-up vortices.

Acknowledgements

My supervisor, Serhiy Yarusevych, deserves a big thanks for all his enthusiasm, insight, help, and patience throughout my Master's. I have never worked with anyone more thorough. While I still have a lot to learn and improve on, he has been a great influence.

I would like to thank my fellow low-speed aerodynamics graduate student colleagues, Holly Neatby and Andrew Lambert, for all their help and cooperation throughout the past couple years.

Thank you, Chris Morton, our resident Ph.D. student, for all those lengthy discussions on signal processing and fluid mechanics. While some of the fruits of our discussions did not ultimately make it into this document, they were very helpful and still have potential.

I would like to thank my fellow graduate students, Manpreet Bansal, Brian Kettlewell, David Sommer, Jeff McClure, Sahil Mahey, and Eugene Zivkov, for your companionship and for exposing me to your areas of research.

Thank you, laboratory staff members, Jim Merli, Jason Benninger, and Neil Griffet, for all your technical and logistical help regarding the experimental facility, equipment, and airfoil model. Student shop technicians, Mark Kuntz, Phil Laycock, and Andrew Urschel, thank you for all your help with the fabrication of parts used in my experiments.

Bülent Yaniktepe, thank you for all your help with flow visualization during your visit in 2013.

I would like to thank research group alumni, Michael Boutilier and Ryan Gerakopulos, for all their help at different stages of this project. Also, Ryan, thank you for developing the top notch airfoil model.

Lastly, I would like to thank the Natural Sciences and Engineering Research Council of Canada and Bombardier Aerospace for their financial support and interest in this investigation.

Dedication

I would like to dedicate this thesis to my mother, Laura, my father, John, and, my sister, Anna. Despite the relative occultness of this research area, you have each shown enthusiasm and have been extremely supportive and understanding since I began this project over two years ago.

I would also like to dedicate this work to my family in Buenos Aires, especially my grandparents, Ebe and Martha, who despite the distance are always there for me, and my grandfather in Winnipeg, Bryan, who is always keen to hear what I'm up to and shares a love of aviation.

To each of you, I couldn't be more grateful.

Table of Contents

List of Tables **xiii**

List of Figures **xvii**

Nomenclature **xix**

1 Introduction **1**

2 Background **5**
2.1 Airfoil Operation at Low Reynolds numbers 5
2.2 Structure of the Laminar Separation Bubble 7
2.3 Separated Shear Layer Transition 9
2.3.1 The Early Stage of Transition 10
2.3.2 The Later Stages of Transition 12

3 Experimental Methodology **17**
3.1 Experimental Setup 18
3.1.1 University of Waterloo Low Speed Wind Tunnel 18
3.1.2 NACA0018 Airfoil Model 19
3.2 Measurement Techniques 21
3.2.1 Static Surface Pressure Measurements 22
3.2.2 Fluctuating Surface Pressure Measurements 22
3.2.3 Velocity Measurements 23
3.3 Flow Visualization 25

4 Results **29**
4.1 Flow Visualization 29
4.1.1 Upstream Smoke-Wire Flow Visualization 30
4.1.2 Separation Bubble Flow Visualizations 30

4.2 Streamwise Flow Development 37
4.2.1 High-Speed Flow Visualization 38
4.2.2 Boundary Layer Measurements 47
4.2.3 Vortex Merging 71
4.2.4 Shear Layer Flapping 79
4.3 Spanwise Flow Development 81
4.3.1 High-Speed Top View Flow Visualization 81
4.3.2 Cross-Correlation Analysis 88

5 Conclusions **95**

6 Recommendations **99**

REFERENCES **103**

APPENDICES **113**

A Experimental Uncertainty **115**
A.1 Uncertainty in Experimental Setup 115
A.2 Uncertainty in Flow Visualizations 117
A.3 Uncertainty in Static Pressure Measurements 118
A.4 Uncertainty in Microphone Measurements 119
A.5 Uncertainty in Velocity Measurements 120
A.6 Uncertainty in Determining the Central Frequency of the Unstable Disturbance Growth Frequency Band 122
A.7 Uncertainty in Estimating Cross-Correlation Coefficients 122

B Influence of Experimental Setup **125**
B.1 Intrusiveness of Flow Visualization 125
B.2 Intrusiveness of Velocity Measurements 131
B.3 Effect of Wind Tunnel Free-stream 134

List of Tables

3.1 Model solid blockage ratio 21
3.2 Streamwise and vertical positions of the smoke-wire in the second configuration 26

4.1 Summary of data obtained from side view high-speed visualizations 47
4.2 Mean separation, transition, and reattachment locations and uncertainty estimated from surface pressure distributions 49
4.3 Estimated central frequency and bandwidth of unstable disturbance band . 64
4.4 Frequency and relative frequency of roll-up associated of vortex merging events associated to instances of shear layer roll-up for $\alpha = 5°$. 75

A.1 Summary of measurement uncertainty estimates 116

List of Figures

2.1 Flow regimes of airfoils operating at low Reynolds numbers 6
2.2 Time-averaged laminar separation bubble representation 8
2.3 Typical suction side surface pressure distribution over an airfoil with a laminar separation bubble. 9

3.1 University of Waterloo adaptive-wall wind tunnel 18
3.2 Airfoil model and definition of coordinate systems 19
3.3 Locations of microphones embedded into NACA0018 airfoil model 20
3.4 Isometric view of positioning traverse and hot-wire probes 24
3.5 Hot-wire placement in the rake 24
3.6 Schematics of smoke-wire flow visualization setups 25
3.7 Schematic of streamwise smoke-wire flow visualization laser sheet setup . . 27

4.1 Upstream smoke-wire flow visualization for $\alpha = 0°$ 31
4.2 Upstream smoke-wire flow visualization for $\alpha = 5°$ 31
4.3 Upstream smoke-wire flow visualization for $\alpha = 8°$ 32
4.4 Upstream smoke-wire flow visualization for $\alpha = 10°$ 32
4.5 Side view separation bubble visualization for $\alpha = 0°$ 33
4.6 Side view separation bubble visualization for $\alpha = 5°$ 33
4.7 Side view separation bubble visualization for $\alpha = 8°$ 33
4.8 Side view separation bubble visualization for $\alpha = 10°$ 34
4.9 Top view separation bubble visualization for $\alpha = 0°$ 35
4.10 Top view separation bubble visualization for $\alpha = 5°$ 35
4.11 Top view separation bubble visualization for $\alpha = 8°$ 36
4.12 Top view separation bubble visualization for $\alpha = 10°$ 36
4.13 Sequence of high-speed images displaying vortex shedding at $\alpha = 0°$. 39
4.14 Sequence of high-speed images displaying triple vortex merging at $\alpha = 5°$. . 40
4.15 Sequence of high-speed images displaying vortex shedding at $\alpha = 8°$. 41
4.16 Sequence of high-speed images displaying vortex shedding at $\alpha = 10°$. . . . 42

4.17 Example of breaking wave used in streamwise roll-up position estimation and histogram of x_{roll}/c at $\alpha = 5°$. 44
4.18 Vortex shedding frequency and vortex shedding Strouhal number plotted against α 45
4.19 Drift speed of vortices nondimensionalized by free-stream and edge velocity 46
4.20 Model surface pressure distributions 48
4.21 Mean separation, transition, and reattachment locations and separation bubble length plotted against α 50
4.22 Mean and RMS velocity profiles for $\alpha = 5°$ 52
4.23 Mean and RMS velocity profiles for $\alpha = 8°$ 53
4.24 Streamwise development of boundary layer parameters 55
4.25 Sreamwise development of RMS velocity and RMS fluctuating surface pressure 58
4.26 Velocity and surface pressure spectra for $\alpha = 0°$ 61
4.27 Velocity and surface pressure spectra for $\alpha = 5°$ 62
4.28 Velocity and surface pressure spectra for $\alpha = 8°$ 63
4.29 Comparison between the vortex shedding frequency and central disturbance band frequency 66
4.30 Histograms showing the relative frequency distribution of the period between consecutive instances of shear layer roll-up 68
4.31 Cross-correlation coefficient functions computed from simultaneously acquired surface pressure signals 69
4.32 Normalized accumulated time lag computed from cross-correlations of surface pressure signals 70
4.33 Sequence of high-speed flow visualizations at $\alpha = 5°$ showing the merging of two roll-up vortices. 72
4.34 Sequence of high-speed flow visualizations at $\alpha = 5°$ showing the merging of three roll-up vortices. 73
4.35 Sequence of high-speed flow visualizations at $\alpha = 5°$ showing a vortex that does not merge after formation. 74
4.36 Estimated roll-up x/c locations plotted against time for $\alpha = 5°$. Events associated to each instance of roll-up are marked. 76
4.37 RMS velocity of unfiltered and bandpass filtered signals for $\alpha = 5°$ 78
4.38 Spectra computed from vertical displacement signals of smoke within the separated shear layer upstream of roll-up 80
4.39 Sequence of top view high-speed flow visualizations acquired at $\alpha = 0°$ . . 83
4.40 Sequence of top view high-speed flow visualizations acquired at $\alpha = 5°$ . . 85
4.41 Sequence of top view high-speed flow visualizations acquired at $\alpha = 8°$ . . 86

4.42 Cross-correlation coefficient functions computed from velocity signals acquired simultaneously across the rake of hot-wires at $\alpha = 0°$ 89
4.43 Cross-correlation coefficient functions computed from velocity signals acquired simultaneously across the rake of hot-wires at $\alpha = 5°$ 90
4.44 Cross-correlation coefficient functions computed from velocity signals acquired simultaneously across the rake of hot-wires at $\alpha = 8°$ 91
4.45 Correlation coefficients computed from velocity signals acquired simultaneously with the rake of hot-wires 93

A.1 Standard deviations of cross-correlation coefficients computed individually from the 256 windows used in computing the averaged value of $\rho(\tau)$ 123

B.1 Effect of smoke-wire separation bubble visualization on pressure distribution 126
B.2 Effect of smoke-wire separation bubble visualization on RMS fluctuating surface pressure 128
B.3 Effect of smoke-wire separation bubble visualization on surface pressure spectra 130
B.4 Influence of the rake of hot-wire probes on surface pressure distributions when placed within the boundary layer. 133
B.5 Influence of the rake of hot-wire probes on fluctuating surface pressure spectra when placed within the boundary layer at $\alpha = 5°$ 134
B.6 Spectra of hot-wire velocity measurements obtained within the free-stream of the empty test section and within the test section with the fan off 135

Nomenclature

B	model blockage ratio, computed from the quotient of projected area of model with and without end plates onto a streamwise normal plane and test section cross sectional area
b	spanwise distance between the end plates
C_p	model pressure coefficient, $C_p = (P - P_\infty)/q_\infty$
c	chord length
d	projected model height
E_{pp}	normalized energy spectrum of surface pressure fluctuations
E_{uu}	normalized energy spectrum of streamwise velocity component
f	frequency, Hz
f_{filter}	range of passband of band-pass filter, Hz
$f_{shedding}$	vortex shedding frequency, Hz
f_0	central frequency of unstable disturbance band
H	boundary layer shape factor, $H = \delta^*/\theta$
L	separation bubble length, $L = x_R - x_S$
P	mean surface pressure at a location on the model surface
P_w	mean surface pressure at a location on the test section wall
P_∞	free-stream static pressure
p	fluctuating component of pressure
p'	root-mean-square surface pressure
q_∞	free-stream dynamic pressure, $q_\infty = \frac{1}{2}\rho U_\infty^2$
Re_c	chord Reynolds number, $Re_c = U_\infty c/\nu$
$St_{shedding}$	Strouhal number based on rate of vortex shedding, projected model height and free-stream velocity, $St = f_{shedding} d/U_\infty$
U	time-averaged streamwise component of velocity
U_c	convection speed of pressure fluctuations
U_{drift}	drift speed of shear layer vortices
U_e	edge velocity in mean velocity profile

U_e^*	edge velocity in laminar portion of separation bubble, $U_e^* \approx U_\infty\sqrt{1-C_p}$
U_∞	free-stream velocity
u	streamwise component of velocity fluctuations
u_f	u of band-pass filtered signals
u', u'_f	root-mean-square of u and u_f
t	time
T_{roll}	period between consecutive instances of shear layer roll-up
X	distance measured from the model axle in the streamwise direction
x_{roll}	x location of onset of shear layer roll-up
x_R	mean x location of reattachment obtained from surface pressure distributions
x_S	mean x location of separation obtained from surface pressure distributions
x_T	mean x location of transition obtained from surface pressure distributions
Y	vertical distance from the model axle
y	distance from the model surface
Z	spanwise distance from the model mid-span plane towards the wind tunnel Plexiglas side
α	angle of attack, degrees
Δy	discrete velocity profile point spacing
δ_e	edge thickness, i.e., the y location at which $U = U_e$
δ^*	boundary layer displacement thickness, $\delta^* = \int_0^{\delta_e}(1 - U/U_e)\mathrm{dy}$
ν	kinematic viscosity
ρ	density of air in the test section
$\rho(\tau)$	cross-correlation coefficient function
$\rho(0)$	cross-correlation coefficient
τ	time lag
τ^*	accumulated time lag
θ	boundary layer momentum thickness, $\theta = \int_0^{\delta_e} U/U_e(1 - U/U_e)\mathrm{dy}$

Chapter 1

Introduction

The aerodynamic performance of airfoils operating at low chord Reynolds numbers (i.e. $10^4 < Re_c < 10^5$) is an important consideration in the design of unmanned aerial vehicles (UAVs), micro-air vehicles (MAVs), and small wind turbines [1–3]. At this range of Reynolds numbers, a laminar boundary layer developing over the suction side of an airfoil is likely to separate closer to the leading edge, while at larger Reynolds numbers this may occur closer to the trailing edge within a turbulent boundary layer [2]. The effect of flow separation results in a reduction of the lift-to-drag ratio through lowering of lift and increasing drag [2]. This decrease in performance has led to the development of flow control techniques, which utilize active or passive methods to reduce the losses experienced at these low Reynolds numbers, e.g. [4, 5]. In some cases, boundary layer separation can also lead to the generation of an undesirable tonal noise produced at the trailing edge of an airfoil [6].

Laminar boundary layer separation over airfoils operating at low Reynolds numbers leads to flow development that may be classified into two regimes. The first regime occurs when the separated flow fails to reattach causing the airfoil to stall. This regime is characterized by a significant performance drop due to a decrease in the lift force produced over the suction side combined with a sharp increase in drag [2]. This decrease in the lift coefficient, C_L, occurs when the angle of attack is increased above a critical angle at which the maximum lift, $C_{L,max}$, is generated causing the airfoil to stall [1]. The second flow regime occurs when the separated flow reattaches, leading to the formation of a separation bubble. The separation bubble regime tends to occur above a critical Reynolds number, where reattachment is possible [1, 2]. The extent and position of the bubble is dependent on airfoil shape, Reynolds number, and angle of attack [2]. In most cases, the presence of a separation bubble results in a reduction in lift through a decrease in suction over the airfoil's upper surface [1]. However, the position of the separation bubble may cause

either an increase or a reduction of the lift slope when compared to thin airfoil theory [7]. In the case where the separation bubble forms sufficiently far downstream towards the trailing edge, aerodynamic performance has been shown to increase when compared to a fully turbulent flow over the airfoil [7]. In contrast, a separation bubble positioned near the leading edge lowers the lift force and results in a lower lift slope, which varies nonlinearly [7]. Furthermore, experimental studies have found that the presence of a separation bubble introduces hysteresis into lift slope curves acquired for airfoils tested in free-streams with low turbulence intensities [8]. The different aspects of airfoils operating at low Reynolds number combined with the complexities introduced by the separation bubble regime make it considerably difficult to model flow development and ultimately aerodynamic performance. Thus, the accurate prediction of performance curves, which account for any nonlinear trends and hysteresis, is the subject of ongoing research aimed at improving aerodynamic design tools [9].

To improve the aerodynamic performance of airfoils operating at low Reynolds numbers, it is important that the laminar-to-turbulent transition process occurring within the separated shear layer be understood [3, 5]. Following separation, a laminar separated shear layer undergoes transition to turbulence. The re-energized shear layer will either remain separated or re-attach to form a redeveloping turbulent boundary layer. The location of transition is an important factor in determining whether the flow reattaches. The initial stage of transition over an airfoil is defined by the exponential growth of disturbances within the separated shear layer linked to an inviscid Kelvin-Helmholtz (KH) instability. This disturbance growth is relatively well understood, and has been shown to be accurately modelled by linear stability theory (LST) [10–12]. However, the stages following this initial disturbance growth ultimately lead to transition, and are still the subject of ongoing research, e.g. [13].

This thesis aims to further investigate the later stages of transition within the separation bubble developing over an airfoil operating at a low Reynolds number. Until this time, studies on airfoils have shown that, following the initial disturbance growth, the separated shear layer tends to roll-up into coherent vortices, which then break down to turbulence [14–17]. These studies have demonstrated that there are notable discrepancies in aspects regarding the formation and development of roll-up vortices. Some investigations have observed highly three-dimensional secondary structures, which form during the breakdown of roll-up vortices, tend to persist past the transition location [14, 18–20], while other studies have found that roll-up vortices break down directly into small-scale turbulence [15, 21]. Shear layer roll-up has been shown to initially occur mostly two-dimensionally [22–26], however, as the roll-up vortices convect downstream, they have been shown to deform significantly across the span prior to breaking down [13, 27]. The formation and development of roll-up vortices has been shown to be dependent upon angle of attack [14, 21], Reynolds number [14], and free-stream

turbulence intensity [14, 15], which is expected due to the influence of these conditions on separation bubble formation. In spite of this, the number of studies investigating this phenomenon are limited to few geometries and a small range of Reynolds numbers and angles of attack. Thus, one of the objectives of the present study is to investigate roll-up vortices developing over a different geometry for a large range of angles of attack.

The instability mechanisms, which drive laminar-to-turbulent transition within laminar separation bubbles, has been the subject of ongoing research focused primarily on flows over airfoils [15, 20] and flat plates [13, 26, 28, 29]. These studies have found that secondary instabilities lead to the deformation and breakdown of roll-up vortices, as well as the generation of organized secondary structures [13, 15, 25]. These instabilities occur locally within the aft portion of separation bubbles, and have been shown to be absolutely unstable independently [13, 29] or in combination [15]. It has been suggested that, while secondary instabilities act locally, they may be part of a global instability framework, which could have have serious implications on the design of flow control systems [30]. Further investigation into these breakdown mechanisms is nevertheless required as different disturbance environments and geometries have been shown to produce markedly distinct results [13]. In particular, experimental studies that investigate these mechanisms over airfoils without characterized disturbance forcing are currently lacking. To this end, this investigation also focuses on the link between roll-up vortices and instability mechanisms investigated in prior studies.

In this work, an experimental investigation on separated shear layer transition is conducted over a NACA0018 airfoil model installed in an open-loop low-speed wind tunnel at the University of Waterloo. The model, which was designed and fabricated by Gerakopulos [31], contains embedded static pressure taps and microphones. Over this geometry, Gerakopulos and Yarusevych [32] demonstrated that surface pressure fluctuation measurements are an effective and efficient method to study the convection and growth of disturbances within the separated shear layer. More recently, Boutilier and Yarusevych [12] investigated the early stage of transition over the same airfoil model by performing in-depth hot-wire velocity measurements. The effect of the experimental setup on the flow was also studied, including the intrusiveness of boundary layer hot-wire probes, and the effect on flow development of endplates and blockage [33]. While the characterization and modelling of the initial disturbance growth is valuable, past studies over this model did not directly observe the roll-up and laminar-to-turbulent transition of the separated shear layer, which forms the basis of the later stages of transition.

This work aims to build upon these previous efforts, and investigate the later stages of separated shear layer transition experimentally over the same NACA0018 model. The primary objectives of this thesis are:

1. To study the formation of roll-up structures and their role in separated shear layer transition within a separation bubble forming over an airfoil by:
   (a) capturing high-speed image sequences of flow visualizations within the separated shear layer, and
   (b) analysing the videos qualitatively and quantitatively.
2. To link the results of the flow visualizations to streamwise and spanwise boundary layer measurements by:
   (a) analysing velocity and surface pressure measurements obtained within the boundary layer through:
      i. a traditional statistical and spectral analysis, and
      ii. the cross-correlation analysis of fluctuating surface pressure signals acquired simultaneously across the chord with embedded microphones and velocity measurements acquired simultaneously across the span with a rake of boundary layer hot-wire probes.

Chapter 2

Background

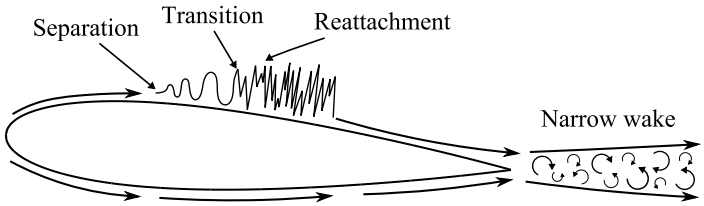
The purpose of this thesis is to investigate the later stages of transition within separation bubbles, which form over a NACA0018 airfoil at low Reynolds numbers. To this end, a brief literature review low Reynolds number flow airfoil operation is presented in Section 2.1. This is followed by a more extensive review on the structure of separation bubbles (Section 2.2), and laminar-to-turbulent transition (Section 2.3) within the separated shear layer.

2.1 Airfoil Operation at Low Reynolds numbers

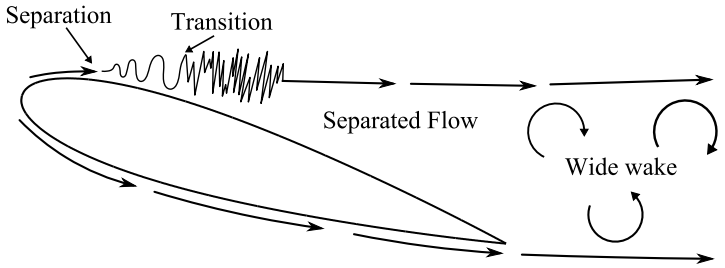
At low chord Reynolds numbers ($Re_c < 10^5$), boundary layer development on the suction side of an airfoil remains laminar past the point of minimum pressure. Downstream, an adverse pressure gradient often leads to boundary layer separation and the formation of a separated shear layer [34]. The laminar separated shear layer is unstable to background disturbances [10] which cause the flow to transition to turbulence after separation. Following transition, the flow may then abide by two regimes.

The first regime (Fig. 2.1a) is defined by the reattachment of the transitioned separated shear layer. The reattachment causes a region of slowly recirculating fluid to form between the separation and reattachment points. Despite the presence of turbulent flow in the aft portion of this region, it is referred to as the laminar separation bubble (LSB) by Gaster [35]. Following the reattachment of the shear layer, a turbulent boundary layer redevelops towards the trailing edge followed by a relatively narrow wake.

The second regime (Fig. 2.1b) occurs when the transitioned separated shear layer fails to reattach, and this causes the airfoil to stall and suffer a significant decline in aerodynamic performance [3]. The stalled airfoil acts similarly to a bluff body and sheds large-scale



(a) Laminar separation bubble regime



(b) Stalled airfoil

Figure 2.1: Flow regimes of airfoils operating at low Reynolds numbers. Reproduced from Yarusevych et al. [36].

vortices, which develop into a wide wake [12, 36, 37]. Despite the lack of reattachment, the laminar separated shear layer still transitions to turbulence. While this thesis does not directly investigate the separated flow regime, it is essential in understanding the low Reynolds number aerodynamics over an airfoil.

The ranges of parameters, such as airfoil angle of attack, Reynolds number, and free-stream turbulence intensity, for when these flow regimes occur are specific to airfoil geometry and test conditions. Also, due to the sensitivity of low Reynolds number flows, differences between the disturbance environments between experimental facilities may be sufficiently large to have an effect on the flow [2]. For higher angles of attack and/or lower Reynolds numbers, the airfoil stalls [1], whereas with decreasing angle of attack and/or increasing Reynolds numbers, the separated shear layer may reattach to form a separation bubble. In the case of the separation bubble regime over airfoils, experimental parametric studies have shown that increasing the Reynolds number and angle of attack causes the separation bubble to shift upstream and shorten in length [7, 14]. Also, separation, transition, and

reattachment locations depend more strongly on the angle of attack than on the chord Reynolds number [7, 14].

The impact of the separation bubble location and length on aerodynamic performance may be significant. For example, Boutilier and Yarusevych [7] showed that the lift coefficient curves of a NACA0018 airfoil are most affected when a separation bubble forms towards the leading edge, due to a substantial decrease in the suction peak. As a result, separation bubbles are often classified as short or long, with short bubbles having a minor effect on performance when compared to long bubbles [38]. The sudden elongation of a short separation bubble, which results in a long bubble or even a stalled airfoil, is known as bubble bursting [35].

The level of free-stream turbulence has a strong effect on the flow development over airfoils. For flow over a Lissaman 7769 airfoil, Mueller et al. [8] found that increasing the free-stream turbulence intensity results in an increase of the maximum lift coefficient and a reduction of the minimum drag. In the case of flow reattachment, an increase in free-stream turbulence intensity leads to a more rapid separated shear layer transition, resulting in a reattachment location further upstream [8]. In addition, Burgmann and Schröder [14] and Hain et al. [20] found that increasing the free-stream turbulence intensity causes the separation location to move further downstream, and reduces the mean flow bubble height. Overall, a shorter separation bubble caused by increased free-stream turbulence intensity causes improved airfoil aerodynamic performance [8]. In contrast, for the stalled airfoil regime, an increase in the drag coefficient was observed when raising the turbulence intensity [8]. Furthermore, airfoil lift and drag curves subjected to low free-stream disturbances have been shown to be affected by hysteresis, which decreases in effect with increasing free-stream turbulence intensity [8, 39].

2.2 Structure of the Laminar Separation Bubble

Attached flow over airfoils operating at low Reynolds numbers is defined by the presence of an LSB on the suction side [2]. Despite the name, laminar-to-turbulent transition is a crucial process within an LSB. Also, while LSBs are naturally unsteady phenomena, they are commonly represented by a time-averaged velocity field. Figure 2.2, originally presented by Horton [40], shows a commonly accepted time-averaged velocity field illustration of a separation bubble forming over the upper surface of an airfoil. Initially, a laminar boundary layer is accelerated away from the leading edge. Once the boundary layer reaches beyond the point of minimum pressure, an adverse pressure gradient causes the flow to separate [34, 35]. The separation point may be estimated based on the time-averaged streamwise velocity gradient at the wall ($\partial U/\partial y|_{wall} = 0$) denoting zero wall shear stress [41]. After separation, a

laminar separated shear layer develops above a region of recirculating fluid. The shear layer is sensitive to small-amplitude background disturbances, which are amplified downstream until the flow transitions. Following transition, the re-energized turbulent shear layer reattaches downstream, where a turbulent boundary layer develops towards the trailing edge.

Boundary layer parameters describe boundary layer development and are effective at estimating the streamwise location of transition within a separation bubble over an airfoil [12, 40, 42]. Past studies have shown that the maximum displacement thickness, δ^*, in the separation bubble corresponds approximately to the streamwise location of transition [12, 42]. Following transition, there is a slight reduction in the displacement thickness until reattachment, where it starts to grow within the re-developing turbulent boundary layer [12]. Furthermore, the momentum thickness, θ, remains approximately constant prior to transition, after which it increases significantly [42, 43]. The shape factor, H, defined as the ratio of the displacement thickness to the momentum thickness, is also an indicator of transition. Following a substantial increase in the shape factor due to the initial increase of the displacement thickness, the plateau (or peak) of the shape factor indicates the region of transition [12, 14]. The shape factor then decreases, as momentum thickness increases.

Separation, transition, and reattachment locations can also be estimated from mean surface pressure distributions [12, 32, 34, 35, 40, 42]. A typical mean surface pressure

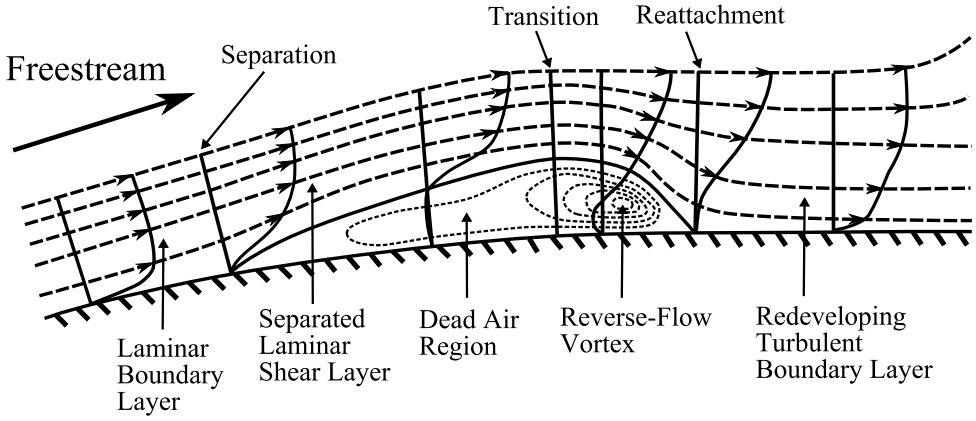


Figure 2.2: Time-averaged laminar separation bubble representation [40] based on the illustration of Alam and Sandham [38].

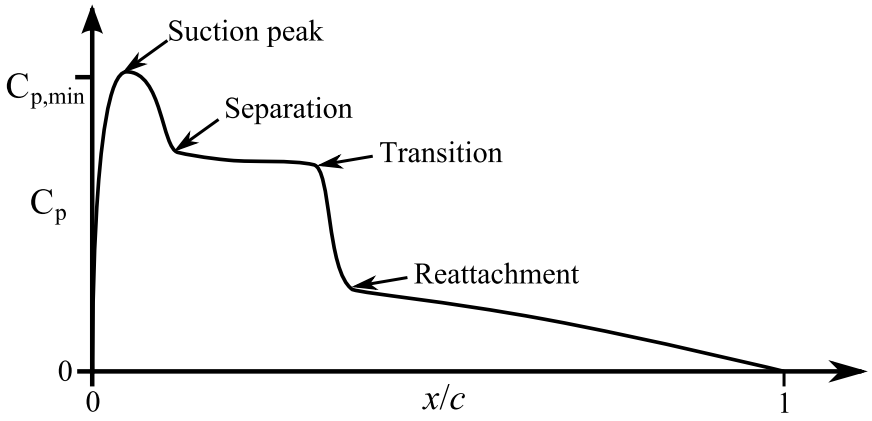


Figure 2.3: A typical suction side surface pressure distribution over an airfoil with a laminar separation bubble.

distribution for the upper surface of an airfoil with a separation bubble is illustrated in Fig. 2.3. It should be noted that the pressure coefficient axis is reversed, and that the suction peak, $C_{p,min}$, in this plot corresponds to a negative value. Following the point of minimum pressure, the presence of a plateau in the mean surface pressure distribution indicates a region of slow-moving fluid and, as a result, the approximate extent of the separation bubble. Following the plateau, a sharp increase in the mean pressure indicates that transition has occurred. After reattachment, the pressure recovery gradually continues within the re-developing turbulent boundary layer.

2.3 Separated Shear Layer Transition

Laminar-to-turbulent transition is essential in the formation of laminar separation bubbles at low Reynolds numbers. The study of separated shear layer transition has been the subject of numerous experimental investigations over airfoils, e.g. [10–12, 14, 17], and flat plates, e.g. [10, 22, 29]. More recently, direct numerical simulation (DNS) has been used to investigate this phenomenon over flat plates [23, 24, 26, 38, 44, 45], as well as airfoils [15, 16].

Following the separation of the laminar boundary layer, disturbances are amplified

exponentially in the separated shear layer within a band of unstable frequencies. This amplification is often preceded by a slight decay, which begins immediately downstream of separation [12]. The understanding and modelling of this exponential growth has been researched extensively, with disturbances having been shown to be well described by linear stability theory (LST) for flow over flat plates [29], backward facing steps [46], airfoils [11, 12], as well as other geometries [10]. When the amplitude of the disturbances grows sufficiently, nonlinear interactions between disturbances begin to occur, and the growth is no longer exponential. Dovgal et al. [10] showed that this stage is often characterized by the appearance of harmonics and a subharmonic of the frequency of the most amplified disturbance in the fluctuating velocity spectra. The distinction between linear and non-linear portions of disturbance growth allows for the separated shear layer transition to be divided in two stages: the earlier linear stage, which is associated with initial disturbance growth, and the later non-linear stages, where complex interactions between disturbances, lead to transition [10].

2.3.1 The Early Stage of Transition

The early stage of transition is defined by the exponential growth of disturbances within a band of unstable frequencies, centred on a fundamental or central frequency [47]. This growth is initiated by the separated shear layer instability to background disturbances or, in the case of many studies, artificial forcing. Artificial disturbance forcing is often used in both experimental [22, 29] and computational studies [13, 15, 44, 45] to sustain transition and to test the effect of different disturbance environments (e.g. 2-D versus 3-D forcing) on separated shear layer stability. As background disturbances initiate the shear layer instability, experimental studies performed at different facilities are subject to unique disturbance environments, which have considerable influence over transition [10].

This initial disturbance growth is followed by the onset of non-linear interactions, which eventually lead to transition. The exponential growth of the disturbances may be used to establish spatial growth rates, and these provide an indication of how quickly transition occurs. Larger growth rates indicate a more rapid transition and in separation bubbles forming over airfoils, the spatial growth rate has been shown to rise with increasing Reynolds number and angle of attack [7, 12]. LST models this process effectively, which allows for the central instability frequency and growth rates to be predicted [10–12]. In wind tunnels, these general aspects of the exponential growth may be investigated through hot-wire anemometry and surface pressure measurements [12, 32]. Fluctuating surface pressure measurements have been shown to effectively capture disturbance growth within the separated shear layers over airfoils [12, 31]. By acquiring simultaneous fluctuating surface pressure measurements, the convection velocity of disturbances within the shear

layer may be estimated through cross-correlation analysis [32] and was shown to increase with angle of attack [7]. Boutilier and Yarusevych [7] showed that the convection velocity falls within 30 to 50% of the boundary layer edge velocity within the laminar portion of the separation bubble at each angle of attack, agreeing with the range of phase speeds predicted by LST [10]. These results led Boutilier and Yarusevych [7] to suggest that the convection speed of disturbances is dependent on the proximity of the separated shear layer to the wall and the maximum velocity of the reverse flow.

Boundary layer velocity profiles may be acquired to further investigate the spatial aspects of this process. By filtering velocity signals to obtain disturbance profiles, Boutilier and Yarusevych [12] showed that, for flow over a NACA0018 airfoil, the vertical location of the maximum RMS velocity corresponds to the location of the maximum amplitude of the most amplified disturbance within the laminar portion of the separated shear layer. This location also lies closely to the displacement thickness and the location of the mean velocity profile inflection point [11, 12]. Disturbances of lower magnitude have also been shown to grow near the surface of the airfoil below the separated shear layer [11, 12]. As the maximum growth of disturbances occurs near the inflection point of separated shear layer mean velocity profiles, the primary growth mechanism is due to an inviscid Kelvin-Helmholtz. The proximity of the separated shear layer to the surface allows for viscous mechanisms to also influence disturbance growth. Thus, to study which instability mechanisms are responsible for the early stage of transition, LST has been used to model primary disturbance growth within the separated shear layer in separation bubbles [10–12, 45]. By comparing the results of viscous and inviscid stability predictions, Boutilier and Yarusevych [12] showed that the amplification of disturbances within a separation bubble over a NACA0018 airfoil is dominated by a linear inviscid mechanism with viscous effects mainly present near the surface ($y/\delta^* \leq 0.15$). This agrees with the results of Marxen et al. [45], which showed that, while viscous and inviscid instabilities each contribute to the growth of disturbances following separation, as the vertical position of the separated shear layer grows, a Kelvin-Helmoltz instability mechanism begins to dominate. These results imply that an inviscid instability is the primary cause of the initial disturbance growth within the separated shear layer until disturbances reach a certain amplitude, where nonlinear interactions between disturbances set in and initiate the later stages of transition.

While the later stages of transition eventually lead to the laminar-to-turbulent transition of the separated shear layer, they may also have an effect on the initial stage via feedback mechanisms [10]. This was demonstrated in a DNS of flow over a NACA0012 airfoil by Jones et al. [15], who showed that, while artificial forcing is at first required to initialize the primary shear layer instability, once forcing was disabled, the laminar-to-turbulent transition remained self-sustained over the airfoil. The authors suggest that this is caused by an absolute instability linked to the breakdown of shear layer vortices, causing disturbances

to convect upstream due to significant levels of reverse flow. Jones et al. [15] also note that similar absolute instability mechanisms have yet to be observed in experimental studies of separation bubbles forming over airfoils and flat plates. This is likely partly due to the difficulty in minimizing the effect of disturbances in experimental environments, which are often subject to significant background noise [48], to the level of computational studies. Following their earlier findings, Jones et al. [16] extended their study to investigate the receptivity of the separated shear layer and determined that the frequency of trailing edge tonal noise present in an acoustic feedback-loop may be related to the shedding of vortices. The results of these studies are significant since the shedding of shear layer vortices, which are characteristic of the later stages of transition, may play a important role in influencing the initial growth of disturbances in the separated shear layer through feedback mechanisms.

2.3.2 The Later Stages of Transition

Following the initial stage of transition, the onset of nonlinear interactions causes disturbance growth to deviate from the predictions of LST. At this point, the separated shear layer may roll up into vortical structures, which convect downstream, deform, and break down to turbulence. These structures provide a link between the initial growth of disturbances and the turbulent breakdown of the laminar flow, which makes them a fundamental part of transition. This process has been observed in experimental studies over airfoils [14, 17–20] and flat plates [22, 29], as well as DNS of airfoils [15, 21] and flat plates [23, 26, 38, 44, 45].

The formation of structures within the separated shear layer has been shown in experimental [14, 20, 22, 29] and numerical [23, 38, 44, 49] studies to be caused by an inviscid two-dimensional Kelvin-Helmholtz instability initiated by reverse flow. Spatially, the maximum growth of disturbances related to this instability has been shown to occur near the inflection point of the separated shear layer in mean velocity profiles [12, 22]. These vortices are shed at or near the central frequency of the most amplified disturbances in the shear layer [15, 16, 47, 49]. The magnitude of unstable disturbances required to trigger the onset of shear layer roll-up has been shown to be below 0.1 % of the free-stream velocity through experiments [20] and DNS [15].

The Kelvin-Helmholtz instability often results in the formation of large scale vortices [14, 22, 49], however, the shedding of large persistent coherent structures is not ubiquitous and the scale of the vortices has shown a dependence on the reverse flow velocity [21, 38]. Alam and Sandham [38] showed that large reverse flow velocities do not result in large spanwise-oriented structures but rather staggered structures. The magnitude of reverse flow in separation bubbles grows with increasing adverse pressure gradient and decreasing Reynolds number. For the separation bubble regime over airfoils, the adverse pressure gradient increases with angle of attack as the lift increases [2]. Thus, large structures

would be more likely to exist at lower angles of attack. Balzer and Fasel [21] demonstrated this over a NACA 64_3-618 airfoil by showing that large vortices were only shed at a lower angle of attack, while at a larger angle, vortices were much smaller and broke down more rapidly. As the chord Reynolds number of an airfoil is increased, the adverse pressure gradient should decrease at a given angle of attack, resulting in larger structures. This has been shown to be true in studies over an SD7003 airfoil by Burgmann and Schröder [14] and Zhang et al. [19]. The scale of vortices is also related to the rate of shedding. Burgmann and Schröder [14] showed that, at a given Reynolds number, the shedding frequency of vortices increases with angle of attack. Increasing the Reynolds number, however, also results in increased shedding rates. This would be expected, because the central frequency of unstable frequencies relating to Kelvin-Helmholtz instabilities grows with both increasing angle of attack and Reynolds number [7]. The turbulence intensity of the free-stream also has an effect on the formation of vortices. Burgmann and Schröder [14] demonstrated that increasing the free-stream turbulence intensity reduces the size of vortices, but has little effect on the vortex shedding frequency.

Studies over airfoils [21, 27] and flat plates [22–24, 26] have found that, at formation, roll-up vortices can be two-dimensional across the span. Such spanwise coherent vortices have been linked to strong amplification of two-dimensional Kelvin-Helmholtz instability modes [29], which generally occurs in wall-bounded shear flows [50]. Following their formation, these two-dimensional rollers convect downstream, deform, and break down to turbulence. In some cases, the weakly-periodic merging of vortices followed by a rapid breakdown has been observed [13, 25]. This process resembles what occurs for backward-facing steps [51, 52] and plane mixing layers [53–55]. Vortex merging has been linked to the strong growth of two-dimensional subharmonic fluctuations of the most amplified disturbance, which becomes dominant in regions of vortex merging [13, 55]. While many studies have shown that roll-up structures form coherently across the span, these studies typically investigate airfoils operating at lower angles of attack and over flat plates with 2-D forcing. On the other hand, studies with strong three-dimensional disturbance forcing [13, 15, 29] and larger adverse pressure gradients [21, 38] have observed that the roll-up of the shear layer occurs with a reduced spanwise coherence. This in turn can causes roll-up structures to break down shortly after emerging through an oblique breakdown mechanism [21, 38].

For strongly two-dimensional (2-D) vortices to transition to turbulence, they must deform significantly across the span and generate spanwise perturbations. Following their formation, the rollers break down into smaller-scale three-dimensional structures, which in some studies on airfoils [14, 18–20] and flat plates [22, 23, 29], have been shown to persist past mean reattachment. In some cases, these structures have even been observed to displace as far as into the wake of an airfoil [17] and in some flat plate studies, they have even been shown

to eject from near the surface [22, 23, 29]. For flow over an SD7003 airfoil, Burgmann and Schröder [14] showed that spanwise-oriented vortices become c-shaped and subsequently evolve into interacting 'screwdriver' vortex pairs during breakdown. The interactions between the vortices become more pronounced with increasing Reynolds number, leading to the formation of arc-like structures, which resemble Λ-vortices. This type of structure has been observed in other studies on airfoils [17, 19] and in some studies on flat plates undergoing 2-D forcing [28, 38]. Also, the formation of Λ-structures is not limited to studies with spanwise rollers, and such structures have also been observed in DNS of flat plates with strong three-dimensional forcing and a less coherent roll-up [38, 44]. While Λ-vortices have appeared frequently in separation bubble studies, other types of structures have been observed [15, 22, 25]. In their DNS of a NACA0012 airfoil, Jones et al. [15] showed that spanwise-oriented vortices deform into streamwise-oriented, spanwise-periodic structures. These streamwise-oriented structures, also known as ribs, have also been observed in separation bubbles forming over flat plates [13, 25]. In their Large-Eddy Simulation (LES) of flow over a flat plate, Abdalla and Yang [25] associated the formation of both Λ and streamwise vortices to the helical pairing of spanwise vortices.

While the primary growth of 2-D waves initiates the roll-up of the separated shear layer, secondary instabilities are responsible for the deformation and breakdown of roll-up vortices. More recently, secondary instability mechanisms have been investigated in studies combining DNS and experiments with forcing over flat plates [13], and using DNS with and without forcing over a NACA0012 airfoil [15]. These studies have shown that secondary instabilities cause spanwise-oriented vortices to break down and complex secondary vortex to form following shear-layer roll-up. Specifically, these mechanisms include elliptical instability [13, 15], originating within roll-up vortices, and hyperbolic instability [15], located within the braid region located upstream or between two consecutive roll-up vortices. Elliptical instability is initiated at the onset of vortex stretching and has been shown to cause a rapid breakdown to turbulence in a process beginning in the near-wall region [13]. The name of the instability comes from the elliptical shape of the streamlines caused by vortex shedding. Furthermore, Marxen et al. [13] showed that this instability is associated with the generation of spanwise waviness and merging of vortices, and may be associated with the fundamental and subharmonic growth of disturbances in cases where two vortices interact [13]. Hyperbolic instability leads to the amplification of disturbances within the braid region, associated with hyperbolic flow named after that streamlines make in this region [15]. Jones et al. [15] linked both elliptical and hyperbolic instabilities to the generation of streamwise-oriented vortex cores observed during the breakdown of shear layer vortices. The streamwise vortices are caused by the strong amplification of perturbuations with spanwise wavenumbers on the order of the streamwise extent of roll-up vortices within the braid region. Jones et al. [15] also showed that streamwise vortices convect upstream

with the high-magnitude reverse flow velocity and cause roll-up vortices to breakdown in a self-sustaining process indicative of an absolute instability. Marxen et al. [13] also linked the formation of similar streamwise-elongated vortices during breakdown to an instability originating within the braid region; however, unlike Jones et al. [15], they did not observe hyperbolic flow in this region.

Despite the significant recent advances in the study of separated shear layer vortices, certain aspects regarding the formation and development of these structures and their role in the later stages of transition remain unanswered. This is illustrated by the observed differences between past studies discussed in this chapter. Because the development of laminar separation bubbles is very sensitive to the streamwise pressure gradient and forcing [13], the formation and development of shear layer vortices is strongly dependent on geometry and experimental conditions such as disturbance environment, Reynolds number, and angle of attack over airfoils. At this moment, few studies have investigated this phenomenon over airfoils operating at low Reynolds numbers. Furthermore, these studies have been performed over limited airfoil geometries (i.e. SD7003, NACA0012) at chord Reynolds numbers below 60,000 and generally at mid-range angles of attack between 3 and 8°. Thus, further investigation into separated shear layer transition within separation bubbles forming over other airfoil geometries at larger Reynolds numbers across a larger range of angles of attack remains imperative. Furthermore, while past studies have investigated the flow physics of shear layer vortex shedding, none of these studies has established the link between surface pressure fluctuations and the later stages of transition, which could have considerable benefits the design and implementation of active flow control systems.

Chapter 3

Experimental Methodology

An experimental investigation of separated shear layer transition within a laminar separation bubble was conducted for flow over an airfoil at a low Reynolds number. A NACA0018 airfoil model was mounted in the University of Waterloo's low-speed wind tunnel and a combination of experimental methods was employed to investigate flow development. Previous studies at the same facility and over the same airfoil model have been performed by Boutilier [43] and Gerakopulos [31]. The results of these studies were consulted to select the experimental conditions for this investigation. Experiments were performed at a chord Reynolds number of $Re_c = 10^5$ and at angles of attack of $\alpha = 0$, 5, 8, and 10°. The chord Reynolds number was chosen to allow for velocities within the separated shear layer of a sufficiently large magnitude to minimize the inaccuracies of low velocity hot-wire calibration [22, 56], yet sufficiently low to facilitate flow visualization. The range of α was selected to study separation bubbles of varying lengths positioned at different locations along the airfoil surface. To characterise disturbance growth within the shear layer, long-duration measurements were acquired for each profile with the rake positioned at the displacement thickness, $y = \delta^*$, for $\alpha = 0$, 5 and 8°. The displacement thickness for $\alpha = 0°$ was obtained from the results of Boutilier [43]. Due to the effect of the rake on flow development, boundary layer profiles at $\alpha = 10°$ are not presented; although it should be noted that smoke-wire flow visualizations were performed successfully at this angle of attack.

3.1 Experimental Setup

3.1.1 University of Waterloo Low Speed Wind Tunnel

The experiments were performed in an open-loop adaptive-wall wind tunnel at the University of Waterloo (Fig. 3.1). The wind tunnel has a 9.55:1 contraction followed by a 6.0 m test section with rigid sidewalls, and adaptable upper and lower walls. The width of the test section is 0.61 m and the height with the adaptive-walls in a geometrically straight configuration is 0.89 m. From the perspective of Figure 3.1, the sidewall furthest into the page is painted matte black to minimize reflections and increase contrast during smoke-wire visualizations, while the opposite wall is made of plexiglass. The upper and lower walls were each kept in a geometrically straight configuration for all experiments presented in this study by forty-eight rack and pinion jacks. The upper and lower walls were lined with inflated rubber seals, which were pressurized to 150 kPa to prevent leakage in the test section. Each adjustable wall has seventy static pressure taps to allow for wall surface pressure measurements. The inlet of the contraction was renovated by Bishop [57] to improve the flow conditioning of the wind tunnel with the addition of a steel screen followed by aluminium honeycomb and three more steel screens ahead of the contraction. The maximum free-stream turbulence intensity within the test section is less than 0.3 % for the Reynolds number studied.

The wind tunnel free-stream speed was set using the contraction static pressure drop measured by an inclined manometer with a 1.25 Pa resolution. The pressure upstream and downstream of the contraction was obtained by averaging the pressure obtained from three

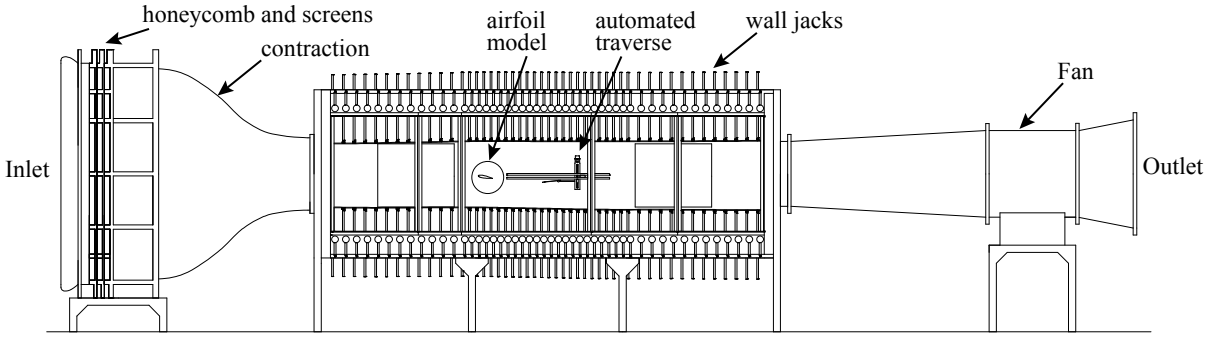


Figure 3.1: University of Waterloo adaptive-wall wind tunnel. Reproduced from Boutilier [43].

1 mm diameter static pressure taps located on the upper and side walls at each location. The uncertainty in setting the free-stream velocity was estimated to be approximately 2.5 %.

3.1.2 NACA0018 Airfoil Model

Measurements were performed over a NACA0018 airfoil model (Fig. 3.2a) with a 200 mm chord length, c, and a 600 mm span developed and manufactured by Gerakopulos [31]. The model's axis of rotation was located 60 mm from the airfoil leading edge (0.3 c) and was mounted 2.0 m (10 c) downstream of the wind tunnel contraction. The flow uniformity at the streamwise location of the model was estimated to be within $\pm 0.6\,\%$ [57]. The model's axis of rotation is defined as the origin of an X and Y coordinate system shown in Figure 3.2b. The x-coordinate is along the airfoil chord, beginning at the leading edge, while the y-coordinate runs vertical and originates at the surface of a given x . The spanwise Z-coordinate begins at the airfoil center X-Y plane with the system following the right-hand rule.

The aluminium model contained a total of ninety-five static pressure taps of 0.4 mm diameter allowing for static surface pressure measurements. Sixty-five of these taps were positioned near the airfoil center plane ($Z = 0$) with one on the leading edge and the rest distributed in even numbers along the upper and lower surfaces. The remaining taps were distributed along the upper surface forming three spanwise rows at $x/c = 0.15$, 0.30, and 0.60. The pressure taps were connected to a mechanical Scanivalve system with 0.8 mm flexible tubing. More details on this system can be found in Boutilier [43]. To permit

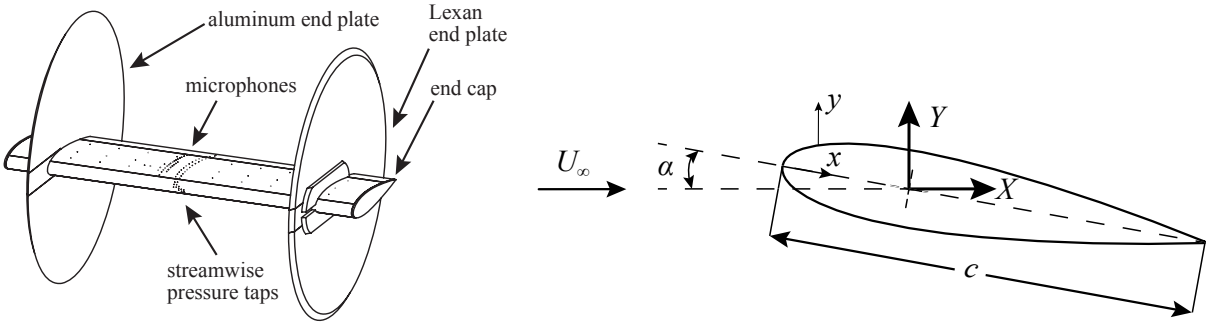


Figure 3.2: (a) Airfoil model with end plates and end caps installed, reproduced from Boutilier [43], and (b)definition of coordinate systems with the Z-coordinate coming out of the page at the X-Y center plane.

fluctuating surface pressure measurements, twenty-five microphones were distributed along the upper surface of the airfoil below 0.8 mm diameter holes. The size of the holes was selected by Gerakopulos [31] such that the Helmholtz cavity resonance is significantly larger than the maximum frequency of disturbance growth within the separated shear layer. As shown in Fig. 3.3, twenty-two of the microphones were divided between a full and partial row located along the $Z/c = -0.20$ and $Z/c = -0.16$ planes, respectively. The remaining three microphones were located at $x/c = 0.21$ across the span at $Z/c = 0.242$, 0.329, and 0.378. Along with a full row sensor at the same streamwise location, these microphones allow for simultaneous fluctuating pressure measurements across the span.

In a closed test section, the growth of the boundary layer along the test section walls may affect the flow over the model [33, 48]. To prevent this, end plates were mounted on the model [33, 58]. Boundary-layer measurements were performed on the model with 450 mm diameter end plates clamped directly onto the airfoil model and end caps, as shown in Figure 3.2a. The end plates, which were manufactured by Boutilier [43], were positioned 10 cm away from the test section side walls such that the spacing between them was $b/c = 2.0$. Boutilier and Yarusevych [33] found that mounting the end plates in this configuration resulted in a mean flow uniformity within 2.5 % from surface pressure measurements obtained across the airfoil span. More details on the endplate design may be found in Boutilier [43]. The flow visualization study was performed with only end caps mounted onto the airfoil. Removing the end plates was necessary to facilitate the

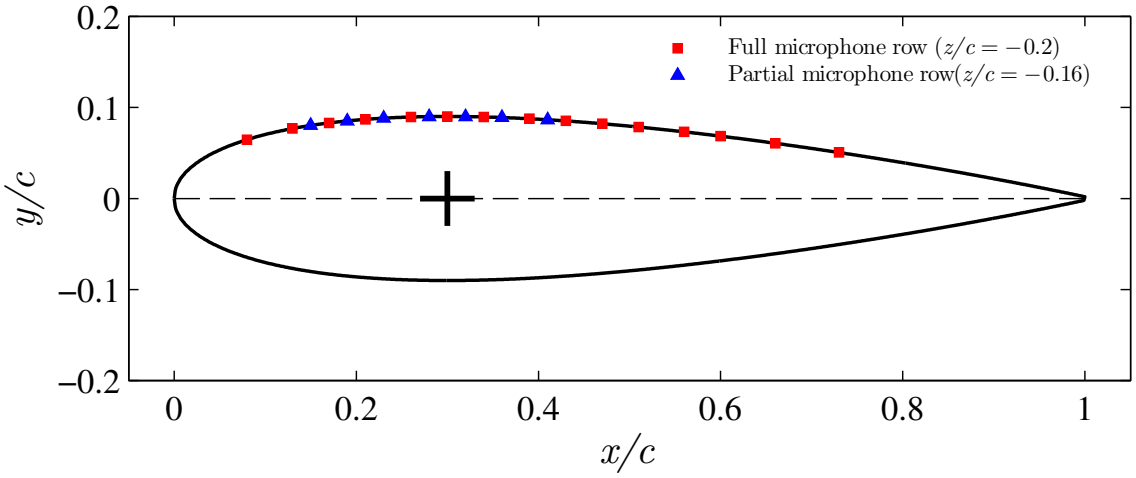


Figure 3.3: Locations of microphones embedded into NACA0018 airfoil model.

mounting of the smoke wire system and the capture of images and videos. Without end plates, the mean spanwise uniformity over the model is reduced but is still satisfactory with the position of the separation bubble only slightly changed [33].

Solid, wake, and upper and lower test section wall boundary layer blockage may also affect closed test section measurements [33, 48]. The solid blockage by the airfoil model may be described by a blockage ratio, B, which is defined as the maximum cross-sectional area of the airfoil with or without end plates divided by the cross-sectional area of the test section. The blockage ratios for the configurations tested in this thesis are presented in Table 3.1. Mounting end plates results in an additional 1.1 % of blockage with the maximum blockage ratios occuring at $\alpha = 10°$. While blockage does have an effect on the upper surface pressure distribution, estimated separation, transition, and reattachment locations along with central instability frequencies are not expected to change significantly [33]. As the effects of blockage are relatively insignificant on separation bubble characteristics, geometrically straight walls were used in this study.

3.2 Measurement Techniques

Several measurement techniques were employed to characterize the flow development. Surface pressure distribution measurements were performed over the airfoil (i) to represent the mean flow development, (ii) to estimate the separation, transition, and reattachment locations, (iii) to assess the spanwise uniformity of the flow development over the airfoil, and (iv) the intrusiveness of other experimental methods. A rake of six boundary layer hot-wire probes was traversed in the region of separation bubble formation to obtain streamwise velocity profiles, which were used to extract boundary layer parameters and study the development of disturbances. Long-duration velocity measurements were obtained at $y = \delta^*$ for spectral and correlation analysis. Microphone measurements of the same duration were also performed independently for spectral analysis and correlation analysis. Lastly, a series

Table 3.1: Model solid blockage ratio, B [%], with and without end plates installed.

α, degrees	B, without end plates	B, with end plates
0	4.0	5.1
5	4.3	5.4
8	4.7	5.8
10	5.2	6.3

of flow visualizations using a smoke-wire technique was performed to obtain images and high-speed video of flow over the airfoil and within the separation bubble.

3.2.1 Static Surface Pressure Measurements

Differential static pressure was measured between the model surface pressure and reference pressure obtained from a wall pressure tap located on the wind tunnel floor upstream of the airfoil. A mechanical system with a total of three Scanivalve mechanical multiplexers was used to connect the airfoil pneumatic tubing to two Lucas Schaevitz P3061-2WD pressure transducers with full scale input and output ranges of 500 Pa and ±5V, respectively. The transducers were calibrated against an inclined manometer, with 0.25 Pa minor divisions. The uncertainty of the static pressure measurements is estimated to be less than 1.6 % of the dynamic pressure [43]. Signals were sampled by a National Instruments PCI-6259 data acquisition card. The system is operated by a LabVIEW virtual instrument routine, which actuates the multiplexers to cycle through the connections. The routine begins by obtaining a zero pressure offset to compensate for the temperature drift of the static pressure transducers. This is followed by a sixty second delay prior to the first measurement, and a thirty second delay between all subsequent measurements to allow for the pressure to stabilize following the recommendations of Boutilier [43].

3.2.2 Fluctuating Surface Pressure Measurements

Fluctuating surface pressure measurements were obtained with twenty-five Panasonic WM-62C omnidirectional back electret condenser microphones located directly beneath 0.8 mm diameter holes on the upper airfoil surface. Each microphone signal was amplified by a Linear Technology LT 1120 dual operational amplifier with the amplification bridge mounted within the airfoil and powered by an external 30 VDC power supply. The microphone signals were sampled by a National Instruments PCI-4472 data acquisition card via coaxial cables with a total length of 6 m. The data acquisition card allows for up to eight microphone signals to be sample simultaneously. All microphone measurements were low-pass filtered by the PCI-4472 at 2.5 kHz. More details on the microphone selection, port design, and calibration may be found in Gerakopulos [31].

Fluctuating surface pressure measurements for the clean model were acquired at 10 kHz for a total of 2^{22} samples. The sampling rate was selected to provide sufficient temporal resolution for cross-correlation coefficient functions. Spectra were computed using Welch's method [59] with 256 non-overlapping rectangular windows, giving a spectral resolution of 0.6 Hz. Measurements investigating the effect of boundary layer probes and the smoke wire were sampled at 40 kHz for a total of 2^{23} samples. Fluctuating surface pressure spectra

were computed using Welch's method [59] with 128 non-overlapping rectangular windows, giving a spectral resolution of approximately 0.6 Hz.

3.2.3 Velocity Measurements

Streamwise velocity measurements were performed with a rake of six normal boundary layer type probes (Dantec 55P15) operated by a Dantec Streamline Pro constant temperature anemometry system. The rake was angled at approximately 7° to the curvature of the airfoil following the recommendations of Brendel and Mueller [42]. Within the separated shear layer, the uncertainty in the velocity measurements is estimated to be less than 5% [60]. The rake was positioned with an automated three-axis traverse (Fig. 3.4), with an estimated uncertainty in positioning of ± 0.025 mm in the vertical and spanwise directions, and ± 0.05 mm in the streamwise direction [31].

As shown in Fig. 3.5, adjacent probes within the rake were separated by 6 mm in the spanwise direction. The probes were aligned optically over the airfoil surface and the alignment between probes was confirmed through digital images taken with a Nikon D300 digital SLR camera with a Nikon UV-Nikkor 105 mm f/4.5 macro lens and a Nikon SB-600 speedlight. The estimated uncertainty in the alignment is within $\pm 0.1\,mm$ in both the streamwise and vertical directions respectively. The probe alignment images were used to adjust the vertical positions of velocity profiles presented in Section 4.2.2, to compensate for slight vertical misalignments between the probes.

The probes were calibrated in situ upstream of the airfoil using a Pitot-static tube positioned at the same X-Y plane within 50 mm. The Pitot-static tube measurements were performed with two inclined manometers of 1.25 Pa and 2.5 Pa minor divisions to allow for lower and higher calibration velocities. A calibration curve was constructed using a fourth-order polynomial fit of the hot-wire bridge output voltage and the free-stream velocity following the recommendations of Bruun and Khan [61].

For all hot-wire measurements, the bridge top voltage output from the Dantec Streamline Pro was sampled at 20 kHz and low-pass filtered at 2.5 kHz by a National Instruments PCI-4472 data acquisition card. The sampling rate was selected to provide sufficient temporal resolution for cross-correlation coefficient functions. For the long-duration measurements obtained with the rake positioned at the displacement thickness, 2^{23} samples were acquired over approximately seven minutes. Streamwise fluctuating velocity spectra on these long-duration measurements were computed using Welch's method [59] with 256 non-overlapping rectangular windows, giving a spectral resolution of approximately 0.6 Hz.

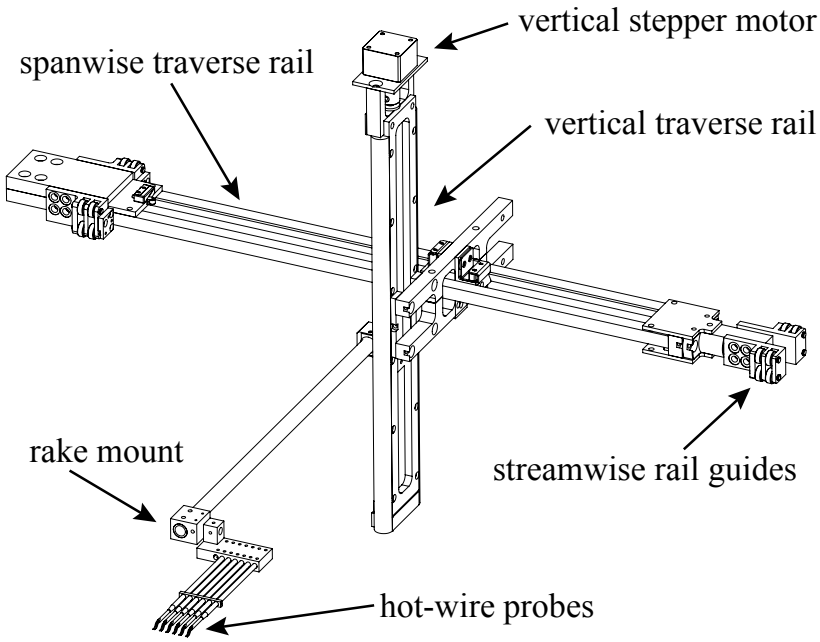


Figure 3.4: Isometric view of positioning traverse with rake of hot-wire probes.

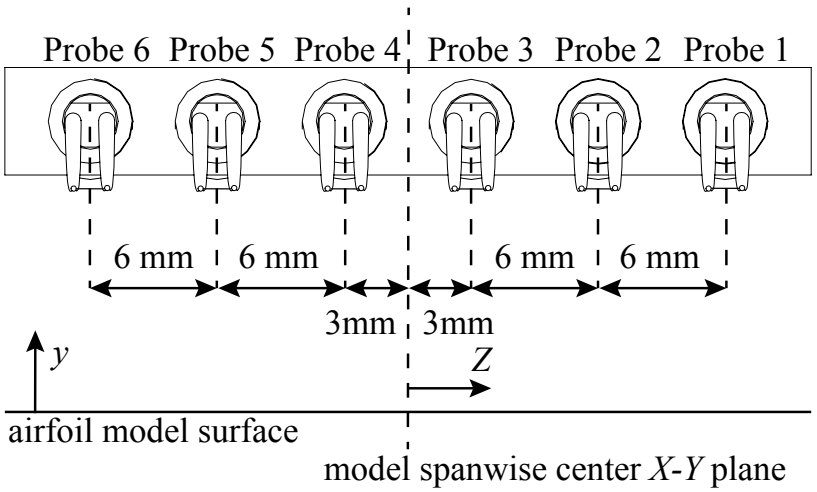


Figure 3.5: Front view of hot-wire placement in the rake. Note: the main direction of the flow is into the page.

3.3 Flow Visualization

Smoke-wire flow visualizations were captured over the airfoil without end plates using a 0.1 mm diameter steel wire. A smoke-wire was positioned in two main configurations with the wire placed (1) vertically, 50 mm (0.25 x/c) upstream of the airfoil at $Z/c = 0.25$, (Fig. 3.6a) and (2) within the initial portion of the separation bubble on the suction side across the span (Fig. 3.6b).

In both configurations, the wire was kept in tension with a combination of a spring and a weight attached to a platform, which was secured to the test section floor. The streamwise position of the smoke wire for the first configuration was based on the technique described by Yarusevych et al. [62]. The spanwise position of the wire was selected to avoid possible contamination of microphone ports and pressure taps. The smoke wire positions for the second configuration are given in Table 3.2. The streamwise smoke-wire positions were selected based on a combination of surface pressure distributions, and the streamwise development of RMS fluctuating surface pressure and RMS velocities. The y/c position of the smoke-wire within the separated shear layer was selected based on velocity profiles, such that the Reynolds number based on the wire diameter was less than 50. This was done to prevent vortex shedding off of the wire, following the recommendations of Batill [63] .

A smoke-generating mixture comprised of 70% glycerin and 30% distilled water was applied to the wire following the recommendations of Boutilier [43]. A variable AC

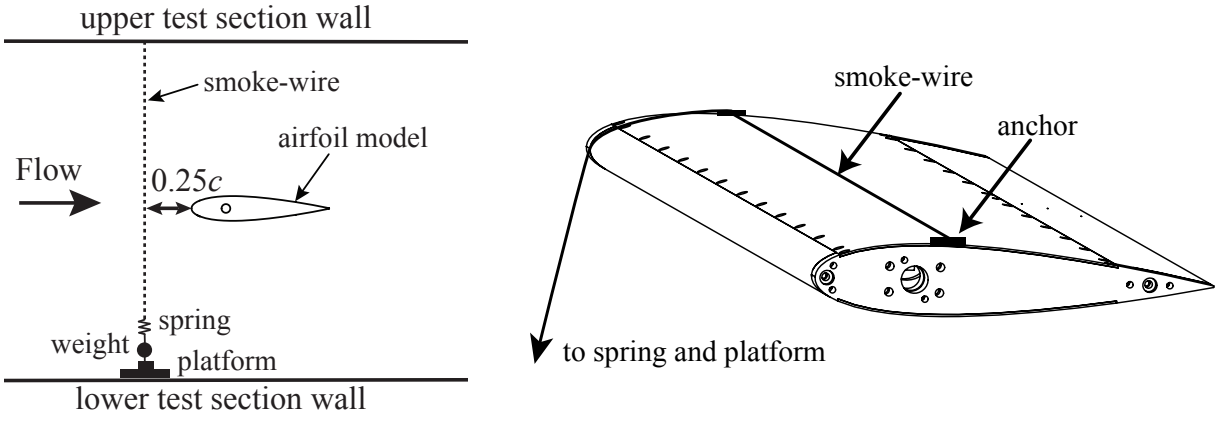


Figure 3.6: Schematics of flow visualization setups with smoke-wire placed (a) vertically upstream of the airfoil and (b) across the span close to the surface of the model. Note: the schematics are not to scale.

Table 3.2: Streamwise and vertical positions of the smoke-wire in the second configuration.

α, degrees	x/c	y/c
0	0.6	0.0075
5	0.33 & 0.38	0.0075
8	0.2	0.005
10	0.19	0.0075

transformer was connected to the smoke-wire, and a voltage between 65-70 V was applied to evaporate the smoke generating liquid.

A Photron Fastcam SA4 high-speed camera fitted with a Nikon UV-Nikkor 105 mm f/4.5 macro lens was used to capture image sequences of the visualizations. The camera captured images at a resolution of 1024×1024 pixels at frame rates of up to 3,600 frames per second (FPS) and at a resolution of 1024×768 at frame rates of up to 4,000 FPS. The camera was controlled with Photron Fastcam Viewer Version 3.3.8. A Nikon D300 digital SLR (dSLR) camera was used to acquire higher definition images at approximately 9 FPS. The smoke was illuminated by a laser sheet produced by a Photonics Industries DM20-527 Nd:YLF laser and LaVision light sheet optic.

For the first configuration, side view images (i.e. X-Y plane) were taken with a Nikon D300 dSLR camera fitted with a Nikon 1870 mm f/3.54.5 Nikkor AF-S DX lens. Figure 3.7 shows a schematic of the setup used to illuminate the flow. The laser head was mounted outside the test section, and the beam was reflected by a mirror into the LaVision light sheet optic, which were both mounted onto the traverse.

For the second configuration, side view images were taken with a Nikon D300 dSLR camera fitted with a Nikon UV-Nikkor 105 mm f/4.5 macro lens and the high-speed camera. The smoke was illuminated using the same setup as the first smoke-wire configuration. For top view images (i.e. X-Z plane), higher definition images were acquired with the Nikon D300 digital SLR camera fitted with a Nikon 1870 mm f/3.54.5 Nikkor AF-S DX lens mounted on a tripod within the test section. High-speed image sequences were acquired with the high-speed camera placed outside the test section with the field-of-view above the airfoil reflected by a 0.15 m×0.20 m, 3 mm clear glass mirror mounted on the upper test section wall directly above the airfoil model. A laser sheet was directed from outside the clear test section wall with the LaVision light sheet optic attached to the laser head.

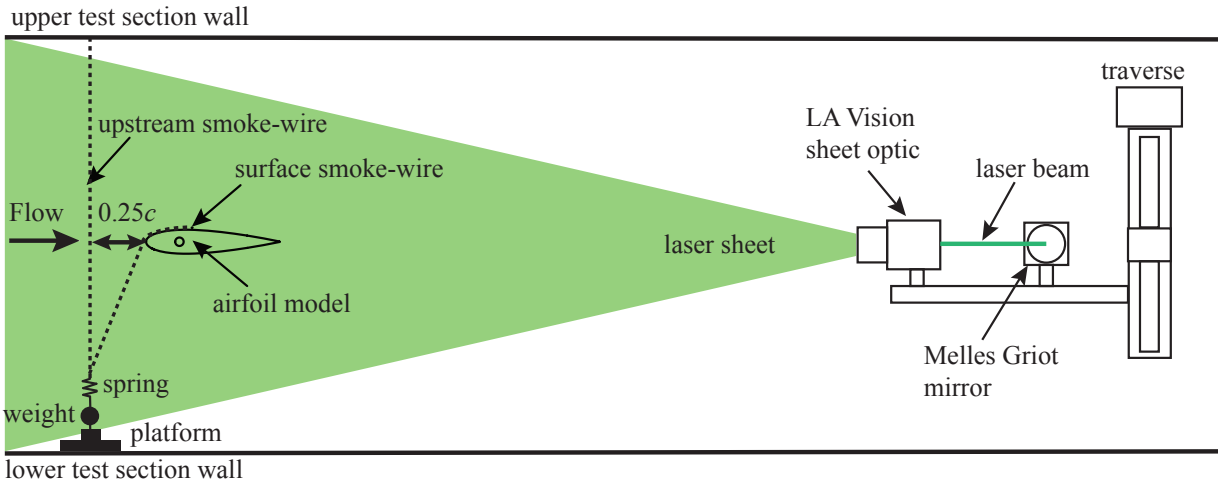


Figure 3.7: Schematic of streamwise flow visualization laser sheet setup. Note: the diagram is not to scale.

Chapter 4

Results

This chapter presents results pertaining to flow development over the NACA0018 airfoil at a chord Reynolds number of $Re_c = 10^5$. The chapter is divided into three sections. Section 4.1 presents flow visualizations acquired after introducing smoke into the flow with a wire placed vertically upstream of the model and across the span within the separated shear layer. Section 4.2 investigates the streamwise development of the flow and the onset of the later stages of transition through the analysis of high-speed flow visualization of the separation bubble and the boundary layer measurements. Vortex merging and shear layer flapping are also investigated in this Section 4.2. Section 4.3 investigates the spanwise development of vortices through high-speed flow visualization and the analysis of velocity measurements acquired simultaneously with a rake of hot-wires.

4.1 Flow Visualization

Two types of flow visualization were performed to study flow development. Flow visualization with a smoke-wire placed vertically upstream of the airfoil model was performed to capture flow development around the airfoil, while separation bubble visualizations obtained with a smoke-wire placed across the span of the airfoil within the separated shear layer were performed to investigate the laminar-to-turbulent transition occurring within the separation bubble. The visualizations were performed with end plates removed from the model to improve image quality. As the flow visualization presented in this section is meant to give a more general overview of the flow development, image sequences acquired at high-speeds are presented later in Sections 4.2 and 4.3. The effect on flow development when placing a smoke-wire within the separated shear layer is presented in Appendix B.1.

4.1.1 Upstream Smoke-Wire Flow Visualization

Figures 4.1-4.4 present upstream smoke-wire visualizations performed for the separation bubble regime over the airfoil. In each image, the shape of the airfoil model at the wall nearest the camera is outlined in white. Streaklines have been generated from a smoke-wire placed towards the airfoil spanwise center plane. Upstream of the airfoil, there is a region where streaklines are not visible due to a shadow cast by the model.

The streaklines give a description of flow development over the airfoil at a low Reynolds number. In each of the images, the proximity of the smoke over the upper side of the airfoil indicates that the flow is attached. Surface pressure measurements presented in Section 4.2.2 confirm that a laminar separation bubble forms at each of these angles of attack. A narrow wake is visible downstream of the trailing edge and, at $\alpha = 0$ and $5°$, the wake exhibits a typical vortex shedding pattern. Note that, the perspective of the camera combined with the plane of the smoke may give the impression that the streaklines are further away from the surface than they actually are, and causes the flow at $\alpha = 0°$ to appear asymmetric.

While a laminar separation bubble forms in at each of these angles of attack, these flow visualizations do not reveal dynamics within the separation bubble, as it develops near the surface of the airfoil. Still, the streaklines nearest the airfoil suction side surface exhibit some unsteadiness in the form of waviness and minor mixing of the smoke. This type of unsteadiness has also been observed of streaklines near the surface of the suction side in other flow visualizations of airfoils operating at low Reynolds numbers [12, 36, 42, 64].

The unsteadiness of the streaklines suggests that flow development is likely more complex close to the airfoil surface, and may be related to the formation and development of vortices that has been observed within laminar separation bubbles forming over airfoils [14].

4.1.2 Separation Bubble Flow Visualizations

To visualize flow development within the separation bubble forming on the suction side, visualizations were performed with a smoke-wire placed across the span of the airfoil within the separated shear layer. Figures 4.5-4.8 present side view images of these separation bubble visualizations. The flow direction and approximate location of the field of view is indicated in the diagram to the lower left of each image.

In Figures 4.5-4.8, smoke is introduced into the separated shear layer by a smoke-wire placed at $x/c = 0.6$, 0.33, 0.2 and 0.19, respectively. The images show the development of smoke, which reflects the dynamics occurring within a separation bubble. Note that, in each figure, the reflection of the smoke is visible on the airfoil surface.

The visualizations depict the formation and development of shear layer vortices. In

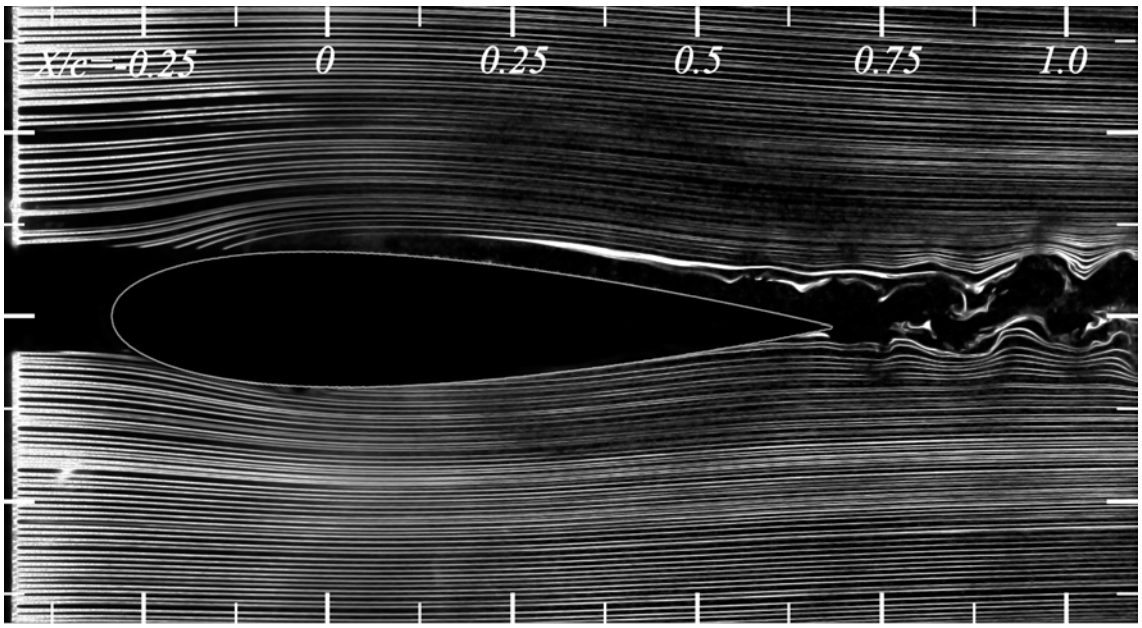


Figure 4.1: Upstream smoke-wire flow visualization for $\alpha = 0°$.

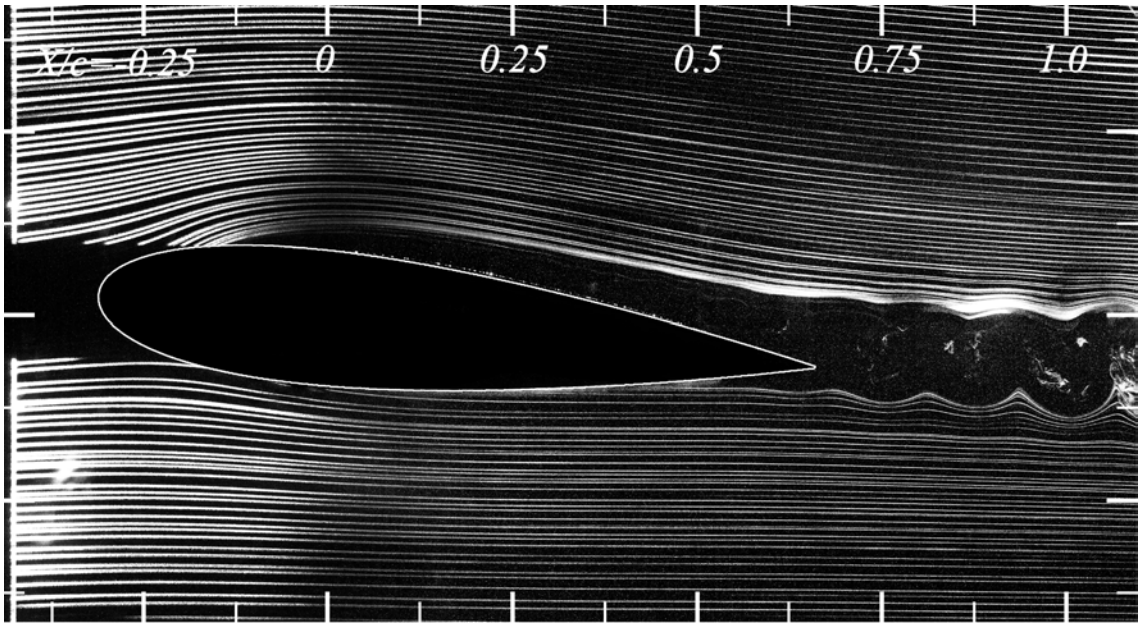


Figure 4.2: Upstream smoke-wire flow visualization for $\alpha = 5°$.

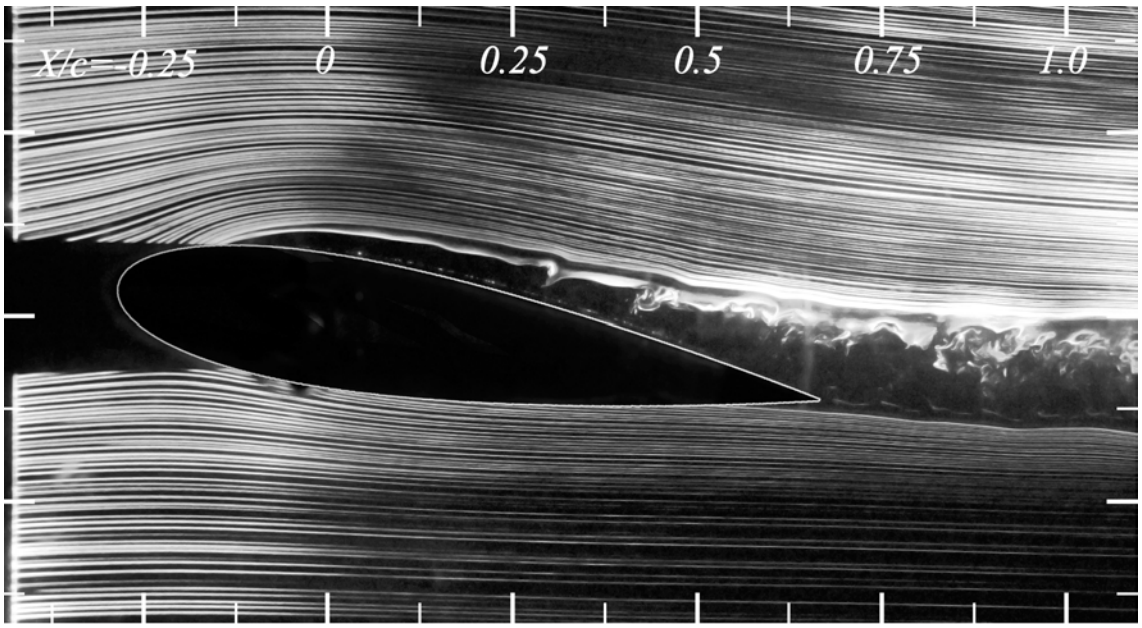


Figure 4.3: Upstream smoke-wire flow visualization for $\alpha = 8°$.

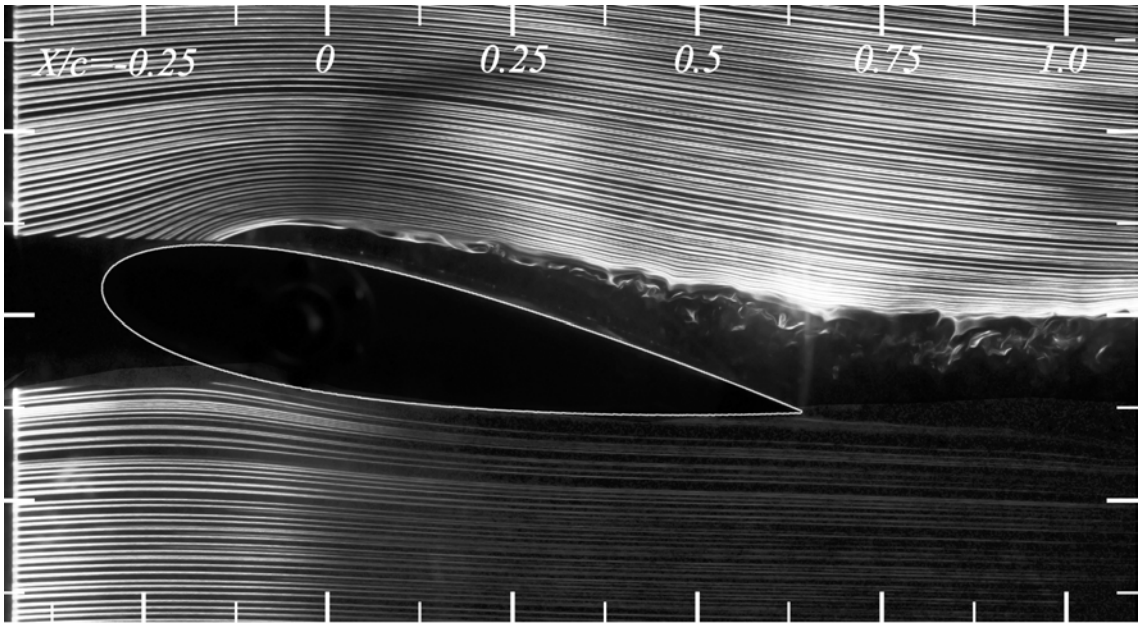


Figure 4.4: Upstream smoke-wire flow visualization for $\alpha = 10°$.

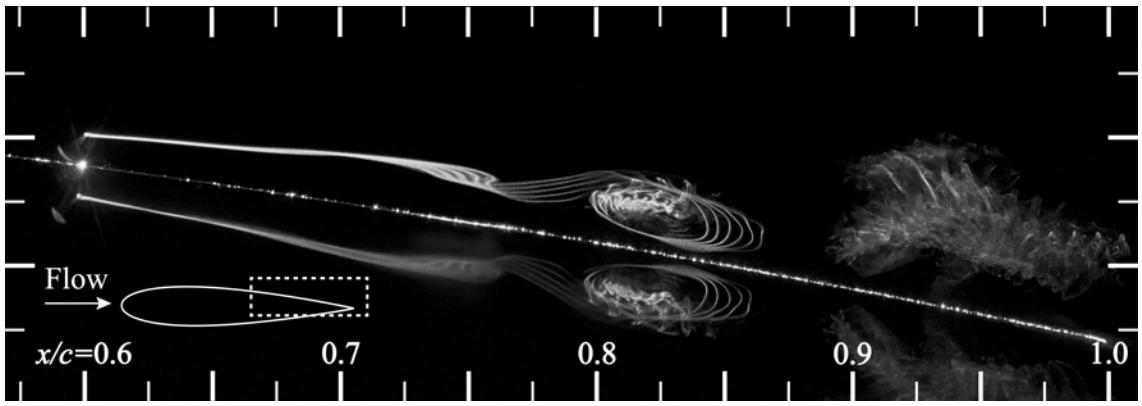


Figure 4.5: Side view separation bubble visualization for $\alpha = 0°$.

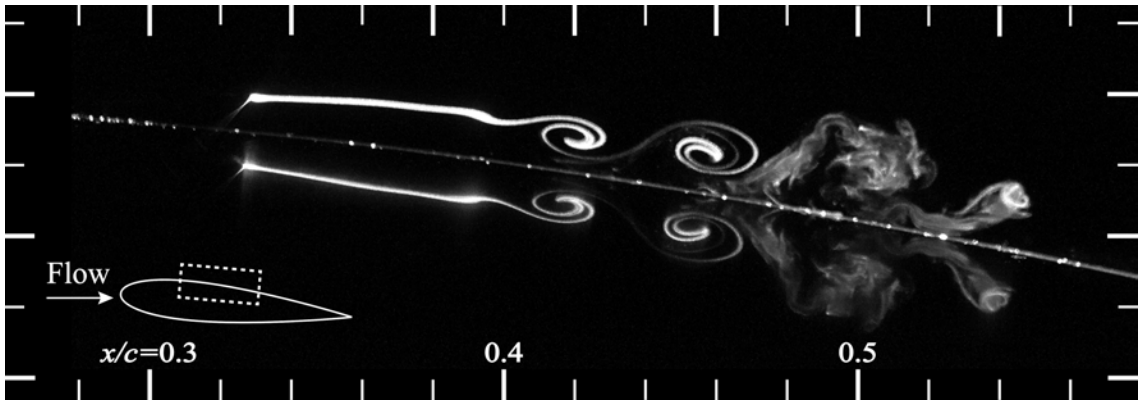


Figure 4.6: Side view separation bubble visualization for $\alpha = 5°$.

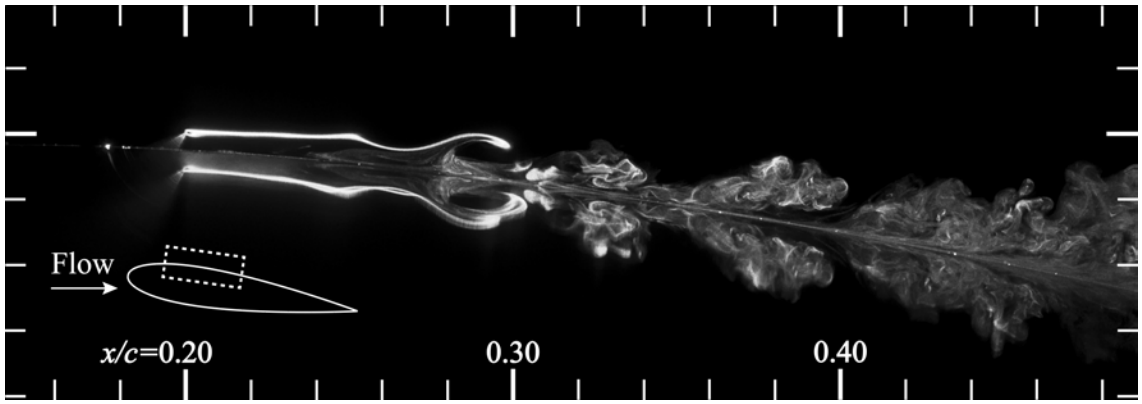


Figure 4.7: Side view separation bubble visualization for $\alpha = 8°$.

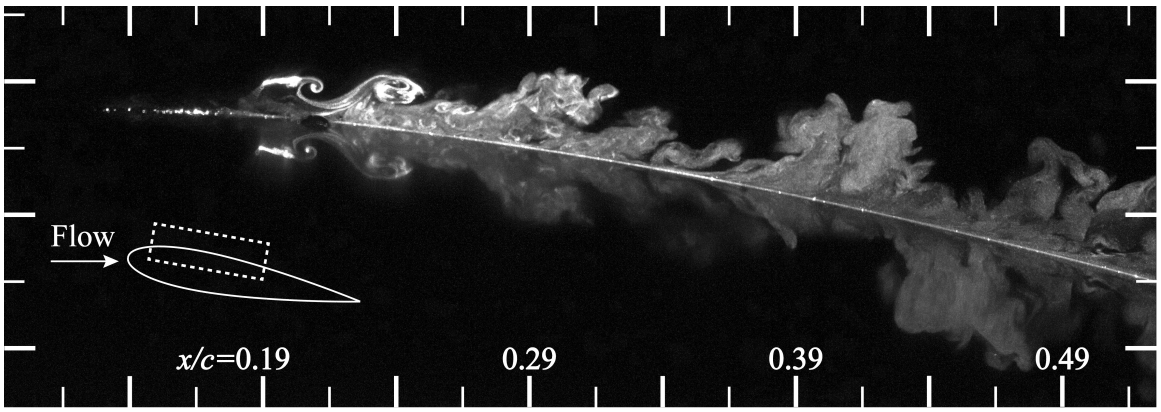


Figure 4.8: Side view separation bubble visualization for $\alpha = 10°$.

Figures 4.5-4.7, the smoke is initially smooth downstream of the wire, indicative of a laminar flow. Further downstream, the smoke begins to exhibit waviness, which is followed by roll-up vortices. These vortices convect downstream and eventually, transition to turbulence as confirmed by the increased mixing. Following breakdown, turbulent structures continue to convect downstream towards the trailing edge. Figure 4.8 shows a similar process, however, the roll-up of the separated shear layer occurs much closer to the smoke-wire. This figure also shows that smoke beneath the smoke-wire is entrained and carried away by reverse flow.

Figures 4.9-4.12 present top view images of the separation bubble visualizations. In each image, the direction of the free-stream is from top to bottom. The figures show the development of smoke after being evaporated across the span into the laminar portion of the separated layer as indicated by the clearly separated fine streaklines visible immediately downstream of the wire. Note that the smoke-wire is located outside the field of view at $\alpha = 0°$ (Fig. 4.9). Further downstream, the separated shear layer rolls up into spanwise-oriented vortices, which convect and break down into smaller structures. This breakdown along with the increased mixing of the smoke denotes the transition to turbulence. Furthermore, Figures 4.9-4.11 show that turbulent structures can be seen convecting towards the trailing edge. The visualizations qualitatively resemble previous smoke-wire visualizations performed over airfoils [63] and swept wings [65] with a smoke-wire placed upstream of the model.

The figures show that the streamwise position of roll-up moves upstream as the angle of attack is increased. Also, the spanwise coherence of the roll-up and transition location appears much stronger at $\alpha = 0$, 5, and 8° compared to at $\alpha = 10°$, which lies just ahead

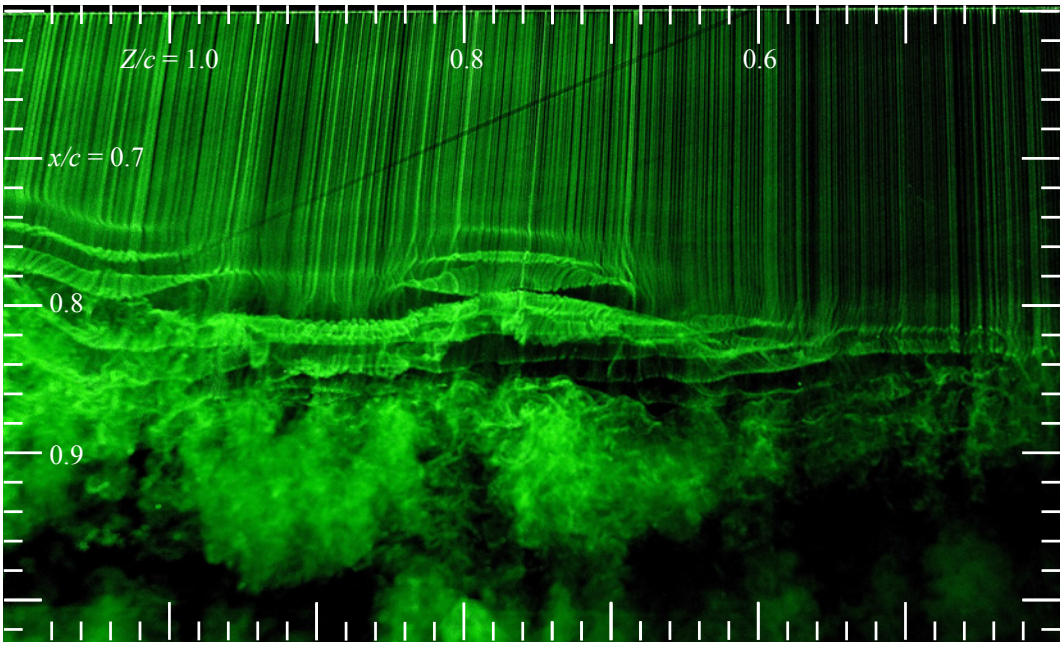


Figure 4.9: Top view separation bubble visualization for $\alpha = 0°$.

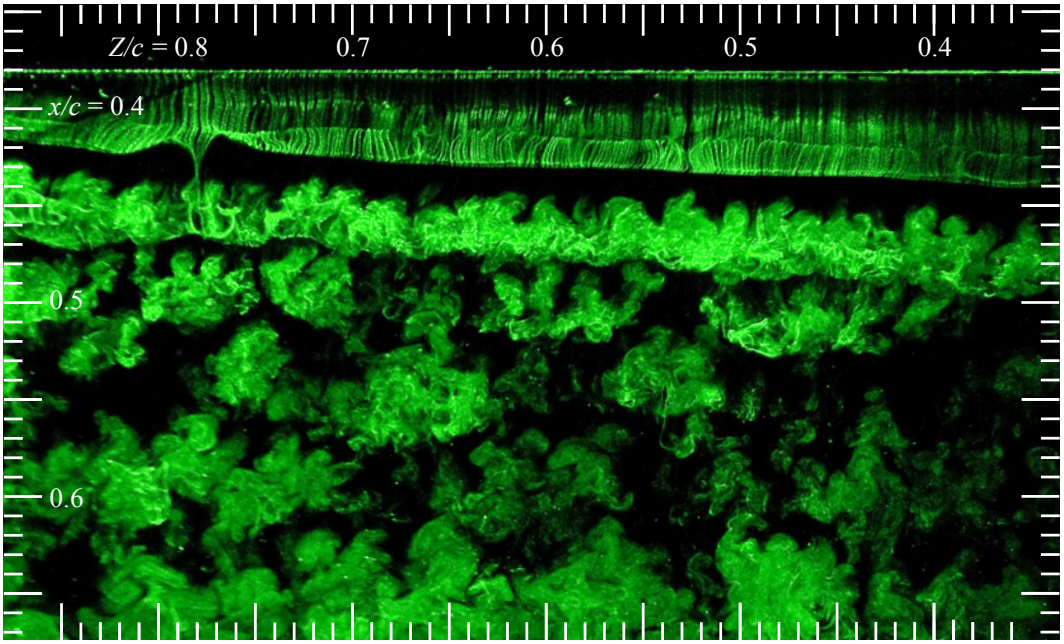


Figure 4.10: Top view separation bubble visualization for $\alpha = 5°$.

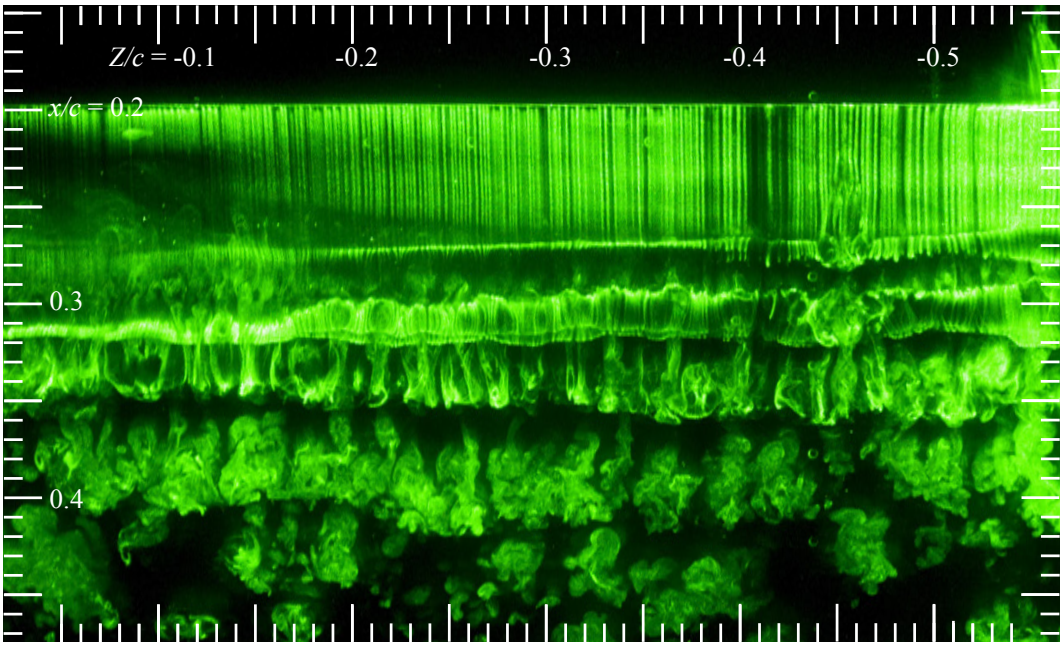


Figure 4.11: Top view separation bubble visualization for $\alpha = 8°$.

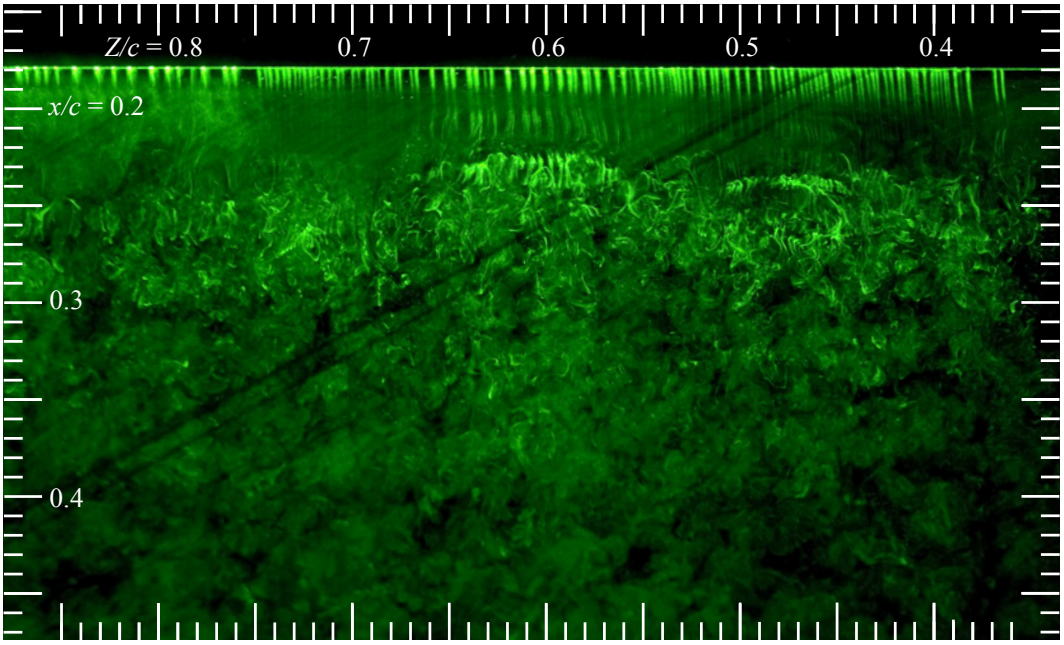


Figure 4.12: Top view separation bubble visualization for $\alpha = 10°$.

of stall. Similar observations may be made from the flow visualizations of the spanwise onset of transition for flow over a NACA66_3-018 airfoil presented by Batill [63]; however, in their case, the roll-up structures are not explicitly visualized. The decrease in the spanwise coherence of roll-up observed at $\alpha = 10°$ appears to be consistent with the observations of Balzer and Fasel [21], who showed that a less coherent roll-up is associated to increased reverse flow, which occurs at larger angles of attack. Figures 4.9-4.11 also show that the roll-up of vortices is slightly oblique. As the images were captured without end plates installed, this is attributed to a slight flow non-uniformity across the span, which occurs due to the influence of end effects [33].

The visualizations may also be used to investigate the development of roll-up vortices during transition. At $\alpha = 0°$, Figure 4.9 shows that a roll-up vortex, at $x/c = 0.82$, has begun to deform across the span ahead of transitioned structures at $x/c \approx 0.9$. At $\alpha = 5°$, Figure 4.10 displays the remnants of a spanwise vortex at $x/c \approx 0.45$, which features a row of mushroom-like turbulent structures spaced approximately $0.025c$ across the span. At $\alpha = 8°$, Figure 4.11 shows that slightly periodic dislocations are visible across a spanwise-coherent vortex developing at $x/c = 0.31$. Further downstream, at $x/c = 0.34$, a roll-up vortex has broken down into streamwise-oriented structures spaced approximately $0.02c$ across the span. Another row of streamwise-oriented structures is visible at $x/c \approx 0.38$, however, the increased mixing of the smoke around these structures indicates that, at this point, the flow has broken down to turbulence. At $\alpha = 10°$, roll-up vortices appear to break down rapidly with no discernible structures present within the images. The deformation of roll-up vortices ahead of transition is consistent with other studies on airfoils [14, 15]. The formation of streamwise-oriented structures during the breakdown of spanwise vortices has been also observed in studies on flat plates [25] and airfoils [15]. The presence of these streamwise-oriented structures has been linked to an instability forming within the braid region between vortices [15] and suggests that a similar mechanism may exist at $\alpha = 5$ and 8°. At $\alpha = 10°$, the rapid breakdown of disordered spanwise structures is typically observed at larger angles of attack [21, 63] and suggests that the flow is subject to an oblique breakdown [21].

4.2 Streamwise Flow Development

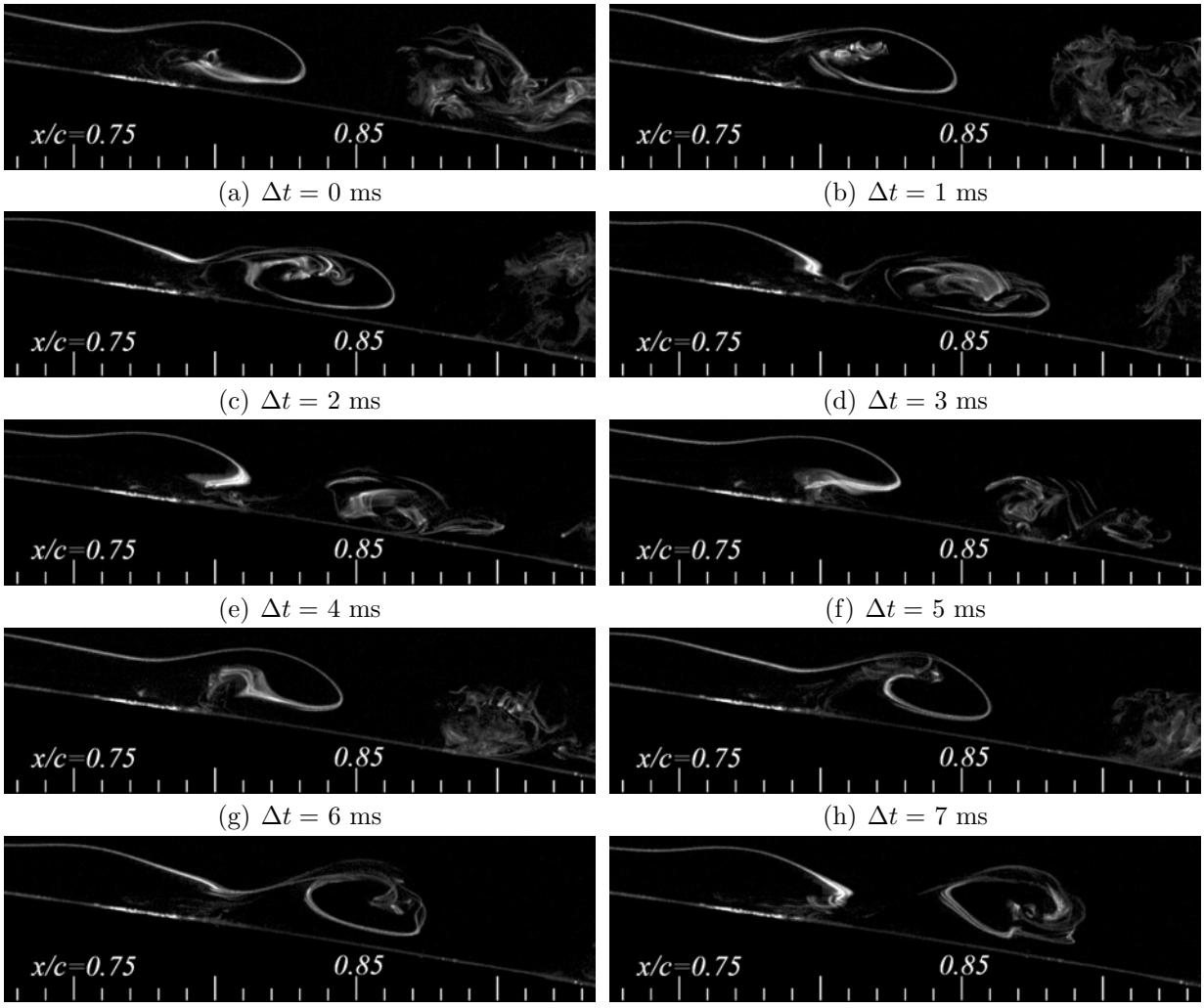
This section focuses on the streamwise development of the flow with an emphasis on the formation and development of shear layer vortices. Boundary layer measurements are compared to time-resolved flow visualizations to link quantitative measurements with unsteady phenomena occurring within the separation bubble.

4.2.1 High-Speed Flow Visualization

Figures 4.13-4.16 present sequences of flow visualizations depicting flow within laminar separation bubbles. In each image, the reflection of the smoke visible in Figures 4.9-4.12 has been masked for clarity. The sequences show that the separated shear layer rolls up into laminar vortices, which convect downstream and eventually breakdown to turbulence. The laminar-to-turbulent transition is marked by the increased mixing of smoke within the vortices. These transitioned structures convect downstream and form part of the re-developing turbulent boundary layer. The images demonstrate that the scale of the vortices decreases with increasing angle of attack with the average vortex diameter estimated at $D/c \approx 0.5$, 0.3, 0.2 and 0.1, for $\alpha = 0$, 5, 8, and 10°, respectively. This observed trend along with the approximate scale of the structures agrees with the observations of past studies on airfoils [14, 19, 21].

Figures 4.13-4.16 show that, following roll-up, shear layer vortices convect downstream and undergo a breakdown to turbulence. In some cases, interactions occur between vortices, which cause vortices to merge ahead of transition. Vortex merging was observed in high-speed videos to occur at $\alpha = 5$ and 8°. At $\alpha = 8°$, vortex merging occurs intermittently between 10% of roll-up vortices and the rest of the structures break down without such interactions. As shown later in Section 4.2.3, vortex merging involving up to three vortices occurs commonly at $\alpha = 5°$. Figure 4.14 demonstrates a sequence of triple vortex merging at $\alpha = 5°$, where three vortices are shed from the separated shear layer and join together between $0.42 \lesssim x/c \lesssim 0.48$. The merging of these structures precedes the laminar-to-turbulent breakdown of the structures. During this process, the first two vortices merge (Fig. 4.14d-f), while a third vortex is shed. The first two joined vortices are stretched at the surface as the third structure convects above (Fig. 4.14g-h). The mixing of smoke in the vicinity of the first paired vortices suggests that these structures have transitioned, while the third structure still appears laminar. Following this event, the merged structures continue to convect downstream (Fig. 4.14i-j) and eventually, the third merged vortex transitions as well. The convection and subsequent breakdown of roll-up vortices shown in the visualizations has also been observed in studies on airfoils [14, 15, 17, 19] and flat plates [13, 22, 25, 44]. This visualization (Fig. 4.14) shows the merging between three vortices, whereas previous studies on separation bubbles forming over airfoils [15] and flat plates [13, 25] have only observed vortex pairing. The visualizations at $\alpha = 5°$ are similar to those of vortex merging between three vortices within a plane mixing layer by [55].

The flow visualizations demonstrate where individual and merged structures break down above the airfoil model. While laminar-to-turbulent transition is typically described by a location (Fig. 2.2), the images show that laminar-to-turbulent breakdown occurs over a region. Furthermore, the extent of this transition region varies depending on the vortex.



(a) $\Delta t = 0$ ms (b) $\Delta t = 1$ ms

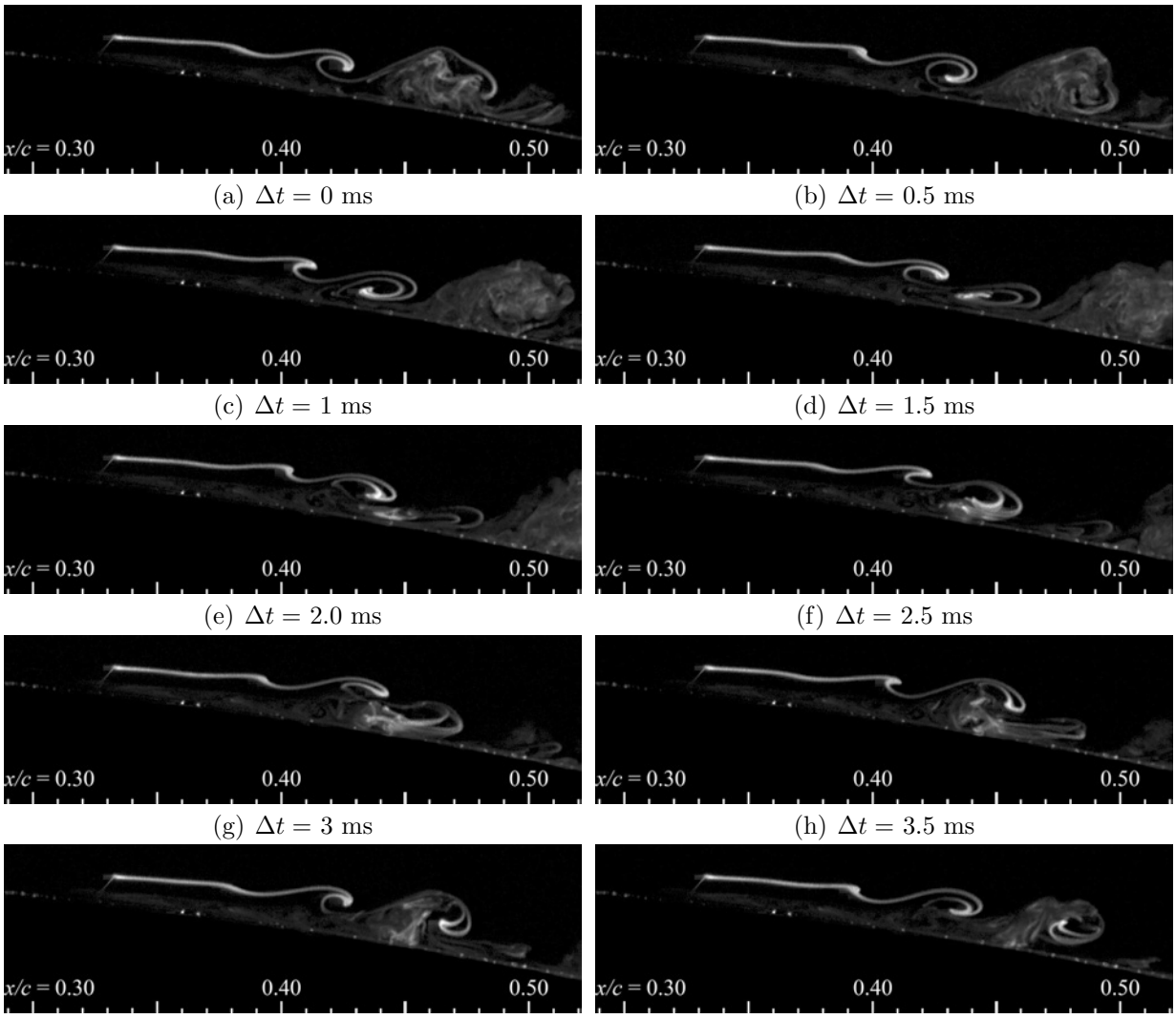
(c) $\Delta t = 2$ ms (d) $\Delta t = 3$ ms

(e) $\Delta t = 4$ ms (f) $\Delta t = 5$ ms

(g) $\Delta t = 6$ ms (h) $\Delta t = 7$ ms

(i) $\Delta t = 8$ ms (j) $\Delta t = 9$ ms

Figure 4.13: Sequence of high-speed images displaying vortex shedding at $\alpha = 0°$.



(a) $\Delta t = 0$ ms (b) $\Delta t = 0.5$ ms

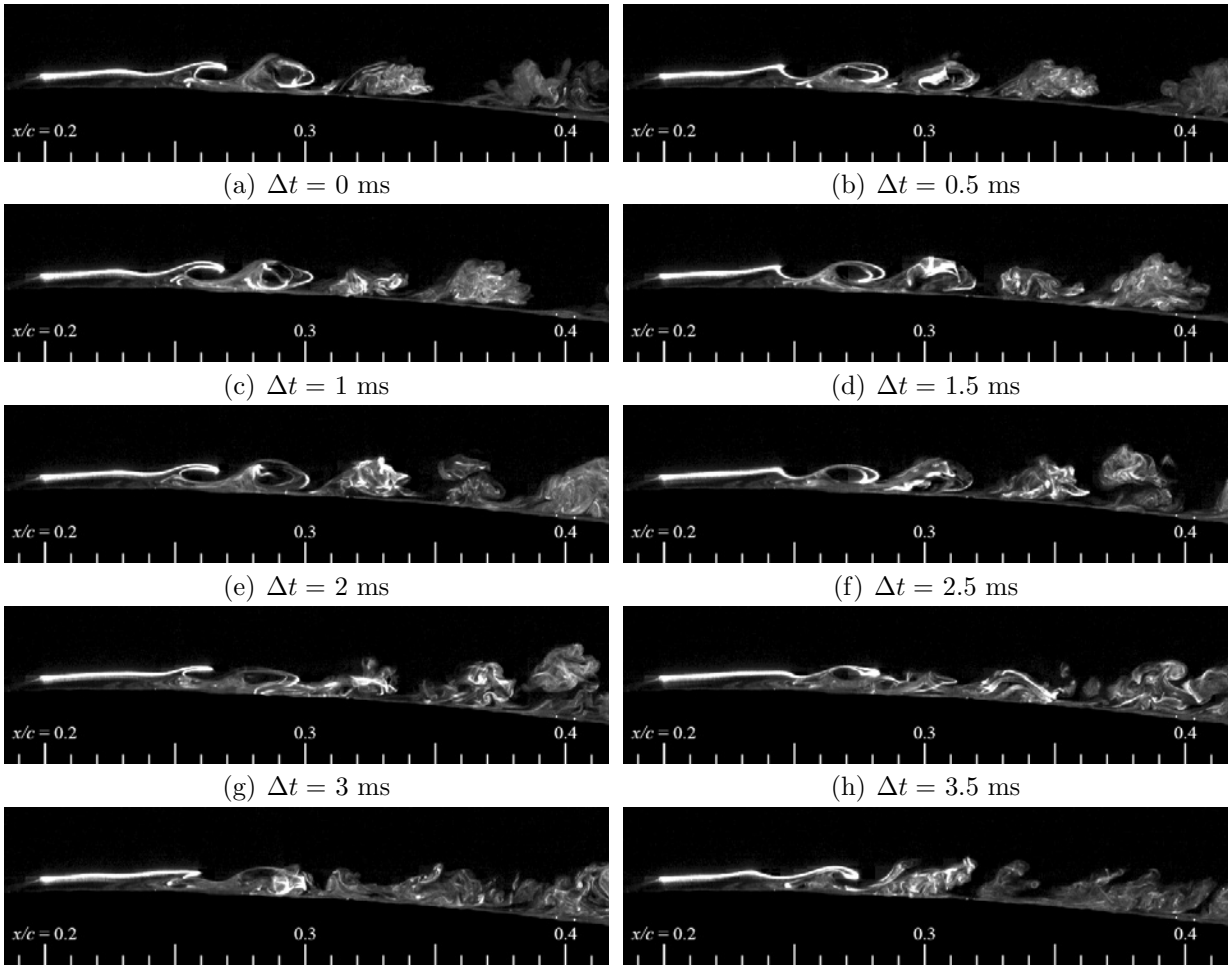
(c) $\Delta t = 1$ ms (d) $\Delta t = 1.5$ ms

(e) $\Delta t = 2.0$ ms (f) $\Delta t = 2.5$ ms

(g) $\Delta t = 3$ ms (h) $\Delta t = 3.5$ ms

(i) $\Delta t = 4$ ms (j) $\Delta t = 4.5$ ms

Figure 4.14: Sequence of high-speed images displaying triple vortex merging at $\alpha = 5°$.



(a) $\Delta t = 0$ ms (b) $\Delta t = 0.5$ ms

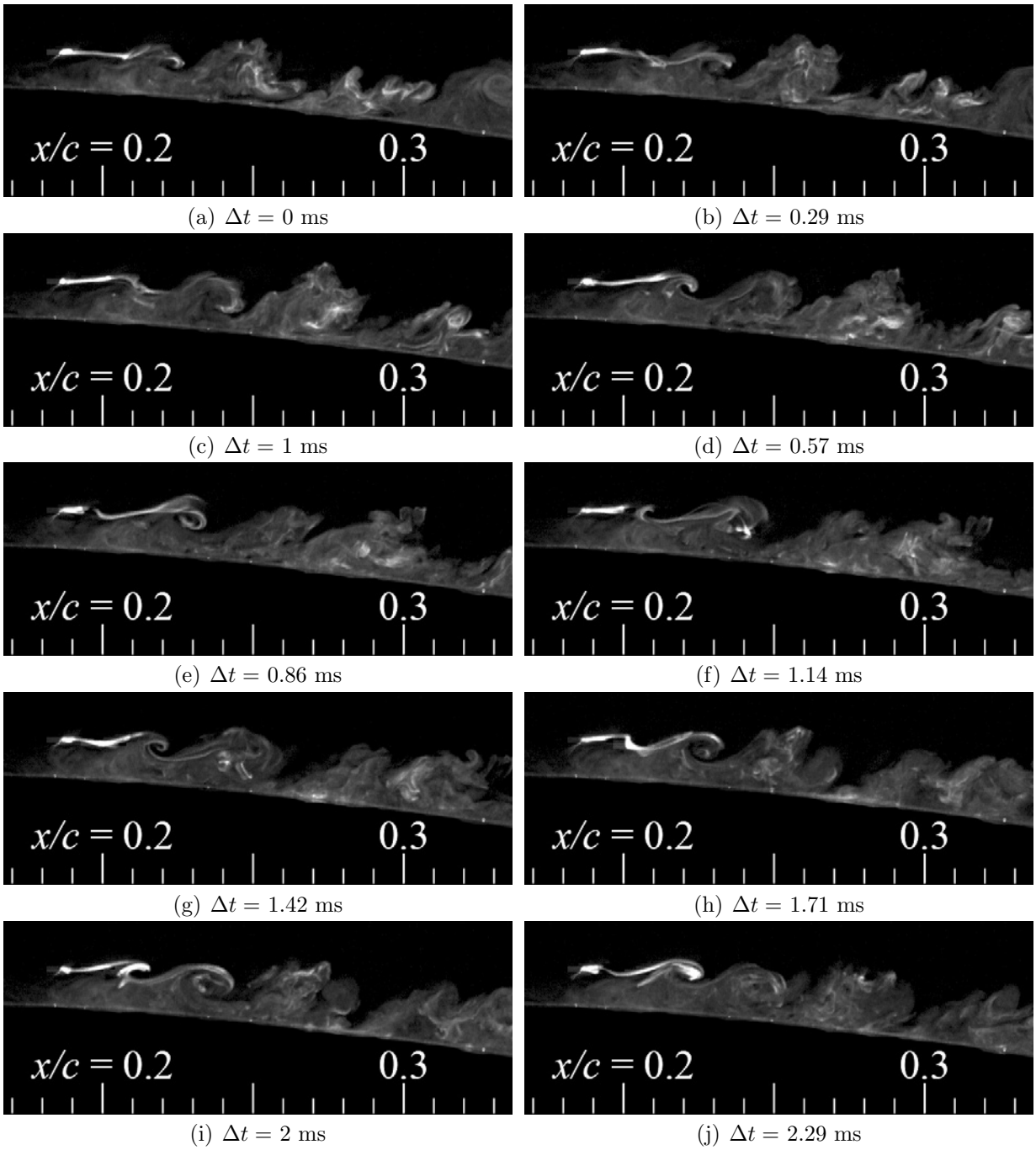
(c) $\Delta t = 1$ ms (d) $\Delta t = 1.5$ ms

(e) $\Delta t = 2$ ms (f) $\Delta t = 2.5$ ms

(g) $\Delta t = 3$ ms (h) $\Delta t = 3.5$ ms

(i) $\Delta t = 4$ ms (j) $\Delta t = 4.5$ ms

Figure 4.15: Sequence of high-speed images displaying vortex shedding at $\alpha = 8°$.



(a) $\Delta t = 0$ ms (b) $\Delta t = 0.29$ ms

(c) $\Delta t = 1$ ms (d) $\Delta t = 0.57$ ms

(e) $\Delta t = 0.86$ ms (f) $\Delta t = 1.14$ ms

(g) $\Delta t = 1.42$ ms (h) $\Delta t = 1.71$ ms

(i) $\Delta t = 2$ ms (j) $\Delta t = 2.29$ ms

Figure 4.16: Sequence of high-speed images displaying vortex shedding at $\alpha = 10°$.

For example, at $\alpha = 0°$ in Figures 4.13d-e, a vortex breaks down between $0.83 \lesssim x/c \lesssim 0.87$, while Figures 4.13h-j show a laminar structure convecting in this region. The rest of the high-speed videos show that vortices at $\alpha = 0°$ break down anywhere between $0.82 \lesssim x/c \lesssim 0.92$. At $\alpha = 5°$, the breakdown of single and merged vortices occurs between $0.42 \lesssim x/c \lesssim 0.5$. As demonstrated in Figure 4.15, the size of the transition region decreases at $\alpha = 8°$, as multiple vortices break down between $0.28 \lesssim x/c \lesssim 0.31$. Finally, at $\alpha = 10°$ (Figure 4.16), vortices are barely shed from the separated shear layer before they break down shortly downstream of the smoke-wire at $x/c \approx 0.23$. These results show that the extent over which shear layer vortices break down scales with the size of the structures and ultimately angle of attack.

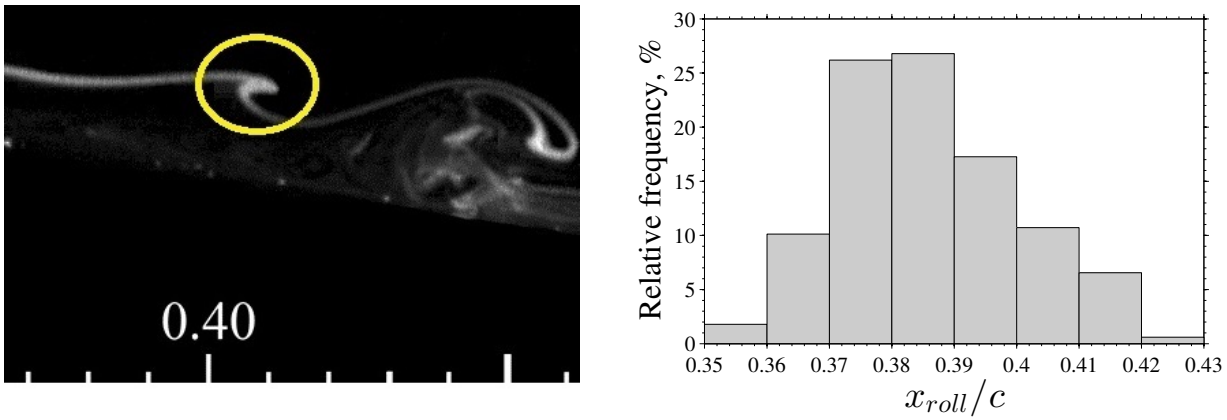
So far, the results show that angle of attack has a strong influence on the formation and development of vortices. While the results of this investigation are aligned with observations from past studies, as discussed in Appendix A.2, there is a a concern that the development of the flow $\alpha = 10°$ is affected by the smoke-wire. At this angle of attack, which lies just ahead of stall, the intrusiveness of the smoke-wire may be affecting the flow by causing it to transition prematurely. As a result of this concern, the focus of the rest of this study is primarily on the three lower angles of attack, where flow development is not as affected by the experimental setup.

A quantitative analysis of the flow visualization images was performed to estimate some salient characteristics of the formation and development of shear layer vortices, namely, the streamwise location of roll-up, x_{roll}, the vortex shedding frequency, $f_{shedding}$, and the drift speed of vortices, U_{drift}.

The streamwise location of roll-up, x_{roll}, was estimated by identifying a feature of the smoke within the separated shear layer that resembles a breaking wave [66]. Figure 4.17a presents an example of a breaking wave feature and when this feature appears in an image, the x/c position of the tip of the wave is used to estimate x_{roll}/c.

Figure 4.17b presents a histogram of roll-up locations x_{roll}/c at an angle of attack of $\alpha = 5°$. The histogram shows the estimated location of roll-up varies between $0.35 \leq x/c \leq 0.43$, which indicates that the roll up location varies over the airfoil. The histogram also suggests that the probability density of x_{roll} may be approximated with a normal distribution centred between $0.38 \lesssim x/c \lesssim 0.40$. Indeed, the mean roll-up location is estimated at $x/c \approx 0.395$ and this value lies within the bin with the largest frequency in the histogram. At $\alpha = 0$, 8 and 10°, roll-up occurs primarily between $0.76 \leq x/c \leq 0.78$, $0.24 \leq x/c \leq 0.26$ and $0.21 \leq x/c \leq 0.23$, respectively, and the extents of these roll-up regions are significantly smaller than at $\alpha = 5°$. Results presented later on in Section 4.2.3, will show that the large range of roll-up locations observed at $\alpha = 5°$ may be related to vortex merging.

The vortex shedding frequency, $f_{shedding}$, was estimated based on the number of instances



(a) (b)

Figure 4.17: (a) Example of a breaking wave used in streamwise roll-up position, x_{roll}/c, estimation and (b) relative frequency histogram of x_{roll}/c at $\alpha = 5°$.

of shear layer roll-up in a given time period and was performed for a minimum of sixty shedding cycles at each angle of attack. Figure 4.18a presents the vortex shedding frequency, as estimated from this method plotted against α. The plot shows a nearly linear increasing relationship between the vortex shedding frequency and α, which has been marked by a linear least-squares fit. The increase in $f_{shedding}$ with angle of attack agrees with trends observed by Burgmann and Schröder [14] over an SD7003 airfoil.

Figure 4.18b presents the Strouhal number of the vortex shedding computed from $St_{shedding} = f_{shedding}d/U_\infty$, where d is the model height projected onto the streamwise-normal plane. The data are plotted against the results of Burgmann and Schröder [14] for flow over an SD7003 airfoil at lower chord Reynolds numbers. Like $f_{shedding}$, the Strouhal number increases with angle of attack, which is consistent with the results of Burgmann and Schröder [14]. Figure 4.18b shows that the Strouhal number in the present study is significantly larger at similar angles of attack. If vortices are shed near a fundamental disturbance growth frequency, this difference may be related to the scaling of the frequency band of disturbance growth within the separated shear layer and is investigated later in this section.

The mean vortex drift velocity of roll-up vortices, U_{drift} was estimated with the same technique used by Burgmann and Schröder [14]. Following formation, individual vortex drift velocities were estimated by tracking the displacement of the center of the vortex between two frames and dividing the displacement by the period of between the frames

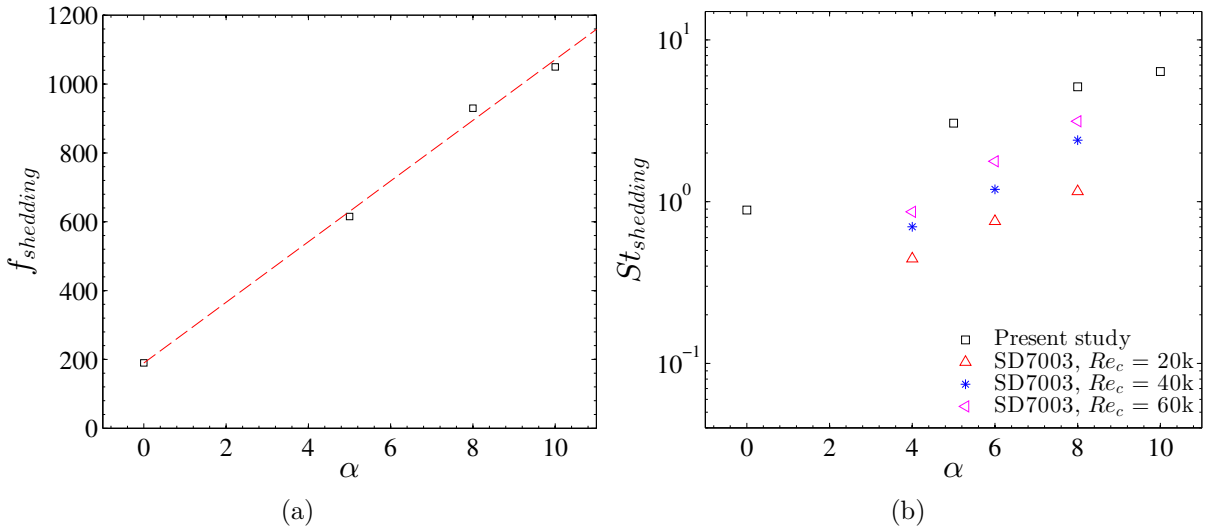


Figure 4.18: (a) Vortex shedding frequency plotted against α with linear least-squares line of best fit (– – –) and (b) vortex shedding Strouhal number plotted against α with data from an SD7003 airfoil computed from the results of Burgmann and Schröder [14].

(i.e. $\Delta x/\Delta t$). Figure 4.19a presents vortex drift speed nondimensionalized by free-stream velocity plotted against angle of attack. The plot shows that U_{drift} increases with angle of attack from $0.4\,U_\infty$ to $0.7\,U_\infty$. The data are plotted against the results of Burgmann and Schröder [14] that show the same increasing trend. The increase in drift velocities with α was attributed by Burgmann et al. [27] to be caused by an increase in shear due to the curvature of the airfoil. The magnitudes of U_{drift}/U_∞ at angles of attack of $\alpha = 5$, 8, and 10° fall within the same range as the results of Burgmann and Schröder [14] and Hain et al. [20] for flow over an airfoil and Pauley et al. [49] for flow over a flat plate. At $\alpha = 0°$, the estimated drift velocity is below $0.4U_\infty$, which is significantly lower than the results of past studies; however, there are no other studies that investigate such a low angle of attack.

Figure 4.19b presents vortex drift velocity normalized by the edge velocity within the laminar portion of the separation bubble, U_e^*, plotted against angle of attack. The edge velocity was estimated from the mean surface pressure coefficient (Fig. 4.20) acquired just upstream of the estimated transition location, x_R, with $U_e/U_\infty \approx \sqrt{1 - C_P}$ [7]. The plot shows that U_{drift} lies between 33 and 44 % of the separation bubble edge velocity, which falls within the range of surface pressure disturbance convection velocities obtained by Boutilier and Yarusevych [7] in a parametric study over the same model. These results

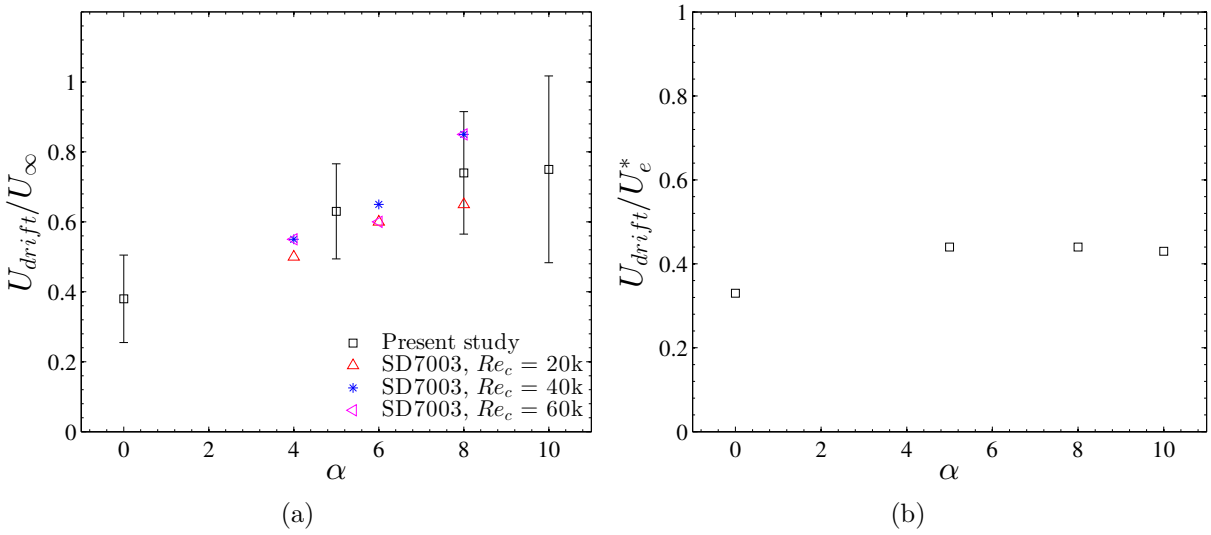


Figure 4.19: Drift speed of vortices, U_{drift}, nondimensionalized by (a) free-stream and (b) edge velocity. Error bars in (a) are representative of a 95 % confidence interval. Data for the SD7003 airfoil in (a) was obtained from Burgmann and Schröder [14].

imply that the drift speed of vortices does not depend on the maximum reverse flow speed but on other factors such as the vertical position of the separated shear layer Boutilier and Yarusevych [7].

Vortex drift velocities computed for individual vortices were subject to a substantial amount of scatter with the standard deviation of the convection velocities increasing from 10 to 20% of the free-stream velocity between $\alpha = 0$ and 10°. Large amounts of variation in vortex drift velocities were also observed by Burgmann and Schröder [14], and the results of Hain et al. [20] suggest that the drifting of roll-up vortices is an unsteady phenomenon over airfoils. The variation in these drift velocities is especially apparent in cases where vortex interactions lead to merging. An example of this is demonstrated in Figure 4.14 during triple vortex merging. The sequence shows that when two vortices merge, the first shed vortex convects slowly and decelerates to a near halt. The second vortex is then accelerated over the first vortex as they merge, and a similar process occurs when the third vortex convects over the paired structures. This suggests that the structures which lead to vortex merging have the same effect as displacing the wall such that the vortices which follow are accelerated above them.

In this section, flow visualizations have demonstrated that vortices are formed within

the separated shear layer over the suction side of a NACA0018 airfoil. Following their formation, these vortices convect downstream, and break down to turbulence. The initial roll-up of the separated shear layer occurs two-dimensionally at lower angles of attack and is less coherent across the span at an angle ahead of stall ($\alpha = 10°$). The flow visualizations demonstrate that vortices deform across the span ahead of breakdown, and that in some cases, streamwise-oriented structures are generated during breakdown. The flow visualizations and the results of a quantitative analysis show that the formation and development of vortices is dependent on angle of attack and the results of this analysis are summarized in Table 4.1. The results show that increasing the angle of attack has the effect of reducing the scale of vortices, which results in smaller breakdown regions. Increasing α also causes the vortex shedding frequency and mean drift velocity to increase. Also, at some angles of attack, vortices may interact, which leads them to merge then break down to turbulence.

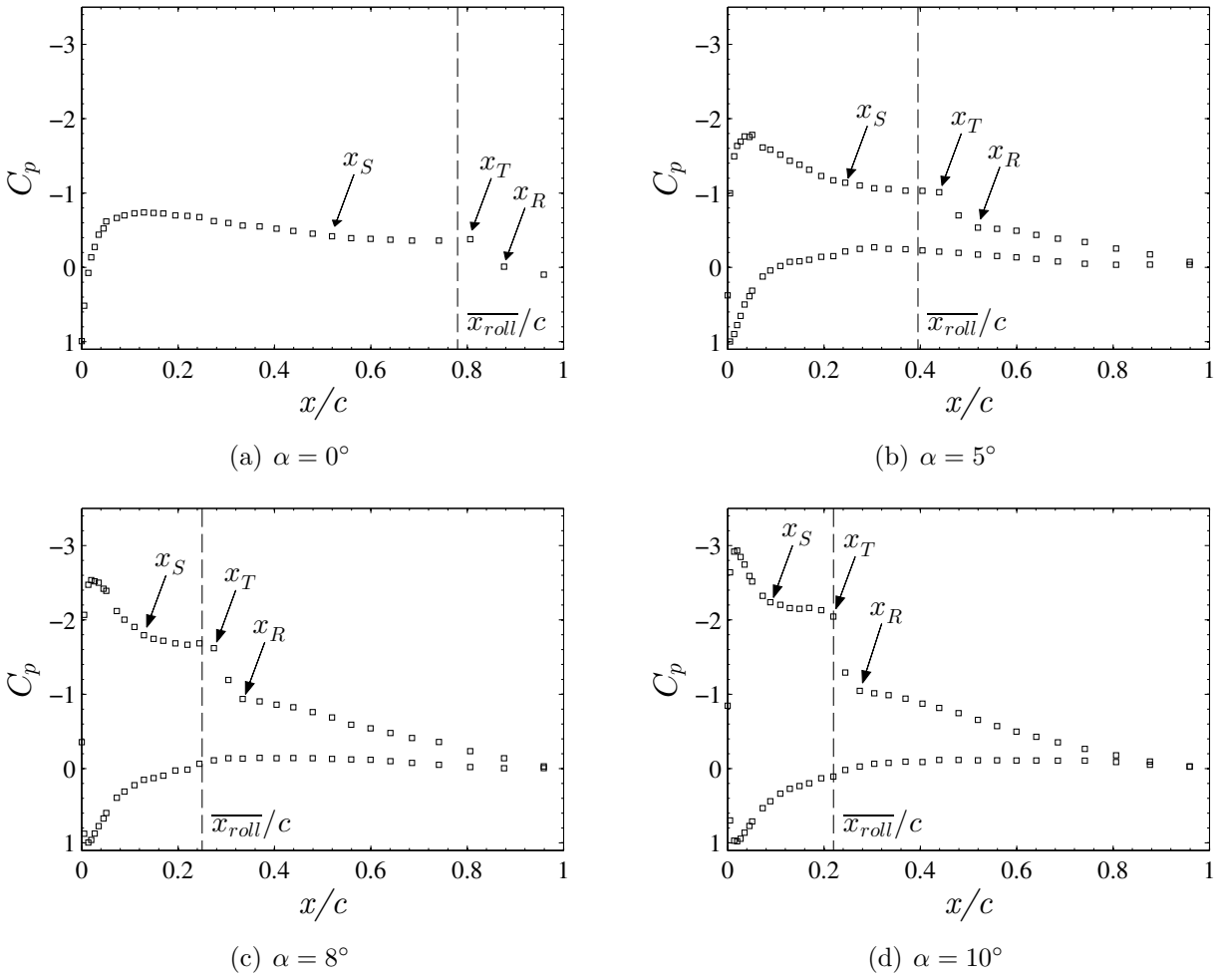
Table 4.1: Summary of data obtained from side view high-speed visualizations.

	$\alpha = 0°$	$\alpha = 5°$	$\alpha = 8°$	$\alpha = 10°$
U_e/U_∞	1.17	1.42	1.64	1.77
D/c	0.05	0.03	0.02	0.01
$f_{shedding}$, Hz	190	615	930	1050
U_{drift}/U_∞	0.38	0.63	0.74	0.75
U_{drift}/U_e	0.33	0.54	0.64	0.65
$\overline{x_{roll}}/c$	0.78	0.40	0.25	0.22

4.2.2 Boundary Layer Measurements

Boundary layer measurements, including static pressure measurements, microphone measurements, and hot-wire measurements were performed with end plates installed on the airfoil model (Fig. 3.2). These measurements were processed to describe the flow development over the airfoil model through a combination of statistical, spectral, and cross-correlation analysis. The results of these measurements are compared to the results of the high-speed flow visualization sequences presented in Section 4.2.1.

Surface pressure measurements were performed to estimate the separation bubble formation region at each angle of attack. Figure 4.20 presents model surface pressure distributions acquired over the suction and pressure sides of the airfoil. For clarity, only



(a) $\alpha = 0°$

(b) $\alpha = 5°$

(c) $\alpha = 8°$

(d) $\alpha = 10°$

Figure 4.20: Model surface pressure distributions with estimated mean separation, transition, reattachment, and roll-up locations marked by x_S, x_T, x_R, $\overline{x_{roll}/c}$, respectively.

the surface pressure distribution along the suction side of the model is presented at $\alpha = 0°$ (Fig. 4.20a). Following the point of minimum pressure, a region of nearly constant pressure indicates the presence of a separation bubble [67]. This allows for mean separation, transition, and reattachment locations to be estimated from the distributions [34, 67]. Using the procedure described in Boutilier and Yarusevych [7], the separation and transition points were estimated by identifying the bounds of the pressure plateau. Following the point of transition, a strong pressure recovery precedes the point of reattachment, which is followed by a more gradual pressure recovery towards the trailing edge. The estimated separation, transition, and reattachment locations are marked in each plot by x_S, x_T, and x_R, respectively, and are presented in Table 4.2. These transition and reattachment locations were verified at $\alpha = 5$ and 8° through hot-wire velocity profiles and streamwise velocity spectra. The deviations between estimated separation, transition, and reattachment locations were within the spatial resolution of the pressure taps, which was used to estimate the uncertainty bounds included for these parameters in Table 4.2. The mean streamwise locations of roll-up, $\overline{x_{roll}}/c$, obtained from high-speed image sequences are also shown on the plots. The figures show that mean roll-up locations lie just upstream of the mean transition location obtained from the surface pressure distributions.

Figure 4.21a presents the estimated separation, transition, reattachment and roll-up locations for each α. This plot highlights common trends regarding the positioning of separation bubbles over airfoils at low Reynolds numbers [7, 34]. The estimated separation, transition, and reattachment points each move upstream with increasing α. The extent to which the separation point moves upstream is less than that of reattachment such that separation bubble length decreases with increasing α (Fig. 4.21b).

Figure 4.21b presents the separation bubble length, L, the distance between separation and transition, $(x_T - x_S)$, and the distance between transition and reattachment $(x_R - x_T)$, plotted against α. The figure demonstrates that, as α is increased from 0° to 10°, the separation bubble length halves from $0.36c$ to $0.18c$. In Figure 4.21a the distance between

α, degrees	x_S/c	x_T/c	x_R/c
0	0.52 ± 0.02	0.80 ± 0.035	0.88 ± 0.04
5	0.24 ± 0.015	0.44 ± 0.02	0.52 ± 0.02
8	0.13 ± 0.01	0.27 ± 0.015	0.33 ± 0.018
10	0.09 ± 0.01	0.22 ± 0.013	0.27 ± 0.015

Table 4.2: Mean separation, x_S , transition, x_T, and reattachment, x_R, locations estimated from surface pressure distributions with the range of measurement uncertainty based on the spatial resolution of static pressure taps.

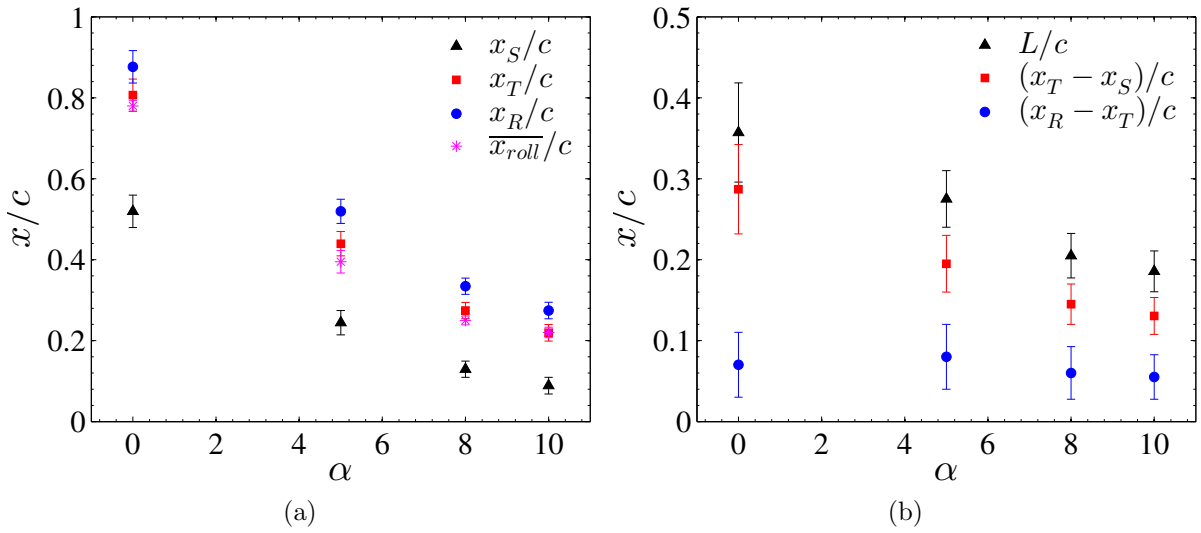


Figure 4.21: (a) Mean separation, transition, and reattachment locations and (b) separation bubble length estimated from surface pressure distributions. Error bars are computed based on the spatial resolution of static pressure taps.

separation and transition decreases significantly with increasing α, while the distance between transition and reattachment changes slightly between 5.5% and 7.0% of the chord. This shows that the decrease in separation bubble length is primarily due to the shortening of the distance between mean separation and transition locations, which has been associated with increased spatial disturbance amplification rates at larger angles of attack [7].

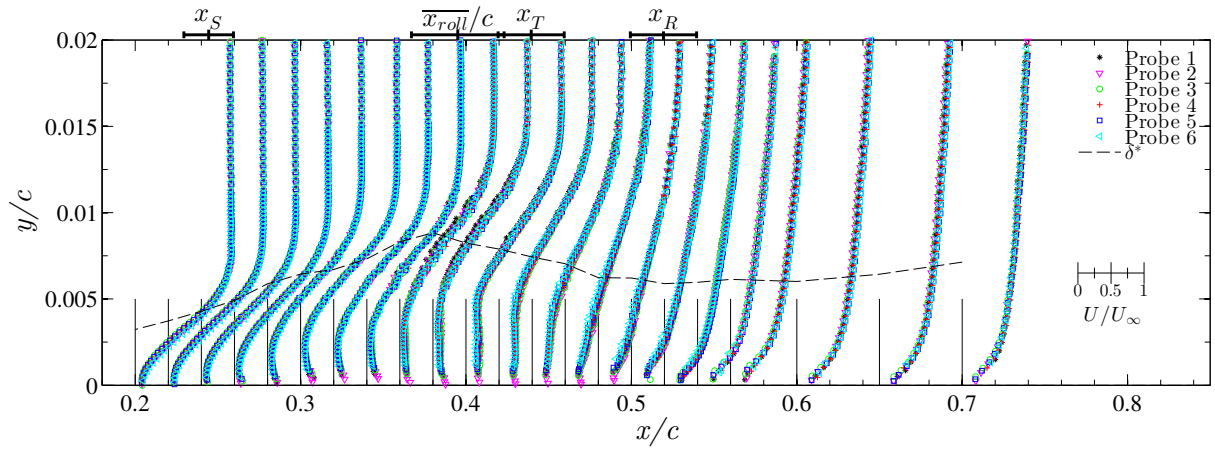
Velocity profiles were obtained with the rake of hot-wires at $\alpha = 5$ and 8° over the suction side of the airfoil. Additional velocity measurements were acquired at multiple streamwise locations at $\alpha = 0$, 5, and 8° with the rake placed at the displacement thickness, $y = \delta^*$. The additional measurements were performed at $y = \delta^*$ as the displacement thickness corresponds approximately to the location of maximum RMS velocity, but being an integral parameter, is less prone to data scatter in the region of maximum fluctuations [12]. At $\alpha = 5$ and 8°, δ^*, at each x/c location, was obtained by taking the average of the displacement thickness computed from mean velocity profiles acquired by each probe in the rake. For $\alpha = 0°$, the displacement thickness locations were obtained from the results of Boutilier [43] performed at the same experimental conditions, resulting in matching surface pressure distributions. The displacement thickness in the present study and in Boutilier [43] was computed by integrating the velocity profiles from the wall to the location of the edge

velocity, $\delta^* = \int_0^{\delta_e}(1 - U/U_e)\mathrm{dy}$. The edge velocity, U_e, was taken as the maximum velocity in the velocity profiles and the velocity at the wall was taken as zero following the no-slip condition.

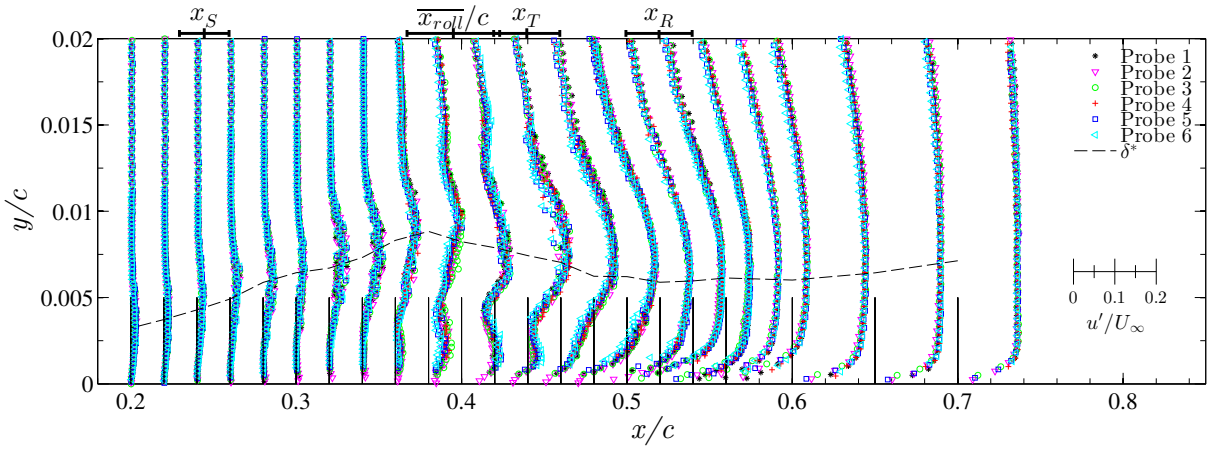
Velocity measurements were performed over the suction side of the airfoil in order to acquire the velocity field and study the growth of disturbances spatially. Figures 4.22 and 4.23 present mean and RMS velocity profiles acquired by the rake of hot-wire probes over the suction side of the airfoil at $\alpha = 5°$ and 8°, respectively. The estimated locations and error bars of separation, transition, and reattachment, as determined from surface pressure distributions, are marked on the plots. The mean roll-up location is also marked with error bars. The streamwise variation of δ^*, is represented on the plot by a dashed line.

At each measurement location, the mean velocity profiles (Figs. 4.22a and 4.23a) display good agreement between all probes, with minor variation being within the range of experimental uncertainty. While normal hot-wire measurements cannot detect the direction of the flow, reverse flow regions in the upstream portion of the separation bubble can be estimated from vertical extents of nearly stagnant positive flow near the wall [12, 22]. Figure 4.22a shows that at $\alpha = 5°$ this region begins at $x/c \approx 0.22$ and ends at $x/c \approx 0.38$ where it extends up to $y/c = 0.005$. Further downstream, in the aft portion of the separation bubble, shear layer roll-up causes the normal hot-wires to measure stronger vertical components of velocity. This results in increased near-wall velocity measurements, which grow downstream. The increase in near-wall velocities makes it difficult to detect reverse flow and accurately estimate the mean reattachment location. Still, if mean reattachment is defined as where the reverse flow region ends [40], reattachment appears to occur at approximately $x/c \approx 0.5$ marking the end of the separation bubble. Downstream of reattachment, a typical turbulent boundary layer profile develops towards the trailing edge [40]. In Figures 4.22a and 4.23a, velocity measurements, corresponding to the separated shear layer and free-stream, are visible above the reverse flow in the profiles obtained within the separation bubble. The plots show that the displacement thickness of each profile, where additional velocity measurements were performed, lies within the separated shear layer. When compared the near-wall measurements, these measurements are subject to fewer sources of error, which allows then to be use with confidence in quantitative analysis [12, 22, 42].

The RMS velocity profiles (Fig. 4.22b and Fig. 4.23b) show that disturbances are amplified within the separated shear layer prior to transition. At $\alpha = 5$, the growth of a peak is visible within the shear layer near δ^* and at $x/c = 0.36$, an additional peak begins to emerge near the wall. This also occurs at $\alpha = 8°$, where a second peak can be seen as of $x/c = 0.24$. The growth of disturbances within the separated shear layer is accompanied with an increase in data scatter, which is partly attributed to measurement errors [60] and

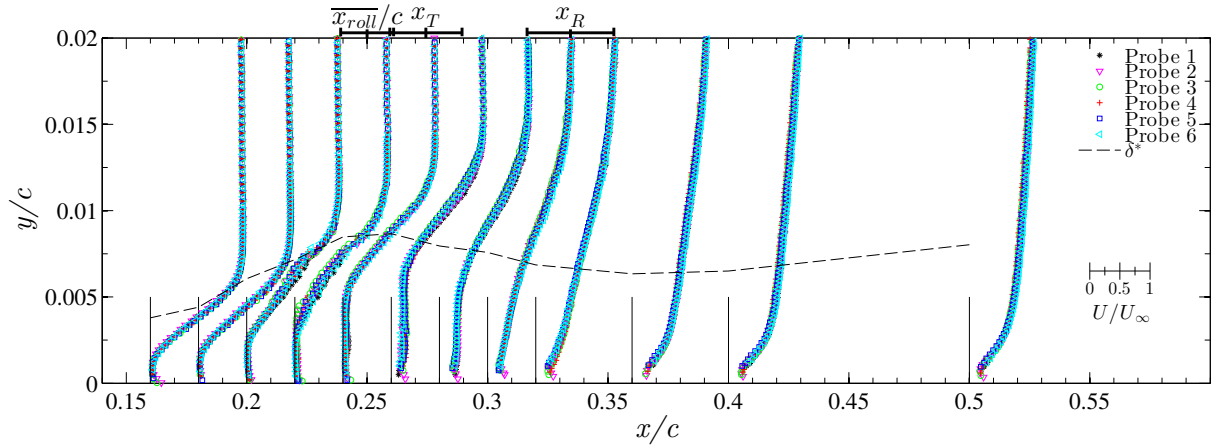


(a)

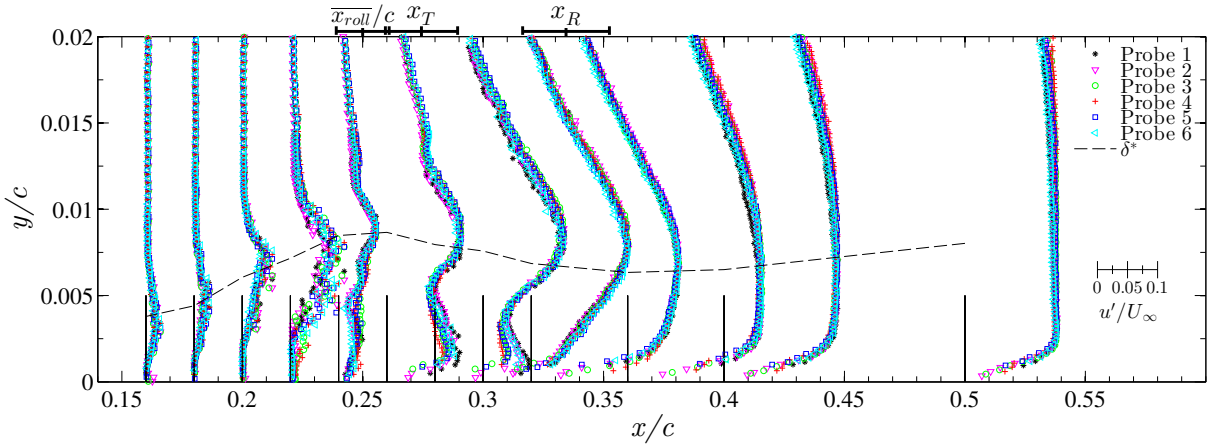


(b)

Figure 4.22: Streamwise development of (a) mean and (b) RMS velocity profiles obtained with the rake of hot-wires at $\alpha = 5°$. Mean separation, transition, and reattachment locations estimated from surface pressure distributions are marked by x_S, x_T, and x_R along with $\overline{x_{roll}}$ and their respective error bars. The average displacement thickness, δ^*, is marked by the dashed line (– – –).



(a)



(b)

Figure 4.23: Streamwise development of (a) mean and (b) RMS velocity profiles obtained with the rake of hot-wires at $\alpha = 8°$. Mean separation, transition, and reattachment locations estimated from surface pressure distributions are marked by x_S, x_T, and x_R along with $\overline{x_{roll}}$ and their respective error bars. The average displacement thickness, δ^*, is marked by the dashed line (– – –).

partly to the spanwise variation of flow development during the later stages of transition as seen in the flow visualizations (Figs. 4.10-4.11). The increased data scatter persists in the aft portion of the separation bubble close to the wall, following the trajectory of the transitional shear layer as it reattaches to the surface. Within the separation bubble, the y/c locations of the maximum disturbance amplitude lies approximately at the displacement thickness, which also corresponds to inflection points within the separated shear layer [12]. The plots show that shear layer roll-up occurs within the separation bubble at approximately the location of the maximum displacement thickness. This implies that shear layer roll-up is caused by a Kelvin-Helmholtz instability initiated by a strong velocity gradient ($\partial U/\partial y$) within the separated shear layer.

Mean velocity profiles may be used to estimate mean separation, and reattachment locations, while boundary layer parameters obtained from these profiles may estimate the approximate location of transition. The separation point may be defined where the wall shear stress vanishes, whereas the reattachment point is effectively a stagnation point more commonly defined as the point where reverse flow vanishes [40]. On the other hand, the location of transition is somewhat arbitrary, and has previously been defined as the location of the maximum displacement thickness, δ^*, within the separation bubble [42]. The accuracy of determining separation and reattachment points through hot-wire velocity profiles is dependent on the spatial resolution of the profiles and the accuracy of near-wall velocity measurements. In particular, the near-wall measurements are prone to low-speed calibration errors [22, 56], rectification errors [22], and an overestimation of velocities due to heat conduction for probes near or at a wall [68]. Combined with the spatial resolution of the profiles, these factors makes it inherently difficult to accurately determine the mean separation and reattachment locations. Also, the locations extracted from these techniques are mean quantities, while separation bubbles are a time-varying phenomena, which means that these locations are unsteady [14, 20, 26]. The velocity profiles obtained at $\alpha = 5^\circ$ show separation at $x/c \approx 0.22$, while at $\alpha = 8^\circ$ the measurements were not taken sufficiently upstream to resolve this point. The location of separation at $\alpha = 5^\circ$ is slightly upstream of the position estimated from the surface pressure distributions, however, it falls within the spatial resolution of those measurements. Also, the results presented in Appendix B.2, suggest that placing the rake of hot-wire probes in the fore portion of the separation bubble causes the separation point to shift slightly upstream. At $\alpha = 5$ and 8°, the mean velocity profiles show reattached flow with no reverse flow at $x/c = 0.52$ and $x/c = 0.31$, respectively. These results are also within the spatial resolution of the reattachment points estimated from the surface pressure distributions.

Figure 4.24 presents boundary layer parameters computed from the mean velocity profiles. Above each plot, the estimated separation, transition, and reattachment locations obtained from the surface pressure distributions are marked on the plot with the superscripts

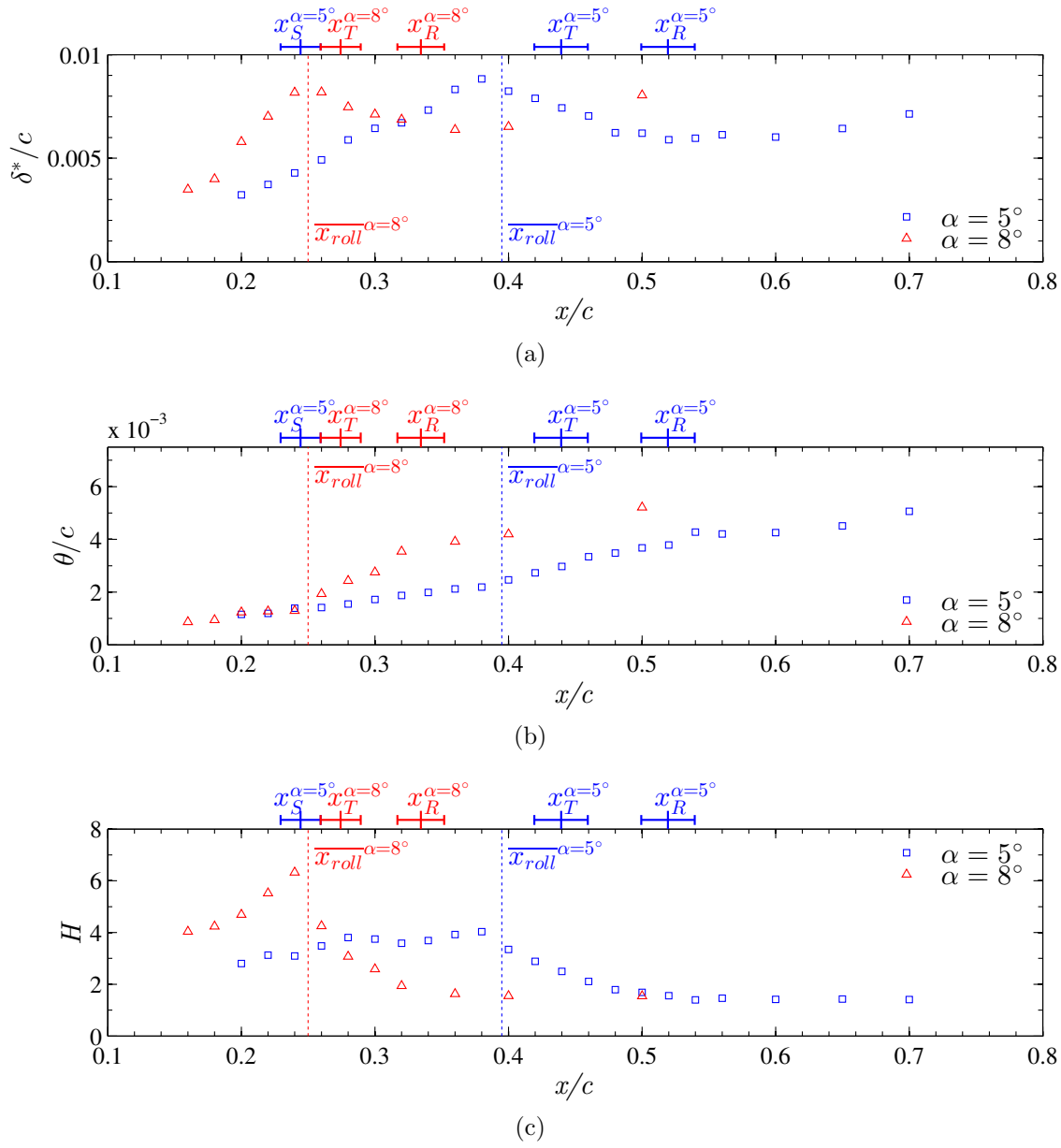


Figure 4.24: Streamwise development of (a) displacement thickness, (b) momentum thickness, and (c) shape factor marked with mean separation (x_S), transition (x_T), and reattachment (x_R) locations and their respective error bars. The mean shear layer roll-up location ($\overline{x_{roll}}$) is also marked by the dashed lines.

denoting α. These labels include error bars computed from the spatial resolution of the surface pressure taps. The mean roll-up location for each α is also marked on the plots. The momentum thickness of each mean velocity profile was computed by integrating the velocity profiles from the wall to the location of the edge velocity, $\theta = \int_0^{\delta_e} U/U_e(1 - U/U_e)\mathrm{dy}$. The boundary layer shape factor, H, was computed from the ratio of the displacement thickness and momentum thickness at each x/c location. Like the displacement thickness, both these parameters were computed individually for each profile obtained with the probes in the rake, then averaged at each x/c location.

Figure 4.24a presents the streamwise development of the displacement thickness. Following separation, the displacement thickness grows until transition, when the newly energized turbulent separated shear layer regains momentum and proceeds to reattach, causing the vertical extent of the reverse flow region to decrease [42, 43]. Following the reattachment of the separated shear layer, δ^* grows towards the trailing edge as the turbulent boundary layer develops. Figure 4.24a shows that, for both the cases presented, the peak of δ^* lies slightly upstream of the location of transition estimated from the surface pressure distributions. Instead, it is the mean locations of shear layer roll-up, $\overline{x_{roll}}/c$, located at at 0.25 and 0.395 for $\alpha = 5$ and 8°, respectively, that are located approximately at these peaks. This suggests that the decrease in the displacement thickness is linked to the roll-up of the separated shear layer, which precedes transition.

Figure 4.24b presents the streamwise development of the momentum thickness. Following separation, the momentum thickness grows downstream towards the trailing edge. At the location of the maximum displacement thickness and $\overline{x_{roll}}/c$, the growth rate of the momentum thickness increases following the introduction of roll-up vortices, which implies that shear layer roll-up contributes to the enhanced momentum exchange caused by transition. At approximately the location of mean reattachment, the rate of streamwise increase of θ decreases as a turbulent boundary layer redevelops towards the trailing edge.

Figure 4.24c presents the streamwise development of the shape factor, H. Downstream of separation, the shape factor increases until $x/c = 0.38$ and 0.24 for $\alpha = 5$ and 8°, respectively. At both angles of attack, the beginning of a sharp decrease in H coincides approximately with $\overline{x_{roll}}/c$ and this decrease persists up until mean reattachment, after which the shape factor remains nearly constant. The magnitude of the peak of H increases from 4.0 to 6.5 as α is increased from 5 to 8°. The magnitudes of these peak values of H are similar to those obtained in studies on flat plates [69] and airfoils [14, 42, 43]. Past studies have associated larger shape factors with larger growth rates [10], which result in a more rapid transition and a shorter separation bubble, as shown in Figure 4.21b. However, the results of Boutilier [43] at the same experimental conditions show that H is larger at $\alpha = 0°$ than at $\alpha = 5°$, which shows that this is not always true.

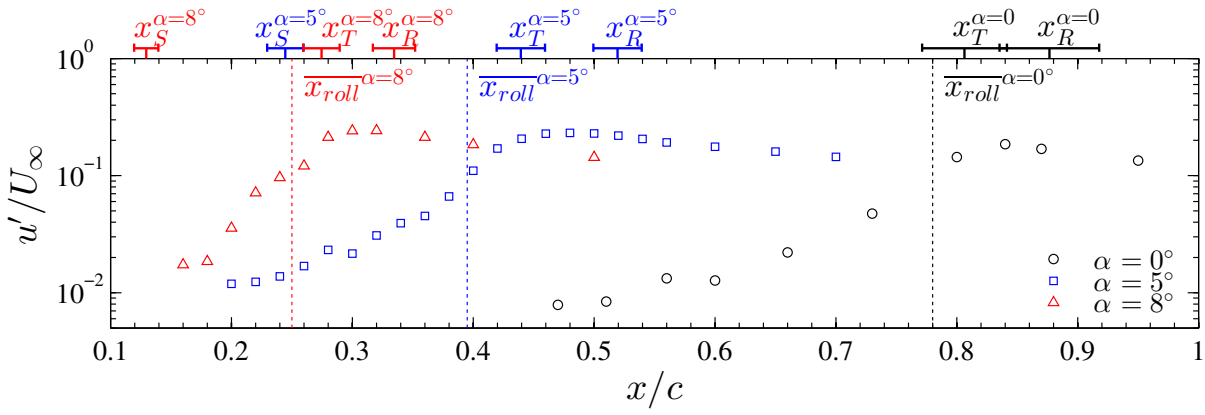
Overall, the trends in the streamwise development of the boundary layer parameters

presented is qualitatively similar to results obtained in past studies on airfoils [12, 42] and flat plates [70]. While past studies have used specific features present within the streamwise development of these parameters to estimate the location of transition, the results of this investigation suggest these features may be used to locate where shear layer roll-up occurs, which marks the onset of later stages of transition.

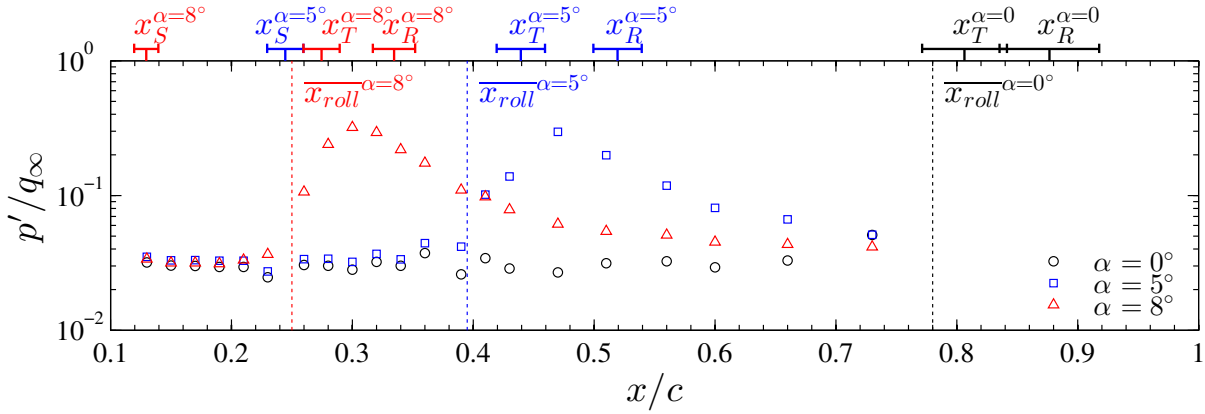
Figure 4.25 presents the streamwise development of the RMS velocity obtained by Probe 1 in the rake at $y = \delta^*$ and the RMS fluctuating surface pressure obtained with the embedded microphones at $\alpha = 0$, 5, and 8°. Separation, transition, and reattachment points obtained from the surface pressure distributions are marked with superscripts denoting α. The mean roll-up position is also marked for each α. Figure 4.25a shows that, downstream of mean separation, the RMS velocity increases until shortly after x_T with saturation occurring between x_T and x_S at $x/c = 0.84$, 0.46, and 0.3 at $\alpha = 0$, 5, and 8°, respectively. Following saturation, the RMS velocity remains nearly constant until mean reattachment. Downstream of saturation, the magnitude of the RMS velocity decays gradually as the turbulent boundary layer redevelops towards the trailing edge. This decrease in the RMS velocity is caused by the energy content spreading vertically as the enhanced mixing of the turbulent boundary layer entrains fluid from the free-stream [71]. At each α, the shape of the streamwise development of the RMS velocity agrees qualitatively with previous studies on unforced airfoils at low Reynolds numbers [12, 19, 72]. From $\alpha = 0$ to 8°, the maximum value of u'/U_∞ increases from 0.19 to 0.25. The same trend was observed by Boutilier and Yarusevych [12] over the same model; however, this differs from the results of Yarusevych [72] for flow over a NACA0025 airfoil, which shows an increase in u'/U_∞ with decreasing α.

The streamwise development of u' allows for trends regarding the type of disturbance growth to be extracted. Figure 4.25a shows that, initially, the growth rate of disturbances is nearly exponential until u'/U_∞ reaches approximately 0.1, after which, the growth rate drops and becomes essentially nonlinear. The results show that $\overline{x_{roll}}/c$ corresponds to the location where the rate of initial streamwise growth of u' becomes non-linear. This indicates that $\overline{x_{roll}}/c$ marks the commencement of nonlinearities and the later stages of transition. The formation of vortices at the onset of nonlinearities in disturbance growth agrees with the observations of Marxen et al. [13] in their DNS of a flat plate. Furthermore, the magnitude of u'/U_∞ at the onset of roll-up is similar to past studies on airfoils [27] and on flat plates [13]. This suggests that shear layer roll-up is triggered when disturbances reach a certain amplitude and that there may be similarities between geometries.

The streamwise development of the RMS fluctuating surface pressure (Fig. 4.25b) exhibits similar trends to the RMS velocity (Fig. 4.25a). Following mean separation, the RMS fluctuating pressure is nearly constant. Further downstream, the RMS pressure begins to increase gradually between $0.21 \leq x/c \leq 0.23$ and $0.36 \leq x/c \leq 0.39$ at $\alpha = 5$ and 8°,



(a)



(b)

Figure 4.25: Streamwise development of (a) RMS velocity measured by Probe 1 at $y = \delta^*$ and (b) RMS fluctuating surface pressure. The plots are marked with mean separation (x_S), transition (x_T), and reattachment (x_R) locations and their respective error bars. The mean shear layer roll-up location ($\overline{x_{roll}}$) is also marked by the dashed lines.

respectively, after which the streamwise growth rate increases significantly. Following this growth, p' saturates at approximately $0.3q_\infty$ at $x/c = 0.3$ and 0.47 for $\alpha = 5$ and 8°, respectively. These points lie between x_T and x_R and downstream, p' decays towards the trailing edge. Due to the position of the microphones, observations cannot be made for $\alpha = 0°$, however, the trends described for the other angles match past studies on airfoils [12, 32] and are qualitatively similar to those acquired for separated flows over other geometries [73–76].

The results show that, following the initial growth of p', the onset of rapid growth occurs near $\overline{x_{roll}}/c$. This suggests that, the growth detected by the microphones is related to the formation of vortices, which introduce large vertical velocity fluctuations [27]. The RMS surface pressure reaches its maximum when vortices are fully formed, and then decays as they break down to turbulence ahead of mean reattachment. This is corroborated by the high-speed flow visualizations (Figs. 4.14-4.15), which show that vortices appear fully formed in the region where p' saturates and then proceed to break down as they convect downstream. This process and the trends in the RMS surface pressure agree with the observations of Hudy et al. [74] on shear layer vortices forming behind an axisymmetric, backward-facing step. One important difference between these geometries, is that for backward-facing steps, the maximum of p'/q_∞ occurs at mean reattachment, whereas in this study, it lies ahead of x_R. This discrepancy is attributed to differences in vertical distance between the separated shear layer and the wall, which ahead of reattachment is larger in separation bubbles past backwards-facing steps than over airfoils. The larger distance in backwards-facing steps causes vortices to impinge onto the wall at a larger angle, which leads to larger pressure fluctuations at reattachment [74].

Past studies have focused on the link between velocity and pressure measurements without specific knowledge of the flow physics [12, 32]. The presence of the vortices in separation bubbles introduces another level of complexity in interpreting such measurements. Figure 4.25a shows that, following $\overline{x_{roll}}/c$, the growth rate of the RMS velocity decreases ahead of transition. This is opposite to the RMS pressure, which shows a significant increase in the streamwise growth rate at approximately $\overline{x_{roll}}/c$. Following their respective peaks, both types of measurements show a gradual decay; however, the relative rate of this decay appears to be much larger for the RMS pressure. One reason for this is due to the proximity of the surface pressure measurements compared to the velocity measurements, which are acquired within the separated shear layer [32]. Shear layer roll-up causes vortices to be shed and descend onto the wall, which reduces the distance between disturbances in the shear layer and the microphones near the surface and introduces strong vertical velocity fluctuations. The decay that follows the peak of p' is due to the decay of these vortices post transition, which results in a decrease in near wall fluctuations as the energy content

spreads vertically. These results suggest that the RMS surface pressure may effectively be used to detect regions of vortex formation in separation bubbles.

So far the results have presented measurements related to mean and fluctuating characteristics of the flow field as measured from hot-wires and microphones. Energy spectra of these measurements may be computed to study the spectral distribution of the energy content contained within the flow [32]. Figures 4.26-4.28 present energy spectra computed from the fluctuating velocity acquired by Probe 1 at $y = \delta^*$, and the fluctuating surface pressure. Each spectrum has been normalized by the total energy content and scaled by a factor proportional to $10^{x/c}$ for clarity.

The velocity spectra (Figs. 4.26a, 4.27a, 4.28a) show that, downstream of separation, spectra are approximately flat. Further downstream, disturbances contained within an unstable frequency band begin to grow at $x/c \approx 0.66$, 0.26, and 0.2 at $\alpha = 0$, 5, and 8°, respectively. The energy content within this unstable frequency band grows until the spectra broadens rapidly indicating the onset of laminar-to-turbulent transition. These figures are typical of velocity spectra obtained over airfoils at low Reynolds numbers [7, 10, 36]. The fluctuating surface pressure spectra (Figs. 4.26b, 4.27b, 4.28b) are similar to the velocity spectra and show that, prior to separation, the energy content is flat with no significant fluctuations related to a particular frequency or frequency band within the laminar boundary layer. Like the velocity spectra, following separation, disturbances are also amplified across a band of unstable disturbances until the energy content broadens. The pressure spectra, however, do not exhibit strong harmonics of the unstable frequency band ahead of the broadening of the spectra. These spectra are typical of fluctuating surface pressure measurements acquired over airfoils [32, 72].

To investigate how the frequency band of unstable disturbances evolves under different experimental conditions, it is beneficial to assign a frequency that describes disturbance growth at each α. While it is simple to take the largest peak within the unstable band, it is possible that this peak is not directly related to the disturbance growth. For example, the strongest peaks visible within the frequency band of unstable disturbances in Figure 4.27 are harmonics of $f \approx 188$ Hz. A similar peak, also near $f \approx 190$ Hz is visible for $\alpha = 0°$ in Fig. 4.26. As will be shown later, at $\alpha = 0$ and 5°, these peaks may be related to some sort of forcing. Thus, to prevent biasing towards such peaks, previous studies have described unstable frequency bands by estimating their central frequencies, f_0 [12, 32, 36]. While several techniques have been used to estimate f_0, in this study, f_0 was obtained by estimating the extent of the unstable band of disturbances (i.e. bandwidth), and selecting f_0 at the center. From the velocity spectra, the bandwidth of disturbances was estimated from the spectrum upstream of the appearance of harmonics, which marks the onset of nonlinearities. Estimates from the fluctuating surface spectra were computed from the spectrum nearest the x/c location of the velocity spectra estimate. Each velocity and

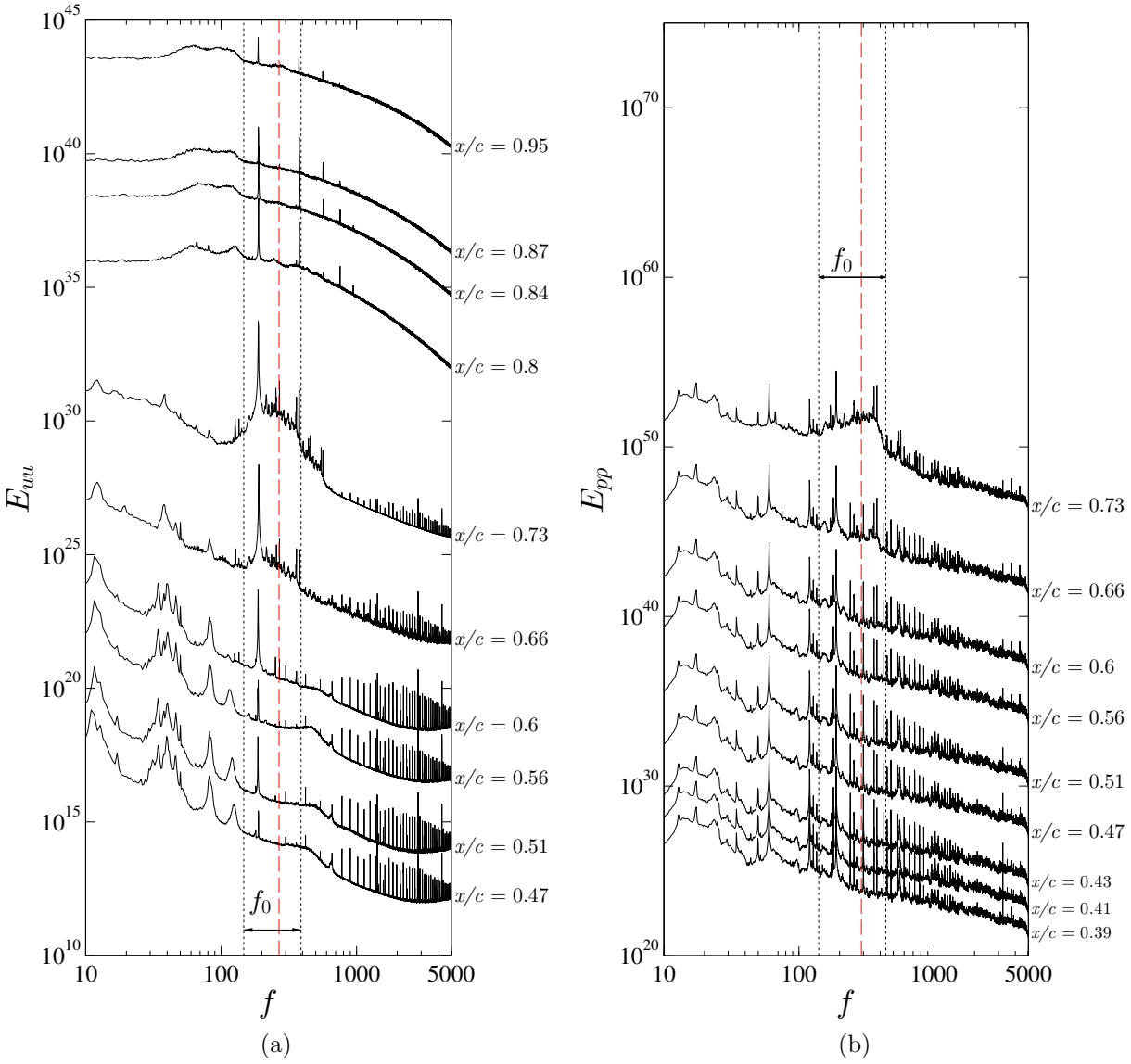


Figure 4.26: (a) Fluctuating velocity spectra computed from velocity signals acquired by Probe 1 in the rake and (b) fluctuating surface pressure spectra for $\alpha = 0°$. Each spectrum has been normalized by the total energy content and scaled by a factor proportional to $10^{x/c}$. The range of the unstable disturbance frequency band is denoted by the dotted lines (·····) separated by an arrow and f_0 is marked by the dashed line (– – –).

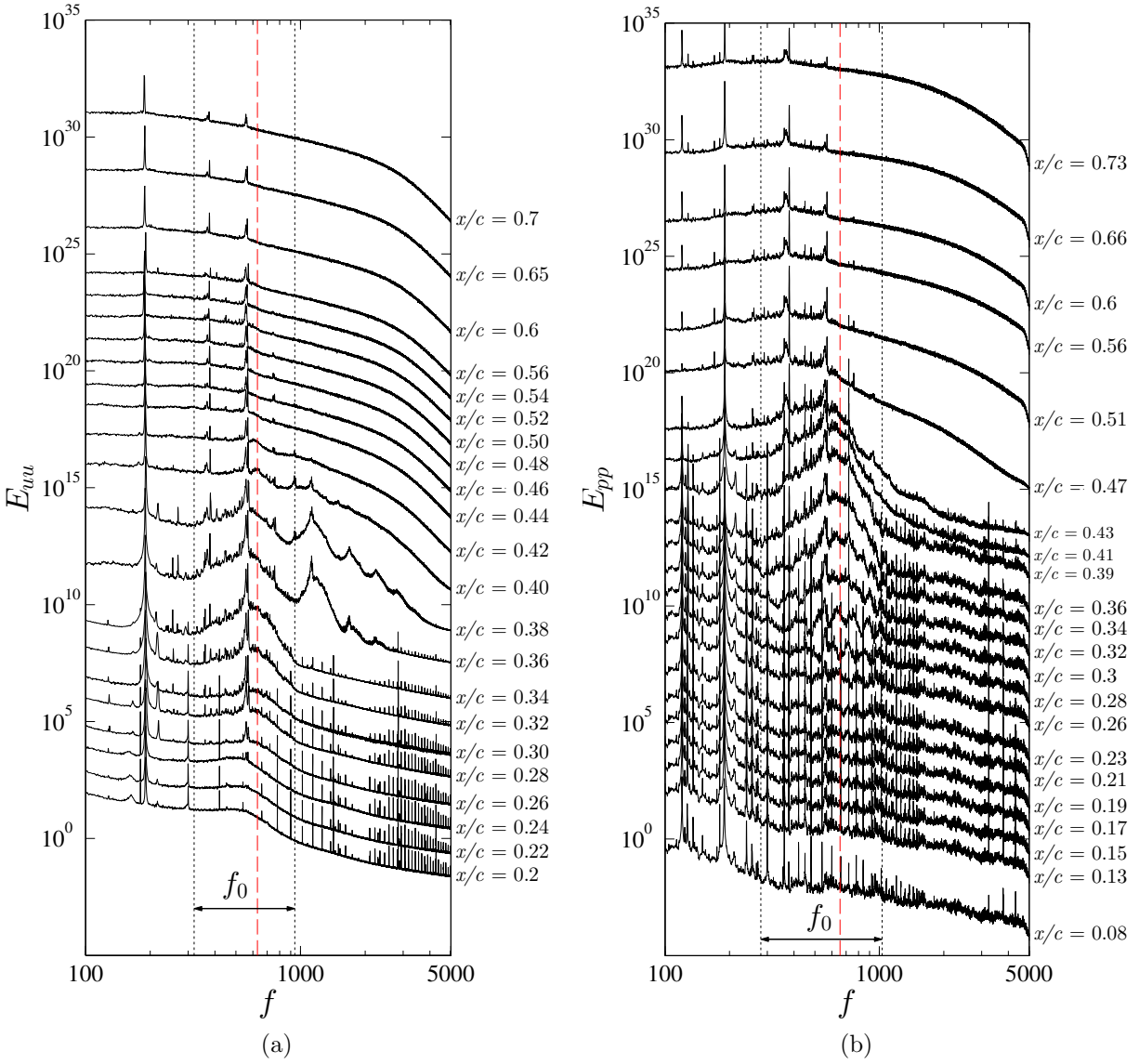


Figure 4.27: (a) Fluctuating velocity spectra computed from velocity signals acquired by Probe 1 in the rake and (b) fluctuating surface pressure spectra for $\alpha = 5°$. Each spectrum has been normalized by the total energy content and scaled by a factor proportional to $10^{x/c}$. The range of the unstable disturbance frequency band is denoted by the dotted lines (·····) separated by an arrow and f_0 is marked by the dashed line (– – –).

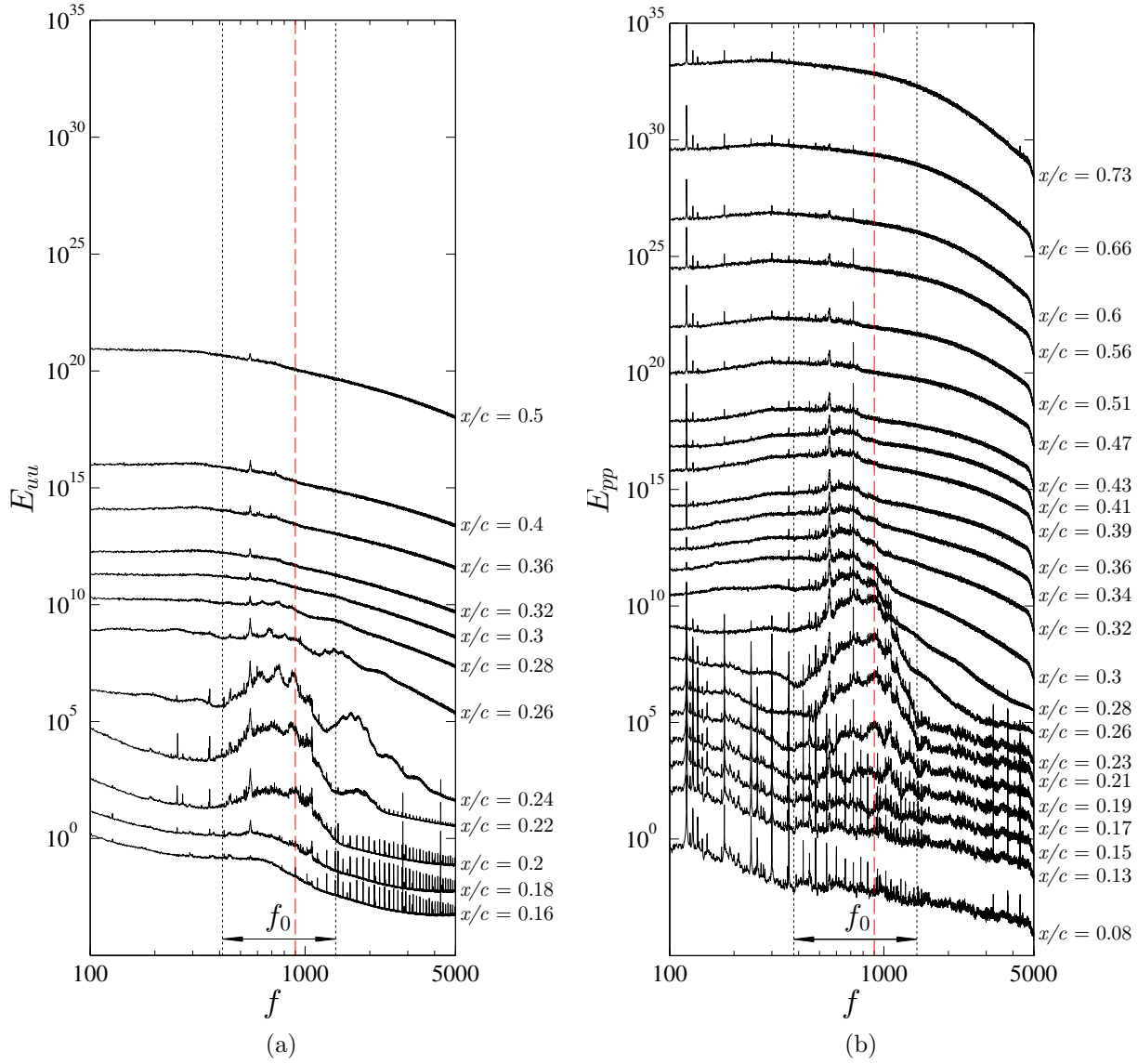


Figure 4.28: (a) Fluctuating velocity spectra computed from velocity signals acquired by Probe 1 in the rake and (b) fluctuating surface pressure spectra for $\alpha = 8°$. Each spectrum has been normalized by the total energy content and scaled by a factor proportional to $10^{x/c}$. The range of the unstable disturbance frequency band is denoted by the dotted lines (·····) separated by an arrow and f_0 is marked by the dashed line (– – –).

surface pressure spectra show dotted lines joined by an arrow, which shows the estimated disturbance freqeuncy band, with f_0 marked by the dashed line at the center. The resulting central frequencies, f_0, and bandwidths obtained using this methodology from both velocity and surface pressure spectra are presented in Table 4.3. The uncertainty in determining f_0 using this method is based on the uncertainty in determining the range of the frequency band and was estimated to be within $\pm$ 60 Hz (Section A.6). The results show that estimating f_0 from the velocity and surface pressure spectra produce different results, however, these differences are within the uncertainty of the measurements.

The growth of unstable disturbances leads to the laminar-to-turbulent transition of the separated shear layer by initiating the formation of shear layer vortices. As shown in the flow visualizations, these structures break down to turbulence over a region, which is not necessarily fixed. As a result, it is difficult to assign transition a fixed location. Instead, the results suggest that it may be best to define a location where transition is complete regardless of where the vortices are shed. The spectra show that, following the growth of unstable disturbances, the energy content broadens indicating a turbulent flow. However, as the spectra presented are averaged representations of the energy content distribution, they may include contributions from both laminar and turbulent flow in the region of vortex formation and breakdown. This is exemplified in Fig. 4.28a at $0.26 \leq x/c \leq 0.28$, which shows spectra that have broadened but still have wide peaks between 500 Hz $< f <$ 1200 Hz likely related to vortex shedding. Further downstream past $x/c \geq 0.3$, the spectra are broad and do not contain these peaks indicating that transition is complete. The spectra at $\alpha = 0$ and 5°, show similar spectra at $x/c = 0.44$, and 0.3, respectively. From the fluctuating surface pressure spectra, similar broadband spectra are visible for $x/c > 0.43$ at $\alpha = 5$. This location corresponds to mean transition obtained from the surface pressure distribution and falls within the uncertainty (Table 4.2). At $\alpha = 8°$, the surface pressure spectra shows

Table 4.3: Estimated central frequency and bandwidth of unstable disturbance band.

	$\alpha = 0°$	$\alpha = 5°$	$\alpha = 8°$
Estimates from E_{uu}:			
f_0 [Hz]	270	630	900
Bandwidth [Hz]	245	620	975
Estimates from E_{pp}:			
f_0 [Hz]	290	655	902
Bandwidth [Hz]	300	750	1045

that slight energy content between 600 Hz $< f <$ 1000 Hz persists between $0.3 \leq x/c \leq 0.6$. This makes it difficult to establish the location of where transition is complete. Also, as this energy content is present within the spectra well past mean reattachment, it suggests that the separation bubble has an influence on the development of the turbulent boundary that persists fairly downstream.

Figures 4.27a-4.28a show that, at $\alpha = 5$ and 8°, harmonics of the unstable frequency band are generated within the velocity spectra before they broaden between $0.36 \leq x/c \leq 0.38$ and $0.22 \leq x/c \leq 0.24$, respectively. These harmonics begin in the linear portion of the RMS velocity growth (Fig. 4.25a), and end ahead the onset of nonlinearities, which suggests that the harmonics are not directly related to vortices. The locations of the harmonics correspond to the regions of initial streamwise growth of the RMS surface pressure (Fig. 4.25b) ahead of $\overline{x_{roll}}/c$. It is expected that, as the amplitude of disturbances grows within the separated shear layer, significant vertical fluctuations will begin to appear ahead of shear layer roll-up. This assumption is confirmed by the flow visualizations (Figs. 4.14-4.15), which show that the smoke has a vertical motion in the same region as the harmonics. This motion is discussed in more detail in Section 4.2.4 but these results suggests that harmonics are caused by vertical velocity fluctuations introduced by vertical oscillations (i.e. flapping) of the separated shear layer ahead of roll-up, supporting the hypothesis of Boutilier and Yarusevych [12]. These vertical fluctuations lead to harmonics in the velocity spectra by causing hot-wires to measure superimposed, periodic out-of-phase signals at similar frequencies generated from streamwise and vertical components of the velocity [12].

At $\alpha = 5°$, the energy spectra (Fig. 4.27) display a low-frequency peak of energy content centred on $f \approx 188$ Hz, which is persistent in both the velocity and fluctuating surface pressure spectra at each x/c location. The peak is notable as it lies well outside the unstable disturbance band. The spectra also contain harmonics of this frequency, which begin to appear at $x/c = 0.24$ near mean separation. At $\alpha = 0°$, a peak near $f \approx 190$ Hz is also visible within the unstable disturbance band but, at $\alpha = 8°$, no peaks are observed at this frequency. Similar spectra with a low-frequency peak that lies outside the unstable disturbance band have been observed in past studies of airfoils at low Reynolds numbers and have been linked to the flapping of the separated shear layer at a frequency associated to free-stream disturbances [10, 20]. Specifically, Hain et al. [20] associated this flapping to a low-frequency variation of the most amplified disturbance in the unstable frequency band. However, in the present study, the generation of harmonics of a larger low-frequency peak resembles the spectra of a separation bubble undergoing high-amplitude excitation [10]. This suggests that the flow is undergoing some type of forcing, near $f \approx 188$ Hz. The presence of a peak near the same frequency as $\alpha = 0°$ suggests the same; however, it is unclear why it does not appear at $\alpha = 8°$. Tests performed in the empty test section at the same velocity as the free-stream in this investigation showed that there are no significant

disturbances present at $f = 188$ Hz (see Appendix B.3). Also, further testing indicates that the peaks are unrelated to generator noise and tonal noise off the airfoil model. As a result, the origins of these peaks are unknown and require further investigation.

The velocity and surface pressure spectra describe the distribution of energy content during the earlier stage of transition. By comparing the results of the flow visualizations to the results obtained from the spectra, links can be made on the relationship between the initial disturbance growth and vortex shedding (Fig. 4.18). Figure 4.29 compares the central frequency of the unstable disturbance frequency band, f_0, obtained from velocity and surface pressure measurements, and the vortex shedding frequency, $f_{shedding}$. The figure shows that f_0 increases with α nearly linearly, and that $f_{shedding}$ falls within the range of uncertainty of f_0 with the exception of the value computed from the surface pressure spectra at $\alpha = 0°$. The increasing trend of f_0 agrees with the results for the separation bubble regime of past studies on airfoils [7, 14]. The results show that vortex shedding occurs at a rate that lies within the frequency band of unstable disturbances and generally lies close to centre of the band, f_0. Like f_0, the relationship between $f_{shedding}$ and α is nearly linear, which is demonstrated by a least squares linear fit on the plot. With the

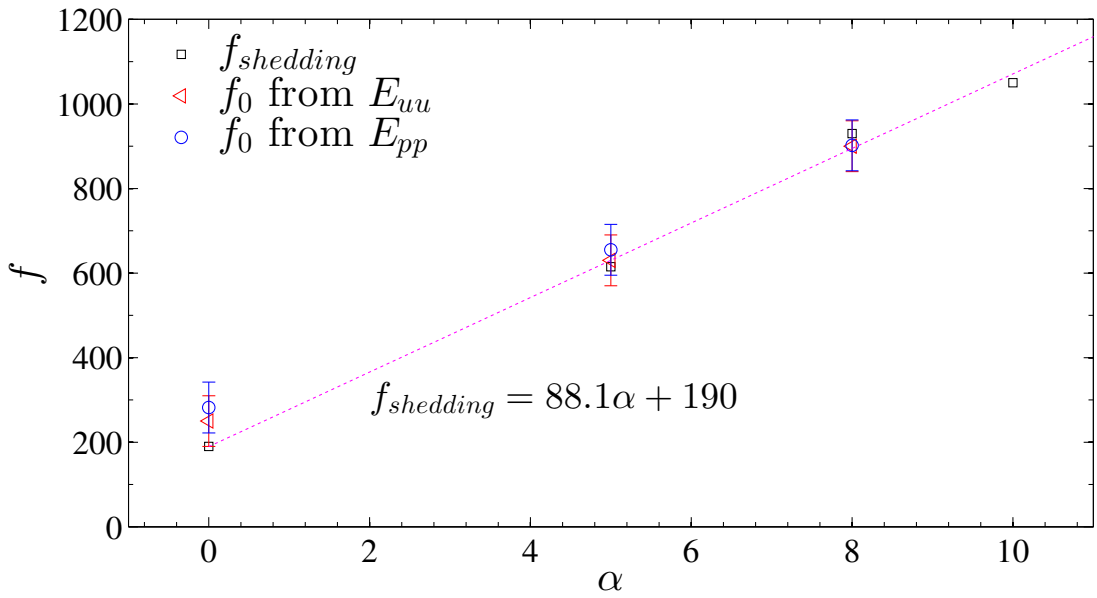
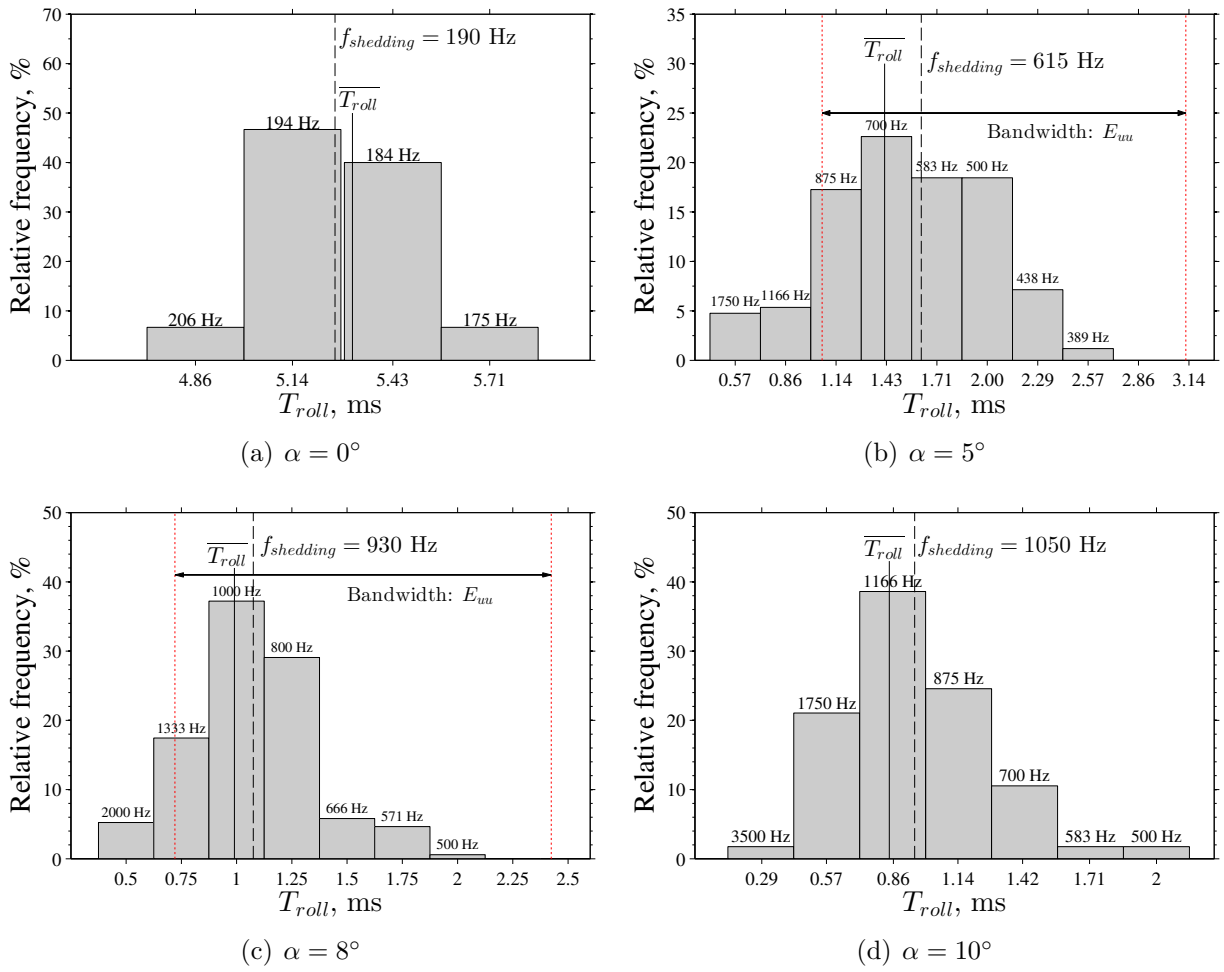


Figure 4.29: Comparison between the vortex shedding frequency, $f_{shedding}$, and central frequency of the unstable disturbance band, f_0 with a linear least-squares line of best fit (------) computed using $f_{shedding}$ and α.

exception of $\alpha = 0°$, the estimated vortex shedding frequencies are within 7% of the central instability frequencies, which is reasonable considering the error involved in obtaining f_0. At $\alpha = 0$, the difference between the central frequency and the vortex shedding frequency is more significant. As $f_{shedding}$ matches the low frequency peak that lies within the unstable disturbance band near α = 190 Hz, the vortex shedding frequency may be related to unidentified forcing discussed earlier. These results may also be used to explain the larger values of $St_{shedding}$ obtained in the present study in comparison to the results of Burgmann and Schröder [14] at lower chord Reynolds numbers, see Fig. 4.18. Since vortices are being shed near the central frequency of the unstable disturbance band within the separated shear layer, higher shedding frequencies are expected at larger Reynolds numbers as the central frequency has been shown to scale proportionally to chord Reynolds numbers at fixed angles of attack [12].

The results have shown that the vortex shedding frequency lies within the frequency band of unstable disturbances. This agrees with the results of previous studies on airfoils [14, 15, 20] and flat plates [22, 49], which have shown that vortex shedding within separation bubbles is associated to disturbance growth contained within this frequency band. As the vortex shedding frequency, $f_{shedding}$, presented in Figure 4.29 is a mean quantity, it is of interest to investigate how the vortex shedding varies in time. To study this, the elapsed time (i.e. number of frames) between each consecutive roll-up was obtained from image sequences at each angle of attack. Figure 4.30 presents relative frequency histograms of the time period obtained between consecutive instances of roll-up, T_{roll}, as generated from the results of this analysis. The mean of the roll-up period, $\overline{T_{roll}}$, and frequencies associated to each period are marked above each bar in the plots. Also, the period associated to $f_{shedding}$ is marked by a dashed line, and for $\alpha = 5$ and 8°, periods corresponding to the range of the unstable frequency band obtained from the velocity spectra are marked by dotted lines separated by an arrow. The plots show that $\overline{T_{roll}}$ lies near $f_{shedding}$ and, unlike $f_{shedding}$, these plots give an estimate over which band of frequencies shedding occurs. The standard deviations of T_{roll} are 8.4, 306, 316, and 477 Hz at α =0, 5, 8, and 10°, respectively. This shows that the bandwidth over which shedding occurs increases with α. At $\alpha = 0°$, the standard deviation is significantly lower with all roll-up periods observed lying between roll-up intervals associated to 175 Hz $< f <$ 206 Hz, a range of frequencies that falls within the unstable frequency band (not shown). This suggests that shedding occurs more steadily at this angle of attack. At larger angles of attack, the stanadard deviation is much greater, which shows that vortex shedding does not occur at a steady frequency. However, the results obtained at α =5 and 8° show that 90% of the observed roll-up periods fall within their respective unstable frequency bands. Along with the results at $\alpha = 0°$, this shows that, while vortex shedding may be unsteady at the larger angles of attack, it occurs predominantly within the unstable frequency band (Table 4.3).



(a) $\alpha = 0°$

(b) $\alpha = 5°$

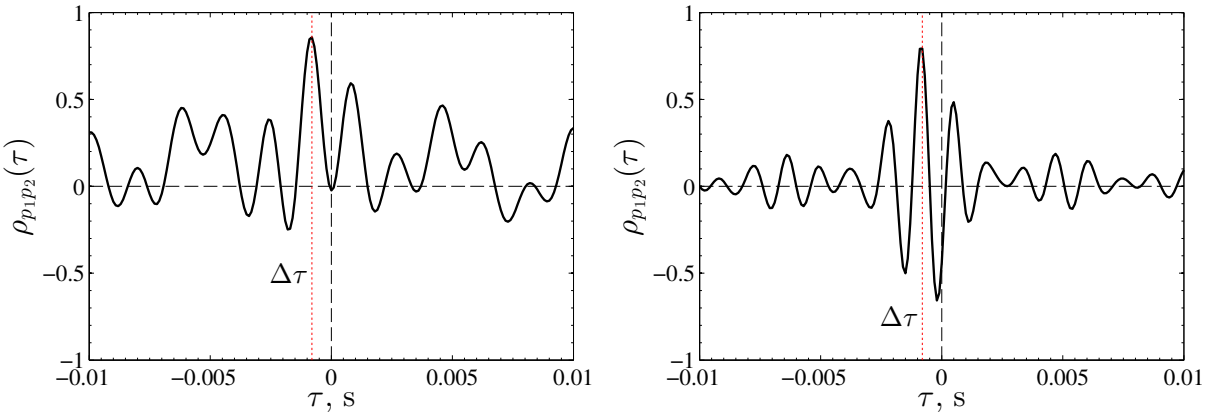
(c) $\alpha = 8°$

(d) $\alpha = 10°$

Figure 4.30: Histograms showing the relative frequency distribution of the period between consecutive instances of shear layer roll-up obtained from high-speed flow visualization video analysis. Frequencies associated to T_{roll} are marked above the histogram bars. The mean roll-up period is marked by $\overline{T_{roll}}$ and the period associated to $f_{shedding}$ is marked by the dotted line (·····). Periods associated to the frequency range of unstable frequencies (Bandwidth: E_{uu}) are marked by the dotted lines (·····) and are separated by arrows.

The results presented in this section show that the streamwise development of disturbances is linked with the roll-up of the separated shear layer. Disturbances are amplified as they propagate within the separated shear layer and lead to the formation of shear layer vortices. To further study the link between disturbances and vortices, the convection speed of disturbances may be estimated from simultaneously acquired surface pressure signals obtained across the suction side of the airfoil. Following the technique of Gerakopulos and Yarusevych [32], a cross-correlation analysis of simultaneously sampled microphone signals was performed to estimate the convection velocity of pressure disturbances at angles of attack of $\alpha = 5$ and 8°.

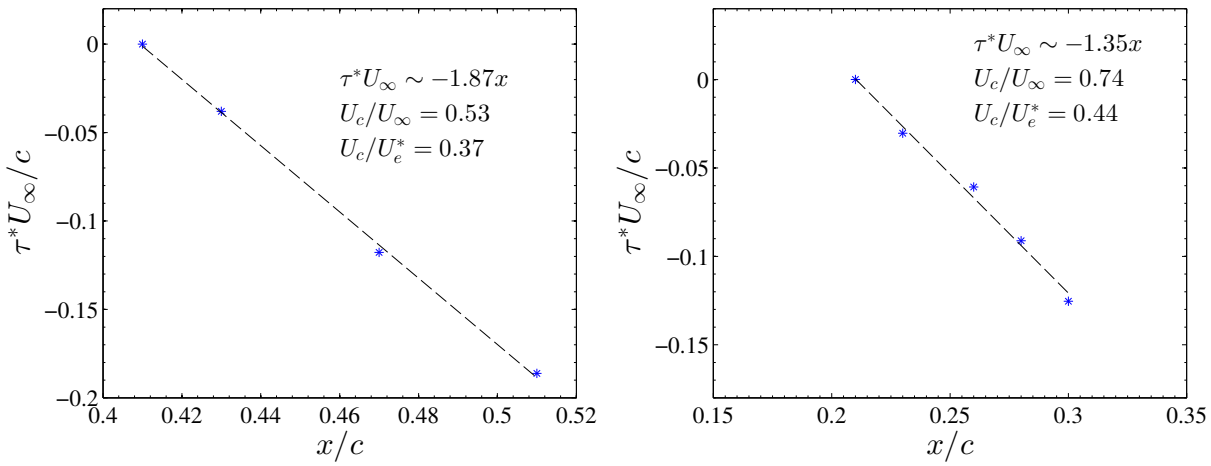
Figure 4.31 presents cross-correlation coefficient functions computed from signals acquired by adjacent microphones in the pronounced growth region of the RMS fluctuating surface pressure. The functions were computed with signals acquired by microphones located at x/c =0.39 and 0.41 and at x/c =0.26 and 0.28 for $\alpha = 5$ and 8°, respectively. The functions were computed from the average of cross-correlation coefficient functions obtained from 256 non-overlapping windows of 2^{14} samples. The lag of the maximum value of each function may be used to estimate the time lag, $\Delta\tau$, between the fluctuating pressure signals with negative values indicating that the disturbances propagate downstream.



(a) $\alpha = 5°$ (b) $\alpha = 8°$

Figure 4.31: Cross-correlation coefficient functions computed from simultaneously acquired surface pressure signals. At $\alpha = 5$ and 8°, the cross-correlated signals were acquired with microphones located at x/c =0.39 and 0.41 and at x/c =0.26 and 0.28, respectively. $\Delta\tau$, which is computed between the maximum coefficient and zero time lag, is marked by the dotted line (·····).

Figure 4.32 presents the accumulated time lag, τ^*, obtained by summing up the time lags of cross-correlation coefficient functions obtained by adjacent microphones. The accumulated time lag represents the time required for disturbances to propagate over the distance between microphones in the RMS surface pressure growth region. This allows for the convection velocity of these disturbances to be computed. A least squares linear fit between the accumulated time lag and distance was computed, and the reciprocal of the slope was used to estimate the convection velocity of disturbances: $U_c = 1/(\Delta\tau^*/\Delta x)$. At $\alpha = 5$ and $8°$, the convection velocities were estimated as $0.53\,U_\infty$ and $0.75\,U_\infty$, respectively, and are near the estimates obtained for the drift velocity of shear-layer vortices from the high-speed flow visualizations (Fig. 4.19). The vortex drift speed obtained at $\alpha = 5°$ is approximately 20 % larger than U_c, while the values obtained for $\alpha = 8°$ are much closer. It is proposed that the merging of roll-up vortices at $\alpha = 5°$ may cause this discrepancy between U_c and U_{drift}. A parametric study by Boutilier and Yarusevych [7] for flow over the same model shows a general increase in the convection velocity of pressure disturbances with α. However, from $\alpha = 4$ to $6°$, there is a valley with nearly constant convection velocities of approximately $0.5\,U_\infty$. The study also showed that similar valleys occur at larger Reynolds number. As these valleys cause a deviation in the trend between U_c and



(a) $\alpha = 5°$ (b) $\alpha = 8°$

Figure 4.32: Normalized accumulated time lag computed from cross-correlations of surface pressure signals. The linear least-squares line of best fit between the normalized time lag and streamwise coordinate is represented by the dashed line (−−−) along with the slope and convection velocity, U_c, normalized by U_∞ and U_e^*.

α, it is hypothesized that these valleys may be indicative of angles of attack were vortex merging occurs.

4.2.3 Vortex Merging

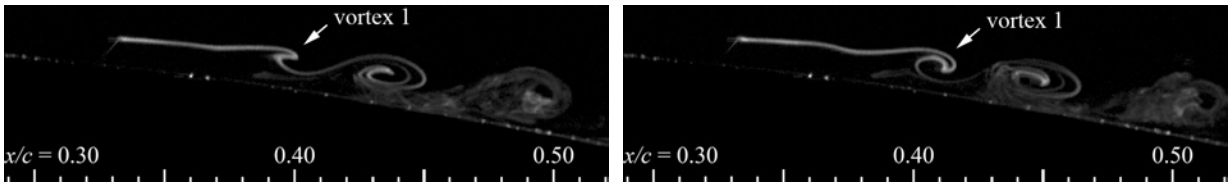
An analysis of side view separation bubble visualizations revealed that merging of separated shear layer roll-up vortices occurs over the suction side of the airfoil at $\alpha = 5$ and 8°. The process is analyzed here for the case of $\alpha = 5°$. Figures 4.33, and 4.34 display representative flow visualization sequences of the merging that occurs between two and three vortices at $\alpha = 5°$, respectively, while Figure 4.35 shows a roll-up vortex that does not merge.

Figures 4.33a-4.33e show that, initially, a first vortex (vortex 1) is shed between $0.4 \lesssim x/c \lesssim 0.45$ and is followed by a second vortex (vortex 2) that emerges between $1.5\,\text{ms} \leq \Delta t \leq 2.5\,\text{ms}$ at $0.39 \lesssim x/c \lesssim 0.43$. The two vortices proceed to merge and form a single vortex (vortex 1 + 2) between $2.5\,\text{ms} \leq \Delta t \leq 4\,\text{ms}$. The merging is followed by the breakdown of the newly formed vortex (vortex 1 + 2), in a process that appears to be initiated at the wall. When the new vortex reaches $x/c \approx 0.5$ (Fig. 4.33l), the increased mixing of the smoke indicates that the breakdown to turbulence has occurred. The merging between vortex 1 and vortex 2 is followed by a third roll-up vortex (vortex 3) that breaks down without merging.

Figure 4.34 shows that, between $0\,\text{ms} \leq \Delta t \leq 3\,\text{ms}$, two roll-up vortices (vortices 1 + 2) are in the process of merging between $0.43 \lesssim x/c \lesssim 0.48$ when a third vortex (vortex 3) is shed (Fig. 4.34g). In Figures 4.34h-4.34j, vortex 3 proceeds to merge with the combined vortices (vortices 1 + 2) between $0.44 \lesssim x/c \lesssim 0.50$ and the new vortex convects downstream. The merging of the first two vortices is similar to what is depicted in Figure 4.33. The newly merged vortex convects downstream and by $x/c \approx 0.50$, the increased mixing of the smoke indicates that the structure has broken down to turbulence.

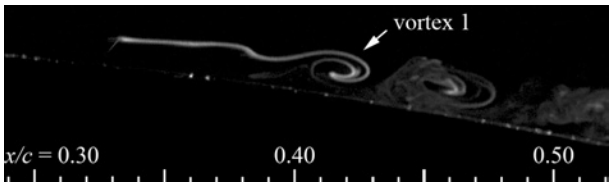
In contrast to the visualizations presented in Figures 4.33 and 4.34, Figure 4.35 shows a roll-up vortex marked by an arrow being shed, convecting downstream, and breaking down without any merging.

These visualizations demonstrate that, at $\alpha = 5°$, roll-up vortices are involved in different types of interactions. To investigate this, a statistical analysis of flow visualizations at $\alpha = 5°$ was performed to investigate vortex merging by identifying when and where vortices form, and by then tracing their development and interactions with other roll-up structures. Data regarding the formation of vortices was obtained using the technique described in Section 4.2 (Figure 4.17a). To study the interactions of vortices following formation, categories of events were created to collect statistics based on the development of individual vortices. These events are categorized as when an individual vortex, (i) does not merge (no merging), (ii) merges with another vortex (double merger), and (iii) merges

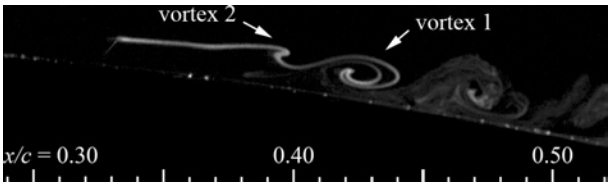


(a) $\Delta t = 0$ ms

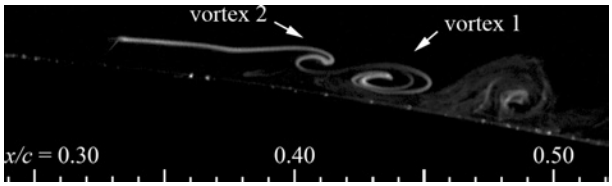
(b) $\Delta t = 0.5$ ms



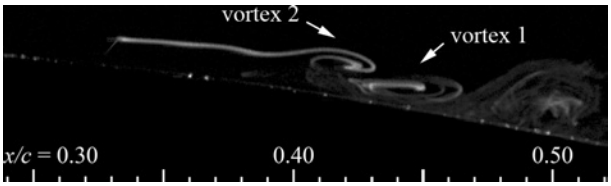
(c) $\Delta t = 1$ ms



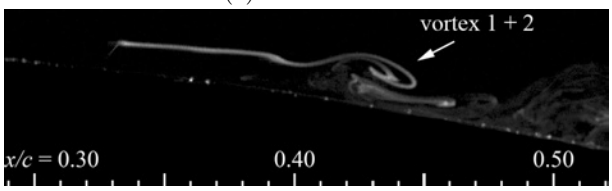
(d) $\Delta t = 1.5$ ms



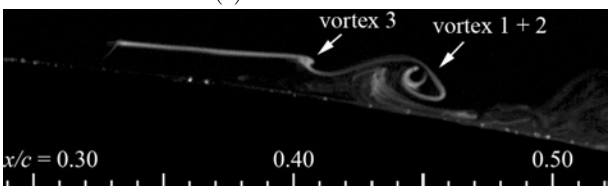
(e) $\Delta t = 2$ ms



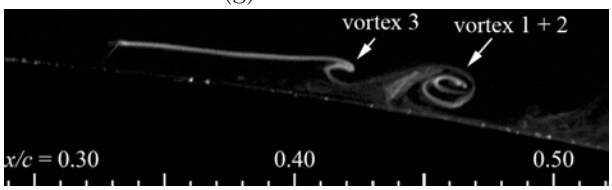
(f) $\Delta t = 2.5$ ms



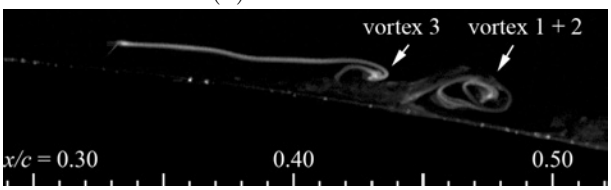
(g) $\Delta t = 3$ ms



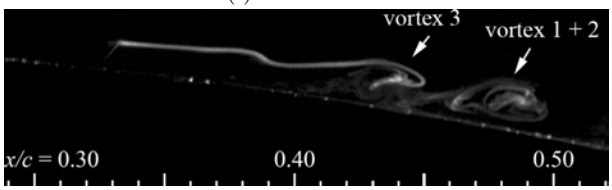
(h) $\Delta t = 3.5$ ms



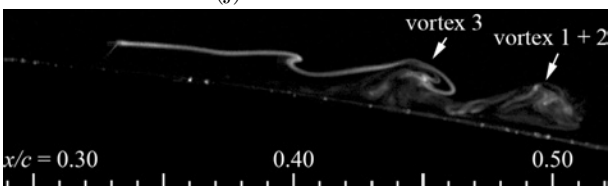
(i) $\Delta t = 4$ ms



(j) $\Delta t = 4.5$ ms

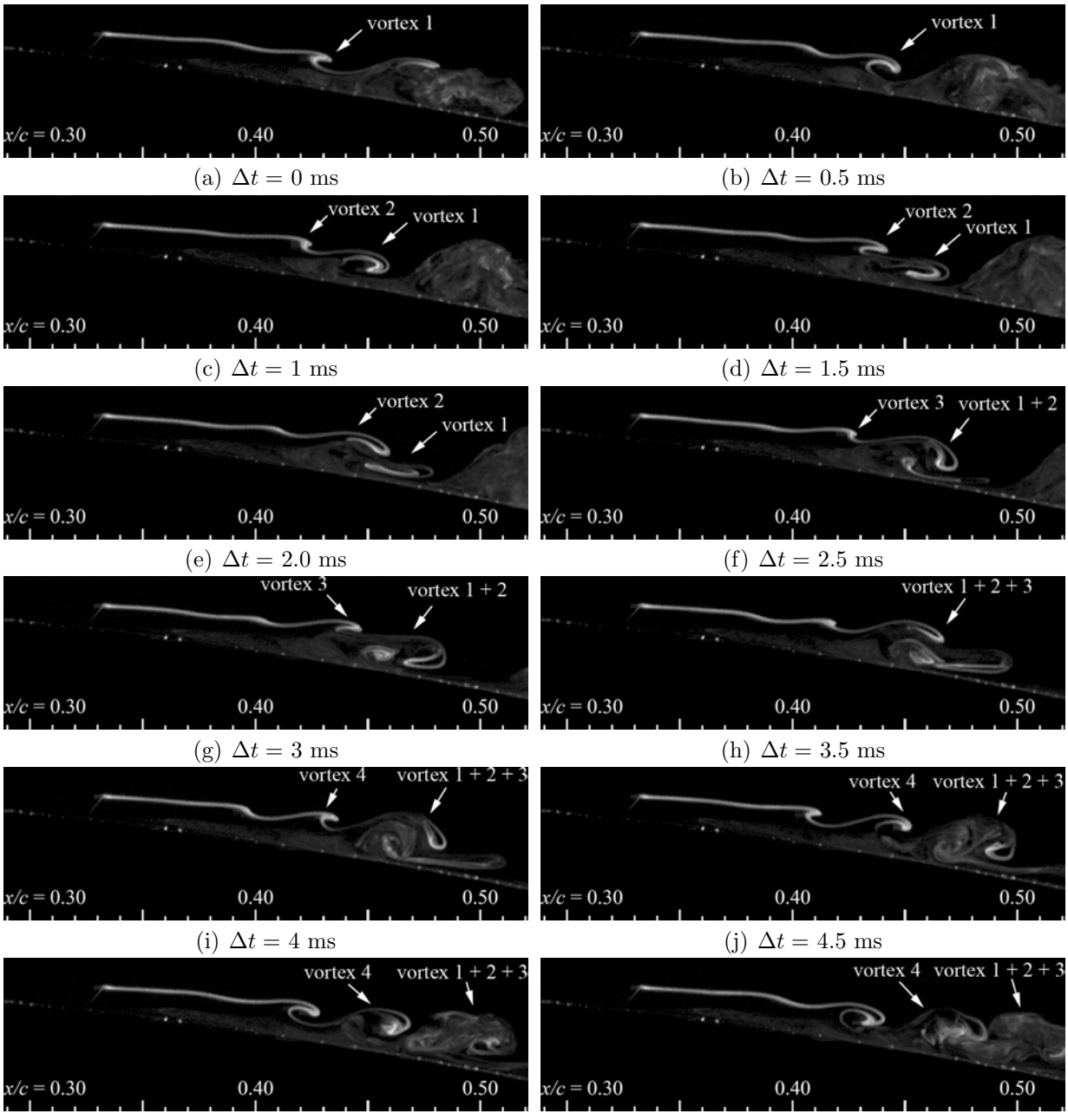


(k) $\Delta t = 5$ ms



(l) $\Delta t = 5.5$ ms

Figure 4.33: Sequence of high-speed flow visualizations at $\alpha = 5^\circ$ showing the merging of two roll-up vortices.



(a) $\Delta t = 0$ ms (b) $\Delta t = 0.5$ ms

(c) $\Delta t = 1$ ms (d) $\Delta t = 1.5$ ms

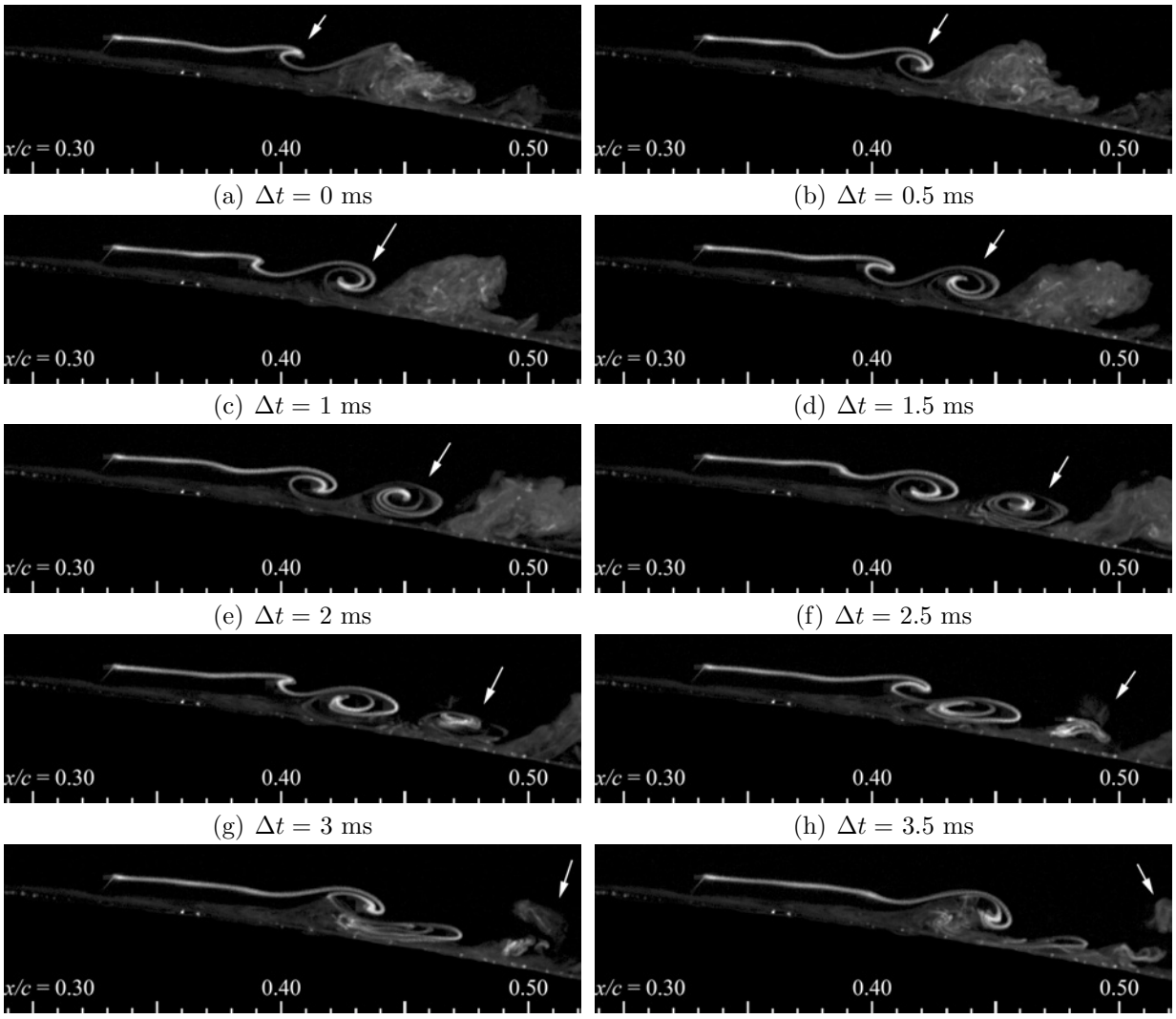
(e) $\Delta t = 2.0$ ms (f) $\Delta t = 2.5$ ms

(g) $\Delta t = 3$ ms (h) $\Delta t = 3.5$ ms

(i) $\Delta t = 4$ ms (j) $\Delta t = 4.5$ ms

(k) $\Delta t = 5$ ms (l) $\Delta t = 5.5$ ms

Figure 4.34: Sequence of high-speed flow visualizations at $\alpha = 5^\circ$ showing the merging of three roll-up vortices.



(a) $\Delta t = 0$ ms (b) $\Delta t = 0.5$ ms

(c) $\Delta t = 1$ ms (d) $\Delta t = 1.5$ ms

(e) $\Delta t = 2$ ms (f) $\Delta t = 2.5$ ms

(g) $\Delta t = 3$ ms (h) $\Delta t = 3.5$ ms

(i) $\Delta t = 4$ ms (j) $\Delta t = 4.5$ ms

Figure 4.35: Sequence of high-speed flow visualizations at $\alpha = 5°$ showing a vortex that does not merge after formation.

with two vortices (triple merger). Each shear layer vortex shed was tagged with a sole event. This means that, while the merging of three vortices may begin with two vortices merging, the event associated to each of the three vortices is a triple merger.

Table 4.4 presents the frequency and relative frequency of each event. The frequency refers to the number of times each event was recorded in the analysis, and the relative frequency was obtained by dividing frequency by the total number of vortices shed. The results show that 65% of vortices shed are involved in double or triple merging events, and that these merging events occur nearly evenly. This number is significantly larger than the number of vortices that merge at $\alpha = 8°$, which is estimated at 10%.

Following shear layer roll-up, interactions between vortices lead to merging. The level of these interactions depend on when and where the vortices form. Thus, to study how vortex merging is associated to the formation of vortices, events were linked to the time and location of each instance of roll-up. Figure 4.36 shows the streamwise location of roll-up, x_{roll}, plotted against time for each instance of roll-up. The plot contains markers, which correspond to the event associated to each instance of roll-up. The plot shows that the location of shear layer roll-up varies significantly in time, with consecutive roll-ups rarely occurring at the same location. In terms of how roll-up location influences events, the plot does not show a clear correlation between x_{roll} and any of the roll-up events. Indeed, the average roll-up location associated to each event occurs within $0.005c$ of $\overline{x_{roll}}$. However, 68% of roll-ups involved in triple merging occur ahead of $\overline{x_{roll}}$, while in the case of double merging roll-ups occur evenly on both sides of $\overline{x_{roll}}$. Also, 62% of vortices that do not merge are shed beyond $\overline{x_{roll}}$. This suggests that the location of shear layer roll-up does influence whether vortices merge or not, with vortices shed further downstream, less likely to be involved in merging.

Figure 4.36 also describes the pattern in which vortices merge. Figure 4.33 showed that, following the merger of two vortices, a single vortex was shed and did not merge. The results show that this is common and occurs after 75% of double mergers. The same is also true for triple mergers, as a single vortex is shed after 61% of mergers. This shows that most instances of merging does not occur consecutively.

Event	*(i) No merging*	*(ii) Double merger*	*(iii) Triple merger*
Frequency	60	56	54
Relative frequency, %	35.3	33.0	31.7

Table 4.4: Frequency and relative frequency of roll-up associated of vortex merging events associated to instances of shear layer roll-up for $\alpha = 5°$.

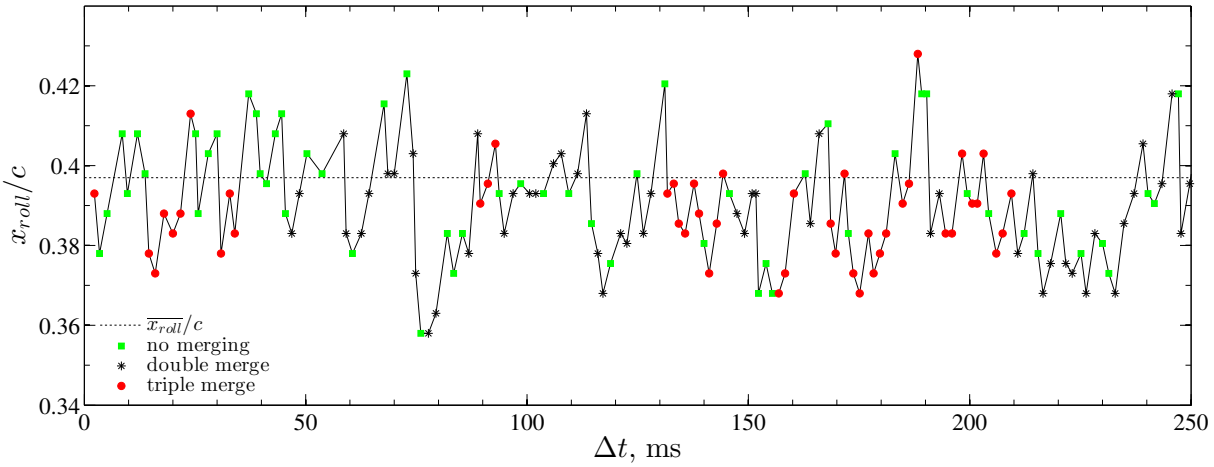


Figure 4.36: Estimated roll-up x/c locations plotted against time for $\alpha = 5°$. Events associated to each instance of roll-up are marked.

Figure 4.36 presents how vortex events evolve over time. The plot shows that different events become more dominant during certain periods of time. For example, the plot shows that, between 0 ms $\lesssim t \lesssim$50 ms, 57% of roll-up vortices do not merge, while 37% are involved in triple mergers. Then, between, 50 ms $\lesssim t \lesssim$ 130 ms, 58% of vortices merge as pairs, while 36% do not merge. Finally, between 130 ms $\lesssim t \lesssim$ 210 ms, 60% of events are triple mergers, while double mergers account for 15% of events. These results suggest that different events dominate over different periods of time. Since a period comprised mostly of single vortices is followed by periods of strong double merging and triple merging, this suggests that this process may also be cyclical.

The results show that, at $\alpha = 5°$, vortex merging is dominant but does not occur in an organized fashion. The vortex merging process appears to be similar to what occurs in plane mixing layers [55]. In their study of unforced and artificially forced plane mixing layers, Ho and Huang [55] observed different merging scenarios with up to four vortices merging. In contrast, until this investigation, only vortex merging involving two spanwise vortices has been observed within separation bubbles forming over airfoils [15, 36] and flat plates [25]. The merging processes of two and three vortices observed in this study are very similar to the observations of Ho and Huang [55], who also observed that vortex merging was affected by the phase shift between the forcing and the fundamental frequency. Furthermore, they showed that the merging of vortices became disorganized as the amplitude of forcing was

decreased with their images of disorganized vortex merging resembling the images from this study (Figs. 4.33-4.34).

While vortex merging will still occur in an unforced plane mixing layer [55], the effect of forcing on this flow reveals some interesting results that might relate to the behaviour observed at $\alpha = 5°$. Ho and Huang [55] forced the flow with subharmonics of the most amplified instability frequency of the mixing layer. The subharmonic forcing frequencies were designated modes, where for example, Mode IV refers to the fourth subharmonic of the most amplified frequency. The study showed that, for Mode I forcing, vortex merging is suppressed for a distance until it assumes the traits of an unforced plane mixing layer. For Modes II, III, and IV, vortex merging occurs between two, three, and four vortices, respectively. In the present study, the spectra presented in Section 4.2.2 suggest that some type of forcing near $f \approx 188$ Hz may be occurring over the airfoil at $\alpha = 5°$ with peaks within the spectra observable at the first two harmonics of this frequency at $f \approx 376$ and 564 Hz. From the velocity spectra (Fig. 4.27a), the central frequency of unstable disturbances at this α is $f_0 \approx 630$ Hz, and while the peak at $f \approx 564$ Hz does not match f_0, it is near the bounds of uncertainty; this makes $f \approx 188$ nearly a third subharmonic of f_0. If vortices are expected to shed at a rate near f_0, this implies that the triple vortex merging observed over the airfoil may be related to vortex merging observed in the plane mixing layer undergoing Mode III forcing. However, as double vortex merging also occurs, this implies that Mode II-type forcing may also exist. The results of this study show that vortex merging between two and three vortices occurs predominantly in sequences that may be part of a cycle involving a segment comprised mostly of vortices that do not merge. It is possible that if $f = 188$ Hz is slightly lower than the true subharmonic of f_0 and that this forcing is causing the vortex merging to cycle between different subharmonic modes like in plane mixing layers. As the vortex merging is disorganized and mostly discontinuous, which is similar to the results of Ho and Huang [55], this implies that this forcing is weak.

Forced flows with vortex merging typically show large amplitudes of subharmonic disturbances of the fundamental disturbance frequency, which dominate in the region of vortex merging [13, 55]. Ho and Huang [55] showed that, in plane mixing layers, subharmonic forcing results in the subharmonic growth of disturbances, which eventually surpasses the fundamental instability growth in the vortex merging region. To test whether Mode II and Mode III type forcing may be resulting in the large growth of subharmonic disturbances at $\alpha = 5°$, bandpass filters were applied to velocity and fluctuating surface pressure signals. Digital band-pass filters centred on 188, 376, and 564 Hz were designed with a ± 25 Hz passband. The central frequencies of the filters correspond to $f = 188$ Hz and the first two harmonics at $f \approx 376$ and 564 Hz.

Figure 4.37 presents the streamwise development of the RMS velocity of unaltered and band-pass filtered signals acquired by Probe 1 at $\alpha = 5°$. The central filter frequency and

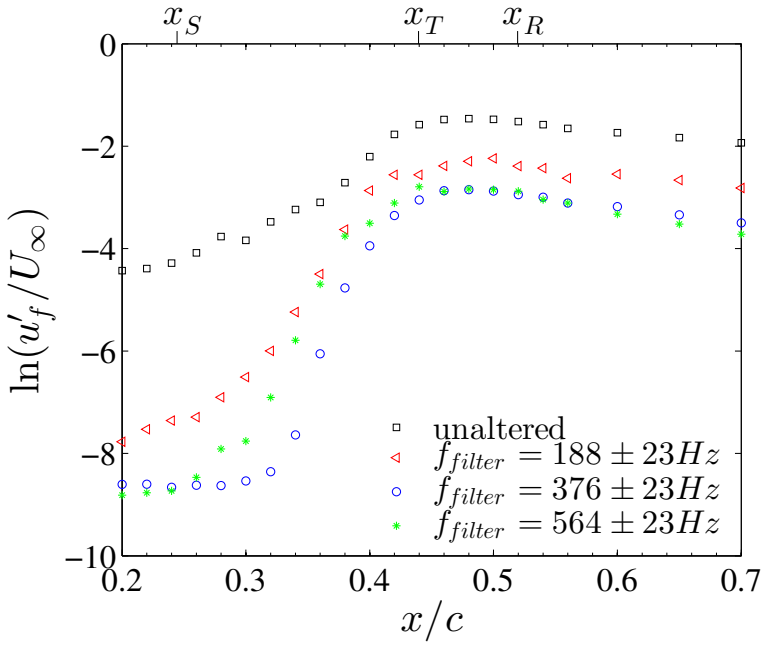


Figure 4.37: Streamwise development of RMS velocity computed from unaltered and bandpass filtered signals acquired by Probe 1 for $\alpha = 5°$. f_{filter} denotes the range of the passband used in band-pass filtering.

the range of the passband is denoted by f_{filter}. Figure 4.37a shows that the amplitude of the signals is amplified downstream until the mean transition and reattachment region, after which they decay towards the trailing edge. Prior to mean separation, the disturbance amplitude at $f = 188$ Hz is largest and remains so across the chord. The plot suggests that disturbances at this frequency are amplified ahead of separation. The amplitude of disturbances at $f = 564$ Hz, which lies within the unstable disturbance band, is nearly constant ahead of mean separation and increases from $x/c = 0.3$ until mean transition. The growth of disturbances at $f = 564$ Hz is followed by the amplification of disturbances at $f = 376$ Hz. Like the disturbances at $f = 564$ Hz, these disturbances also begin to grow at $x/c = 0.3$ but at $x/c = 0.32$, the streamwise rate of disturbance growth increases significantly. The disturbances grow until $x/c = 0.46$, where they are essentially equal in amplitude to those at $f = 564$ Hz, and by $x/c = 0.56$, they are larger. The results show that disturbances at $f = 376$ Hz reach amplitudes similar to disturbances near the center of the unstable disturbance band at $f = 564$ Hz and that disturbances at $f = 188$ Hz grow ahead of energy content at both these frequencies. While this may appear similar to what

occurs in forced plane mixing layers, subharmonic growth generally occurs following the fundamental growth [55], which is not the case here. Also, the peak of the amplitude of subharmonic disturbances is typically one order of magnitude greater than the fundamental disturbances [55]. As the results suggest that a double and triple vortex merging is due to a combination of Modes II and III type forcing, it would be expected that the amplitudes of these modes would be reduced.

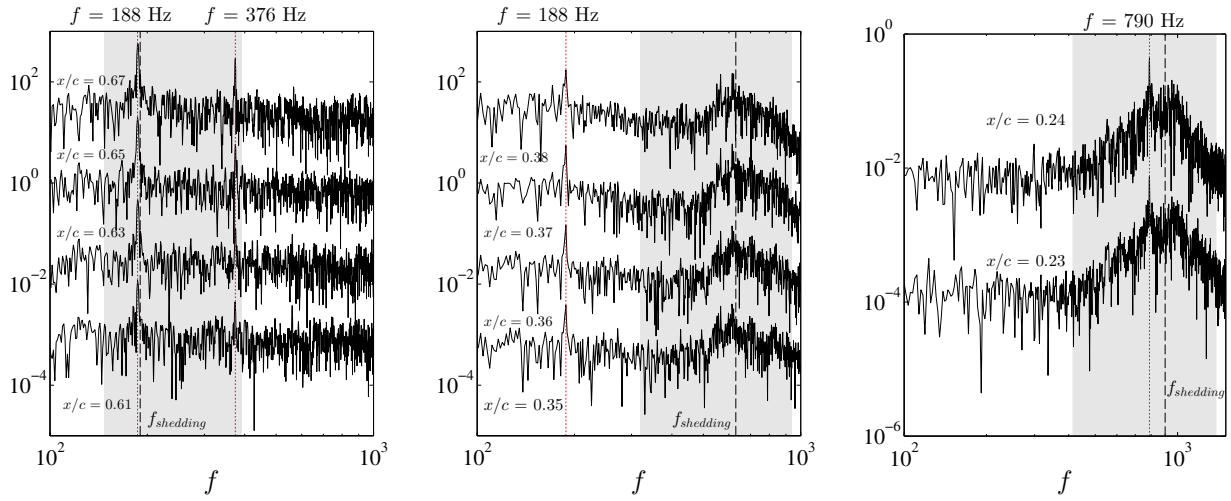
These the results show that there are similarities between vortex merging observed in this study at $\alpha = 5^\circ$ and in plane mixing layers undergoing subharmonic forcing. Also, while this discussion puts forward a hypothesis on the cause of the vortex merging, they also show that there are still several questions related to the nature of the forcing. To this end, further investigation is still required into the source of the low-frequency peaks at this angle of attack, and it is possible that a study exploring a similar type of modal forcing as [55] might reveal further aspects of vortex interactions over airfoils.

4.2.4 Shear Layer Flapping

The side view separation bubble visualization sequences show that smoke contained within the separated shear exhibits a flapping motion and that the magnitude of the flapping increases until roll-up occurs. To determine the relationship between the flapping, disturbance growth within the separated shear layer, and vortex shedding, a cross-correlation algorithm was employed using DaVis software to extract a vertical displacement signal of the smoke within the separated shear layer at streamwise locations ahead of roll-up at angles of attack of 0, 5, and 8°. Note that a signal was not obtained at $\alpha = 10^\circ$ due to the proximity of the smoke-wire to roll-up.

Figure 4.38 presents spectra computed by performing a Fast Fourier Transform (FFT) on each time-varying displacement signal. Each spectrum has been normalized by the energy content and scaled by a factor proportional to $10^{x/c}$. The vortex shedding frequency and the frequency band of unstable disturbance growth obtained from velocity spectra are marked on the plots by dashed lines and grey shaded areas, respectively. The large amount of noise contained within the spectra is attributed to the relatively small signal length available. Nevertheless, dominant peaks and frequency bands related to the motion of the smoke can be identified within the spectra.

The results show that the flapping motion of the smoke occurs at frequencies which lie within the frequency band of unstable shear layer disturbances. The spectra also show that peaks lie near the vortex shedding frequency. At $\alpha = 0$, the largest energy content is contained within a narrow frequency band centred at $f \approx 190$ Hz followed by a harmonic at $f \approx 380$ Hz. The narrow band suggests that the flapping at this angle of attack is associated primarily with this frequency, which is also the most amplified frequency within the spectra.



(a) $\alpha = 0°$ (b) $\alpha = 5°$ (c) $\alpha = 8°$

Figure 4.38: Spectra computed from vertical displacement signals of smoke within the separated shear layer upstream of roll-up. Each spectrum has been normalized by the total energy content, and the spectra have been scaled proportionally to $10^{x/c}$ for clarity. The vortex shedding frequency is marked by the dashed line (– – –) and the frequency band of disturbance growth is shaded in grey.

At $\alpha = 8$ (Fig. 4.38c), the spectra only show significant energy content contained within the unstable frequency band at frequencies between 450 Hz $< f <$ 1100 Hz, which suggests that there is no low frequency component of flapping. At $\alpha = 5°$, energy content is present between 500 Hz $< f <$ 900 Hz, which lies within the disturbance growth frequency band. At this angle of attack, a low-frequency peak lies at $f \approx 188$ Hz, which matches the frequency of the peak that lies below frequency band of unstable disturbances in velocity and surface pressure spectra. This demonstrates that, at this α, the separated shear layer has a component of flapping corresponding to a longer wavelength. Similar behaviour has been observed by Hain et al. [20] and Dovgal et al. [10] in separation bubbles forming over airfoils, and has been linked to free-stream disturbances at similar frequencies. As shown in Appendix B.3, the spectrum of the free-stream does not show any peaks at this frequency and as a results, further investigation is required into the cause of this low-frequency component of flapping and the associated spectral peak.

4.3 Spanwise Flow Development

The previous sections have focused on the streamwise development of the flow and how it relates to formation and development of shear layer vortices during the later stages of separated shear layer transition. This section investigates the spanwise development of the flow over the airfoil suction side through top view separation bubble visualization sequences and the cross-correlation analysis of velocity signals acquired simultaneously with the rake of hot-wires across the span.

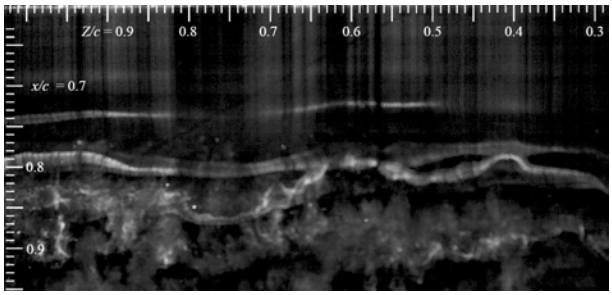
4.3.1 High-Speed Top View Flow Visualization

Figures 4.39-4.41 present sequences of flow visualizations obtained from the top view with a smoke-wire placed within the separated shear layer across the span of the airfoil. In the images, the direction of the free-stream is from top to bottom. At angles of attack of $\alpha = 5$ and 8°, the smoke-wire is visible within the images, and, at $\alpha = 0°$, the wire is located above each image outside the field of view. Like in Figures 4.9-4.11, these visualizations show the separated shear layer rolling up into spanwise oriented vortices, which appear in the images as tube-like filaments of smoke. Once shed, these vortices convect and break down into smaller structures, which convect further downstream. This essentially describes what is visible in side view separation bubble visualizations (Figs. 4.13-4.15) but from a perspective that allows for spanwise aspects of this phenomenon to be studied.

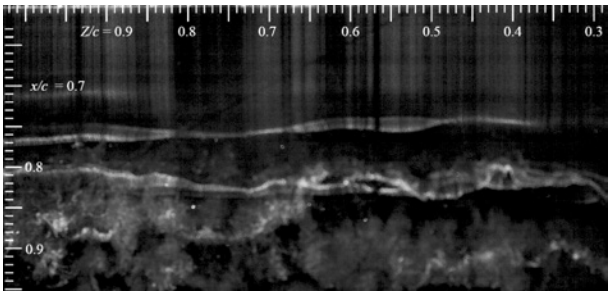
The images show that downstream of the smoke-wire, waves contained within the smoke become visible in the streaklines ahead of the formation of roll-up vortices. For example, these waves are visible in Figure 4.40b at $x/c = 0.4$ and are followed by the emergence of a spanwise-coherent roll-up vortex in Figures 4.40c-4.40f, which forms at $x/c \approx 0.45$. This process is also visible at $\alpha = 0°$ in Figures 4.39a-4.39d between $0.75 \lesssim x/c \lesssim 0.8$, and at $\alpha = 8°$ in Figures 4.41b-4.41f between $0.25 \lesssim x/c \lesssim 0.3$. The streamwise location of the waves suggests that they are likely caused by the flapping of smoke within the separated shear layer ahead of roll-up investigated in Section 4.2.4.

Like the top view visualizations presented in Section 4.1.2 (Figs 4.9-4.11), the sequences show that shear layer roll-up occurs coherently across the span. While the perspective of the top view images makes it difficult to estimate $\overline{x_{roll}}$, roll-up appears to be initiated at approximately $x/c \approx 0.8$, 0.4, and 0.25 at $\alpha = 0$, 5, and 8°, respectively, which are close to the values of $\overline{x_{roll/c}}$ obtained from side view visualizations.

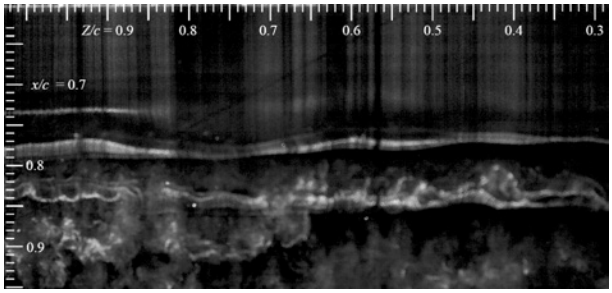
Once shed, the roll-up vortices begin to display waviness across the span. At $\alpha = 0°$, c-shaped vortices [14] are clearly visible in Figure 4.39g between $0.8 < x/c < 0.85$ and $-0.7 < Z/c < -0.45$. These c-shaped vortices are joined at 'arms' [14] spaced approximately $0.1c$ to $0.15c$ apart, which gives a measure of the spanwise wavelength of waves across the



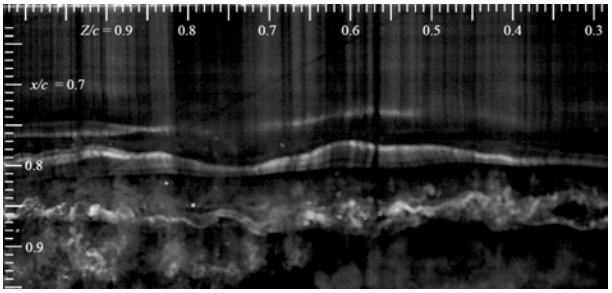
(a) $\Delta t = 1$ ms



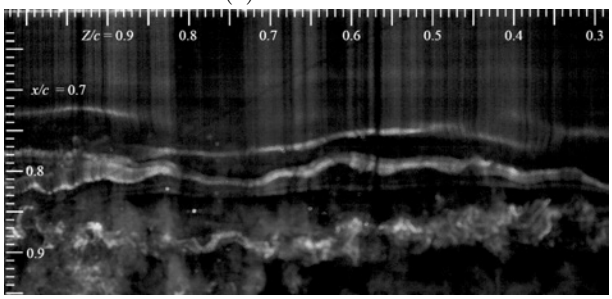
(b) $\Delta t = 2$ ms



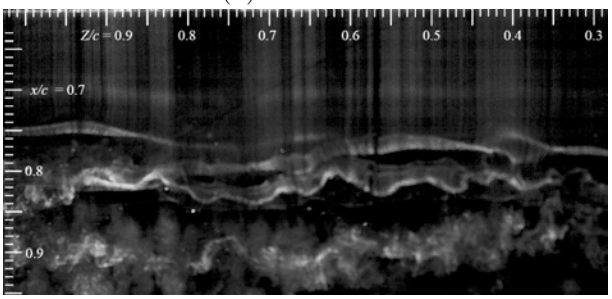
(c) $\Delta t = 3$ ms



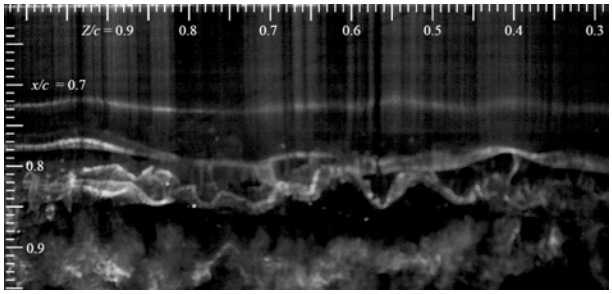
(d) $\Delta t = 4$ ms



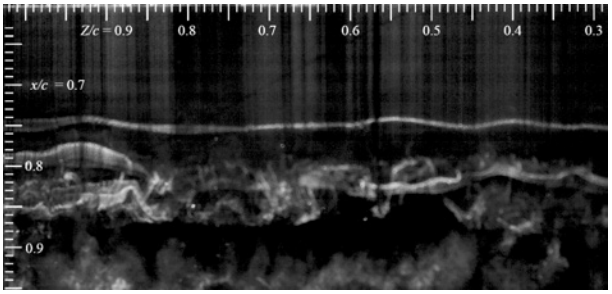
(e) $\Delta t = 5$ ms



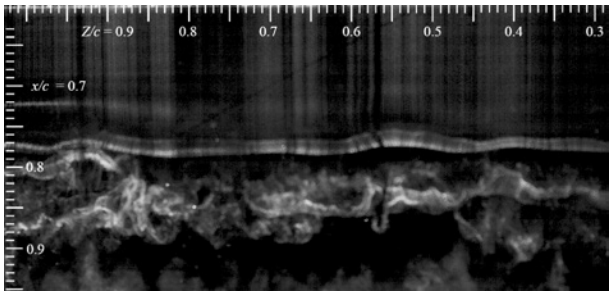
(f) $\Delta t = 6$ ms



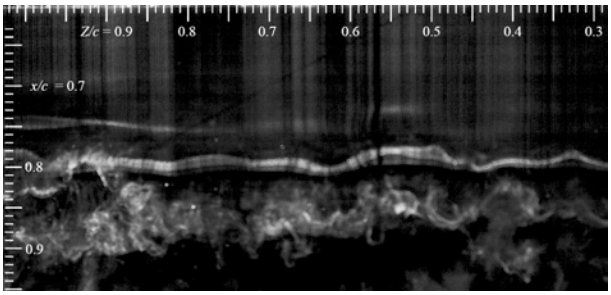
(g) $\Delta t = 7$ ms



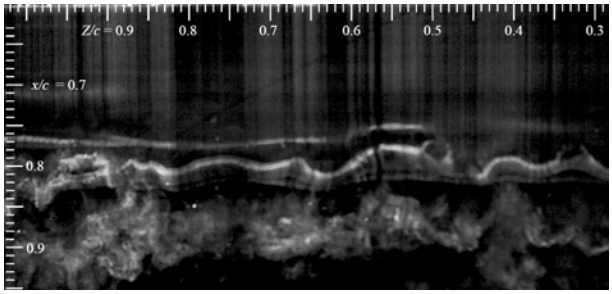
(h) $\Delta t = 8$ ms



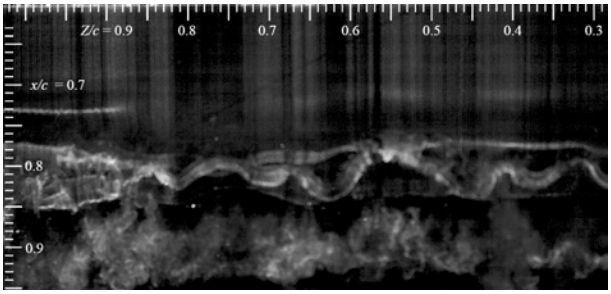
(i) $\Delta t = 9$ ms



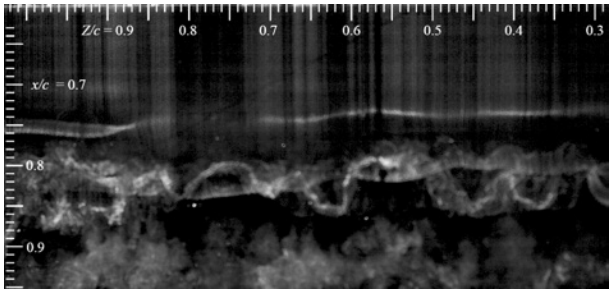
(j) $\Delta t = 10$ ms



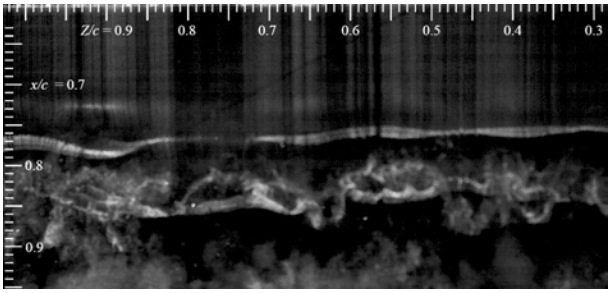
(k) $\Delta t = 11$ ms



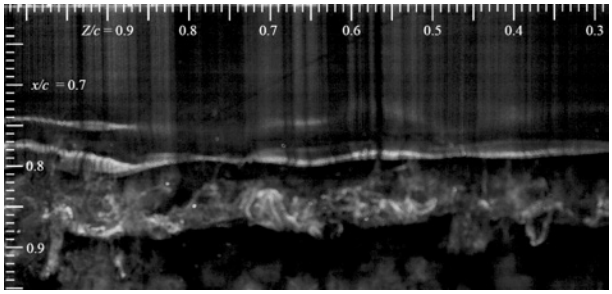
(l) $\Delta t = 12$ ms



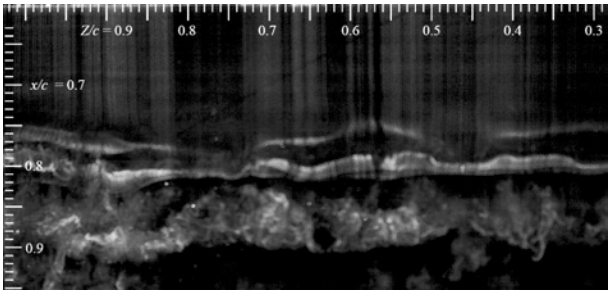
(m) $\Delta t = 13$ ms



(n) $\Delta t = 14$ ms

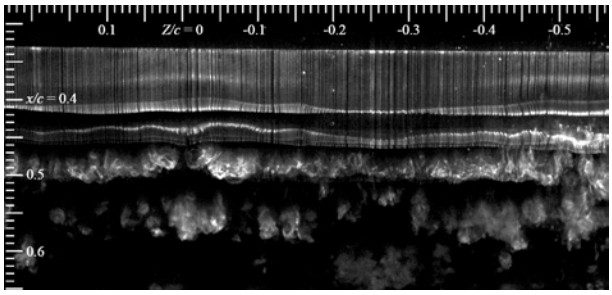


(o) $\Delta t = 15$ ms

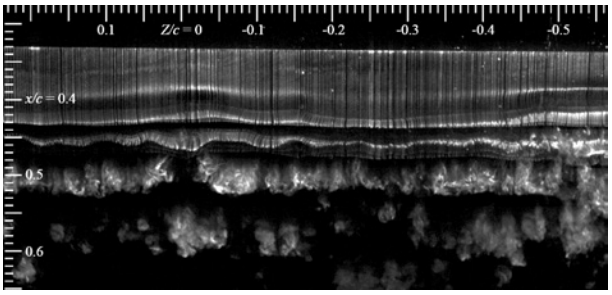


(p) $\Delta t = 16$ ms

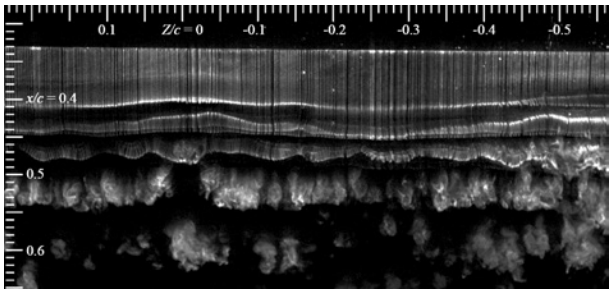
Figure 4.39: Sequence of top view high-speed flow visualizations acquired at $\alpha = 0°$.



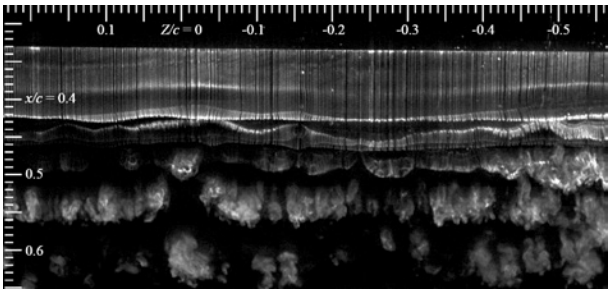
(a) $\Delta t = 0$ ms



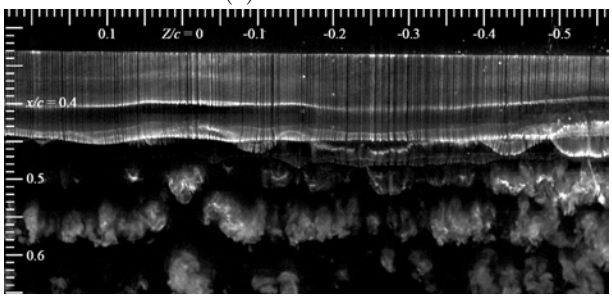
(b) $\Delta t = 0.5$ ms



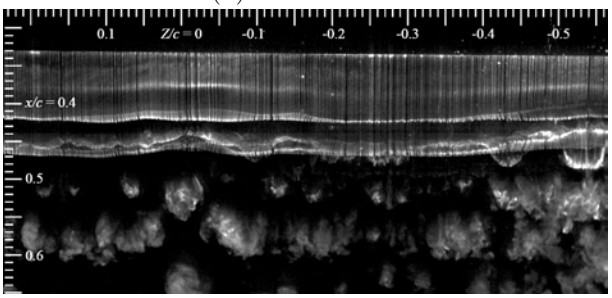
(c) $\Delta t = 1$ ms



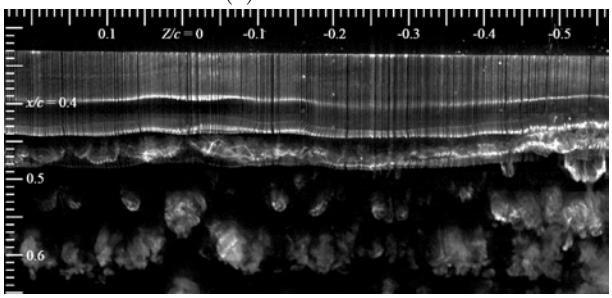
(d) $\Delta t = 1.5$ ms



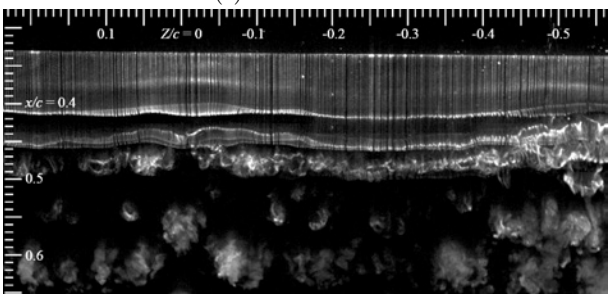
(e) $\Delta t = 2$ ms



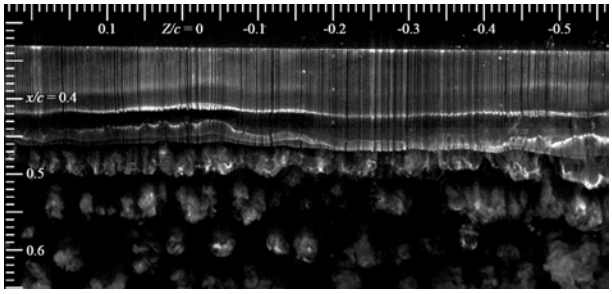
(f) $\Delta t = 2.5$ ms



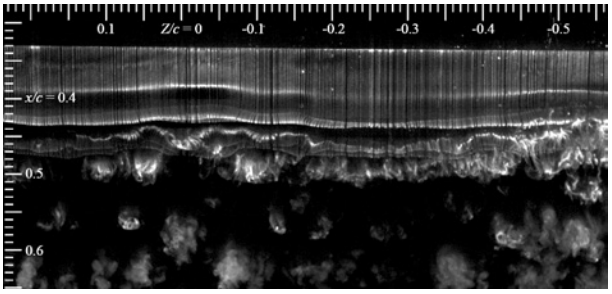
(g) $\Delta t = 3$ ms



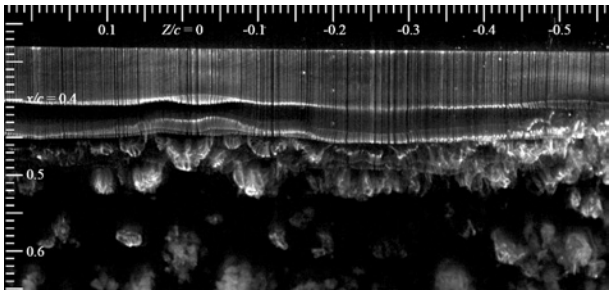
(h) $\Delta t = 3.5$ ms



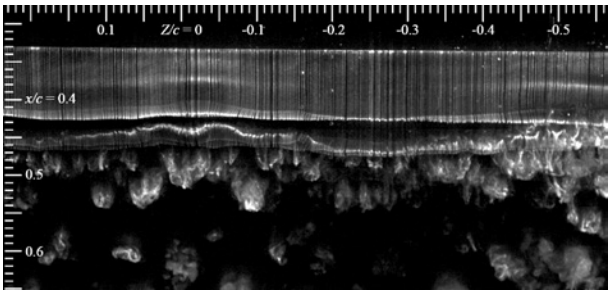
(i) $\Delta t = 4$ ms



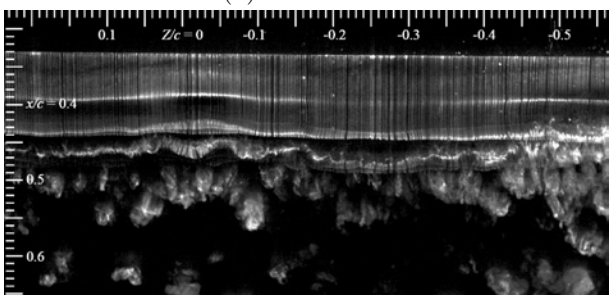
(j) $\Delta t = 4.5$ ms



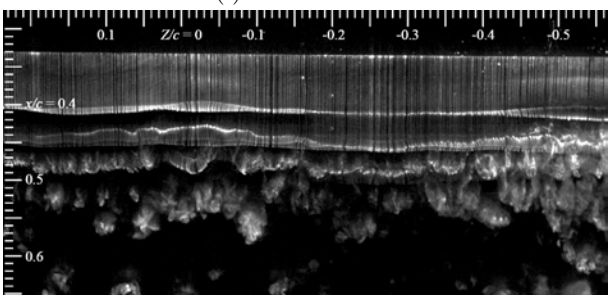
(k) $\Delta t = 5$ ms



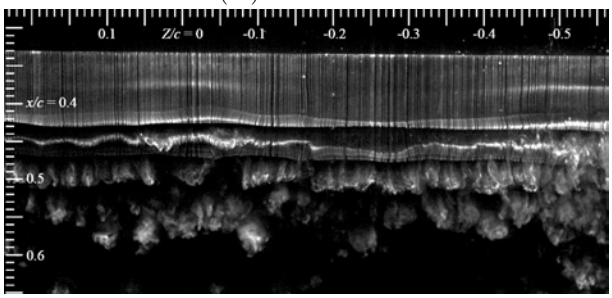
(l) $\Delta t = 5.5$ ms



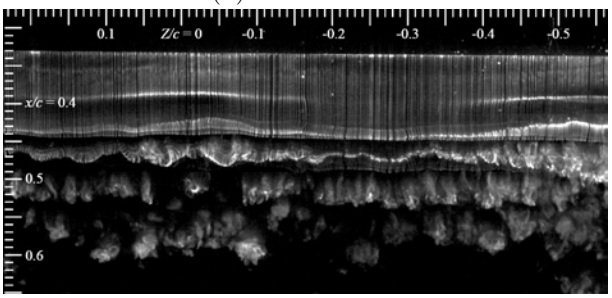
(m) $\Delta t = 6$ ms



(n) $\Delta t = 6.5$ ms

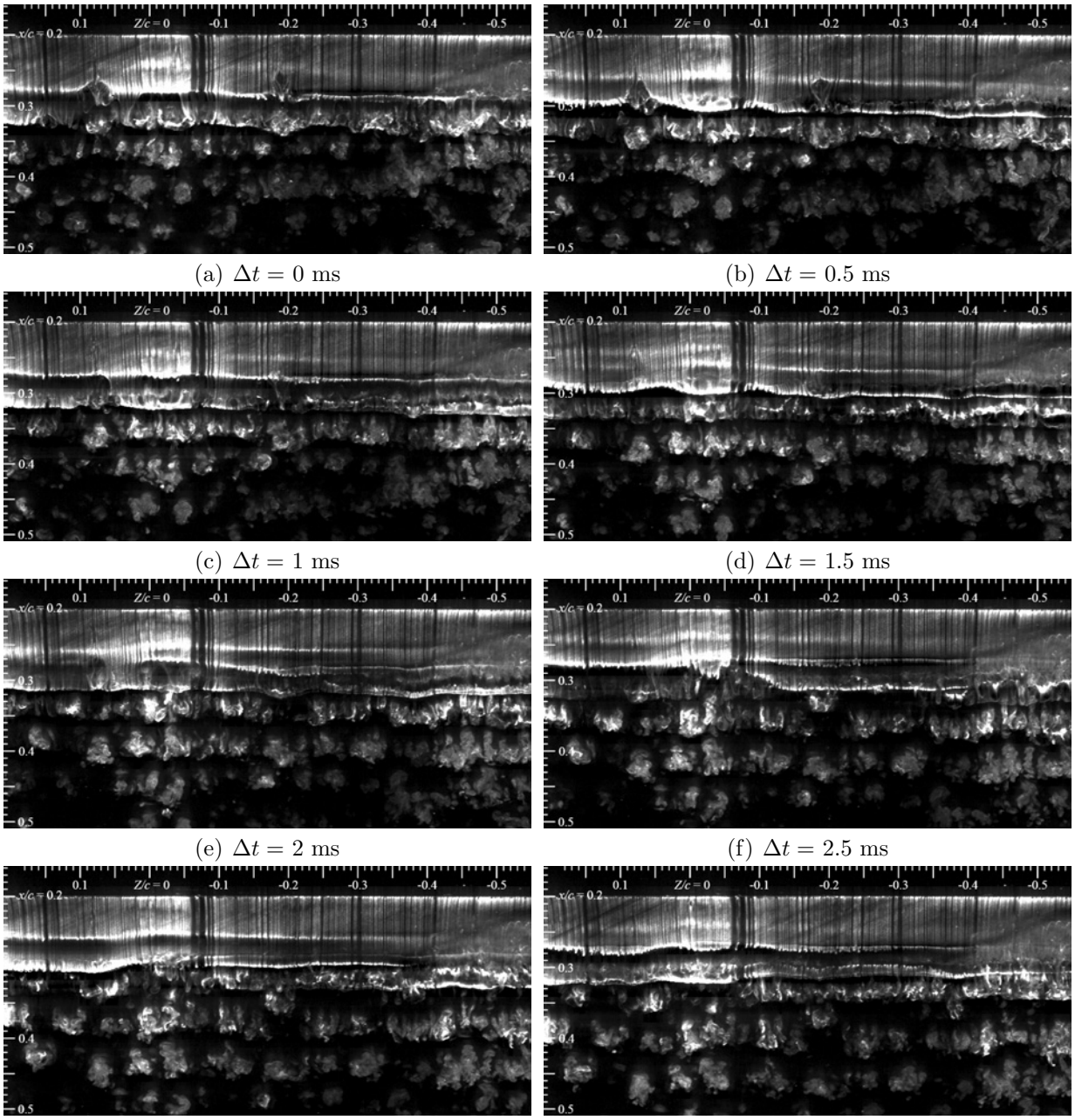


(o) $\Delta t = 7$ ms



(p) $\Delta t = 7.5$ ms

Figure 4.40: Sequence of top view high-speed flow visualizations acquired at $\alpha = 5°$.



(a) $\Delta t = 0$ ms (b) $\Delta t = 0.5$ ms

(c) $\Delta t = 1$ ms (d) $\Delta t = 1.5$ ms

(e) $\Delta t = 2$ ms (f) $\Delta t = 2.5$ ms

(g) $\Delta t = 3$ ms (h) $\Delta t = 3.5$ ms

Figure 4.41: Sequence of top view high-speed flow visualizations acquired at $\alpha = 8°$.

span during breakdown. At this angle of attack, the distinct shape of the c-shaped vortices appears at first in Figure 4.39d at $x/c = 0.8$ and the vortices continue to deform until Figure 4.39g over a period spanning 3 ms. At this point, the streamwise extent of the vortices is approximately $0.05c$ or half the distance between vortex arms and afterwards, these c-shape vortical structures begin to break down. By $\Delta t = 4$ ms (Fig. 4.39i), the distinct shape of the c-shaped structures is no longer visible. Similar c-shaped vortices are also visible at $\alpha = 5°$ throughout the sequence, however, at this angle of attack, the streamwise extent and spanwise wavelength of the structures is approximately half of what was observed at $\alpha = 0°$. The spanwise waviness of the vortices at $\alpha = 8°$ is more subtle when compared to the lower angles of attack, which indicates that the roll-up vortices may undergo less deformation ahead of transition at larger angles of attack. This may be due to a lack of time and space induced by larger shedding rates. The spanwise deformation of structures ahead of breakdown has been observed in several studies on airfoils Burgmann and Schröder [14], Jones et al. [15] and flat plates [13, 29]. In particular, the formation of c-shaped vortices in these visualizations is very similar to the vortices observed by Burgmann and Schröder [14] over the suction side of an SD7003 airfoil operating at lower Reynolds numbers. However, Burgmann and Schröder [14] observed complex interactions between the vortex arms of the c-shaped vortices leading to the deformation of these structures into screwdriver vortices with streamwise-oriented arms.

The top view visualizations presented in Section 4.1.2 (Figs 4.9-4.11) showed that streamwise-oriented structures are visible within the breakdown region of spanwise vortices. The high-speed image sequences confirm that these structures emerge during the breakdown of roll-up vortices. At $\alpha = 5°$, Figure 4.40i shows that organized streamwise-oriented structures appear at $x/c = 0.49$. These structures are spaced approximately $0.2c$ to $0.3c$ across the span. Streamwise-oriented vortices also appear at $\alpha = 8°$ near $x/c \approx 0.35$ and are spaced approximately $0.01c$ to $0.02c$ across the span consistent with the observations made earlier in Figure 4.11. As these structures emerge during breakdown, they appear to be related to secondary streamwise vortices observed in past studies on airfoils [15, 21] and flat plates [13, 25], which have been linked to instability originating within the braid region between consecutive vortices [15]. This suggests that a similar instability mechanism occurs at angles of attack of 5 and 8°.

The visualizations show that, at $\alpha = 5$ and 8°, patterns of structures formed during the breakdown of roll-up vortices convect downstream towards the trailing edge past mean reattachment. The observation of smaller-scale structures past mean reattachment agrees with the results of a number of past studies on airfoils [14, 18–20] and on flat plates [22, 23, 29]. Also, the patterns observed in this study, are similar to the patterns of transitioned structures generated from PIV measurements downstream of reattachment by

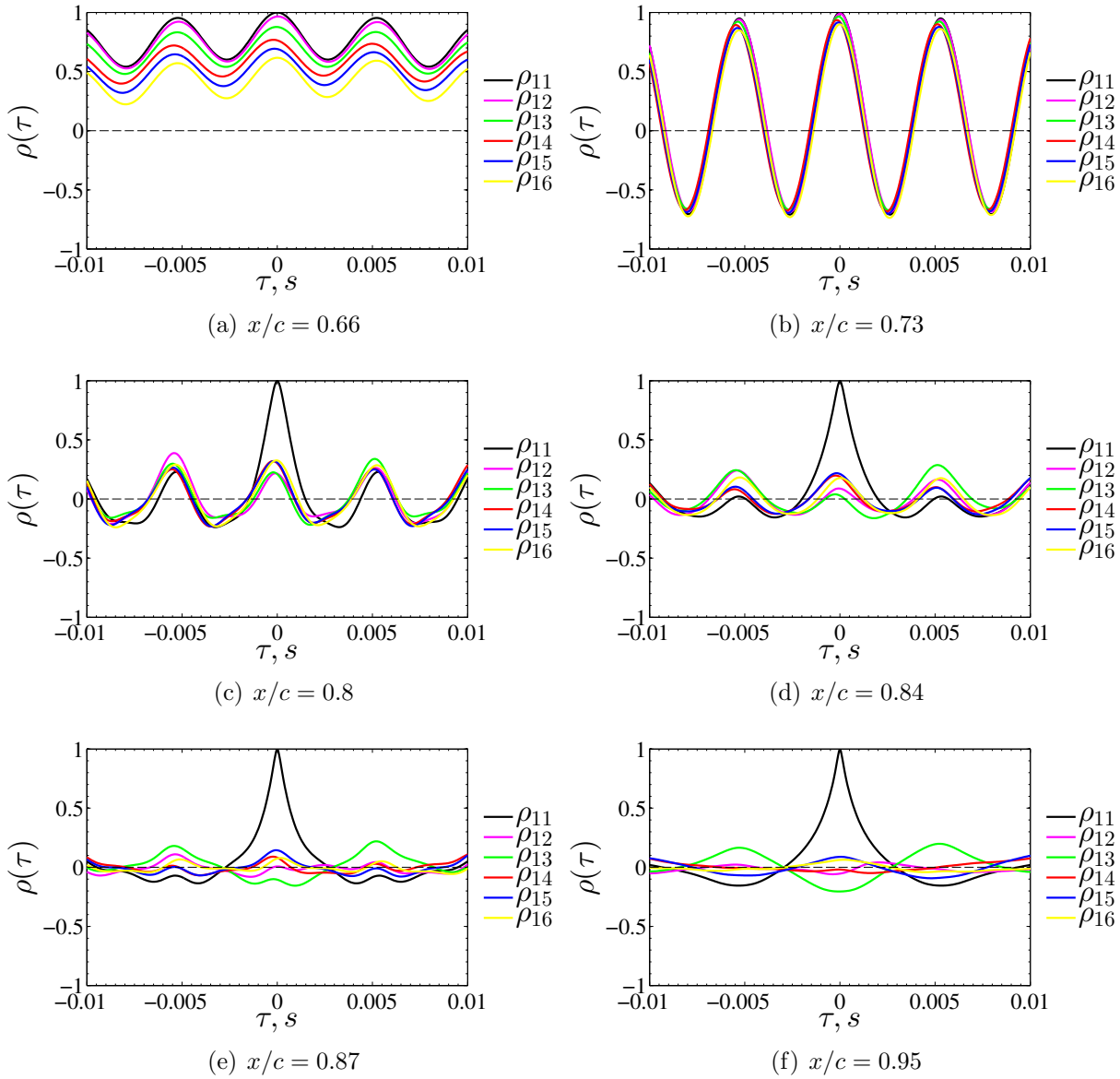
Wolf et al. [17], which were observed to persist even further past the trailing edge and into the wake of an SD7003 airfoil.

Vortex merging is also visible within the images sequences at $\alpha = 5°$ (Fig. 4.40), with the merging of two spanwise vortices occurring across the span at $x/c \approx 0.45$ between 1.5 ms $\leq \Delta t \leq$ 3 ms. Before merging, the first shed vortex, shown in 4.40d Figure at $x/c = 0.45$, already exhibits significant spanwise waviness. A second vortex then proceeds to merge with the first structure and the combined structures breaks down into streamwise-oriented structures, which are visible in Figure 4.40i at $x/c \approx 0.48$. While vortex merging may be common at $\alpha = 5°$, it does not appear to be responsible for the initial deformation of vortices, as the first vortex in the example exhibits waviness at the onset of merging. As shown in the side view visualizations (Fig. 4.14), merging causes the breakdown of the first vortex or vortices near the wall through vortex stretching, which is indicative of an elliptic instability [13]. Marxen et al. [13] showed that elliptical instability may also lead to the spanwise waviness of roll-up vortices as is observed in these sequences. This suggests that vortex merging is not the primary cause of vortex breakdown but may play a part in accelerating this process when it occurs. Also, as the generation of streamwise-oriented vortices can take place without vortex merging at both $\alpha = 5$ and 8°, this suggests that vortex merging is not responsible for the formation of these types of structures. Ultimately, the strong streamwise and spanwise deformation of shear layer vortices and the generation of streamwise structures during breakdown suggest that an elliptical instability and potentially an instability contained within the braid region could exist simultaneously within separation bubbles investigated in this study, which supports the results of Jones et al. [15] and Marxen et al. [13].

4.3.2 Cross-Correlation Analysis

A cross-correlation analysis was performed on velocity signals acquired simultaneously with the rake of hot-wire probes to study disturbance growth within the separated shear layer ahead of roll-up and the subsequent formation and development of roll-up vortices. During these measurements, the rake was positioned at the displacement thickness, $y = \delta^*$, for each x/c location investigated. The analysis was performed on velocity signals of 2^{23} samples acquired over a period of approximately seven minutes. The cross-correlated signals were divided into 256 non-overlapping rectangular windows and normalized cross-correlation functions were computed for each window; the resulting functions of all the windows were averaged to obtain $\rho(\tau)$.

Figures 4.42-4.44 present cross-correlation coefficient functions computed from signals acquired at α =0, 5, and 8°. The cross-correlation functions are plotted at x/c locations ahead of $\overline{x_{roll}}$ past mean reattachment. The indices of each function, $\rho_{ij}(\tau)$, refer to the

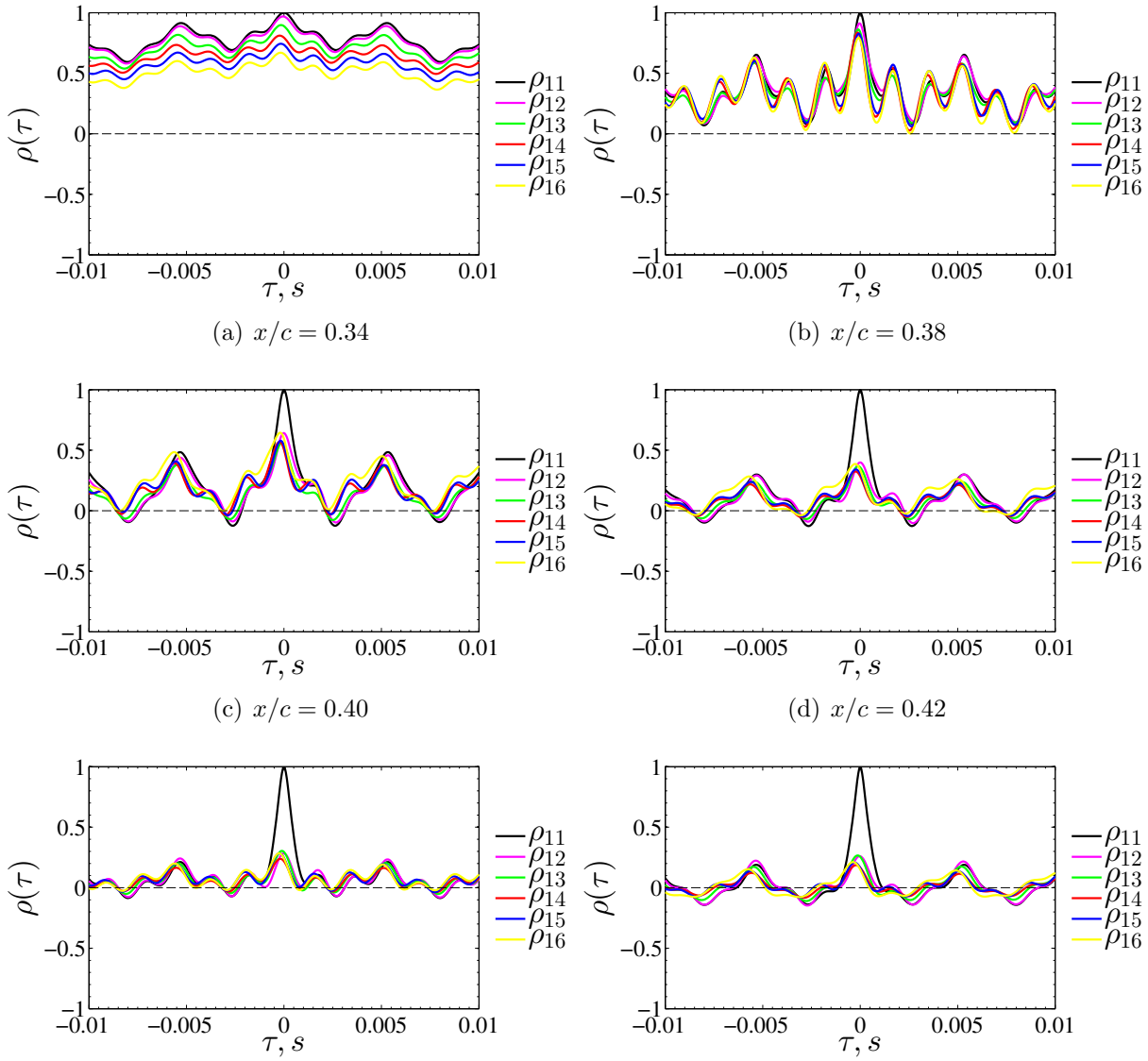


(a) $x/c = 0.66$ (b) $x/c = 0.73$

(c) $x/c = 0.8$ (d) $x/c = 0.84$

(e) $x/c = 0.87$ (f) $x/c = 0.95$

Figure 4.42: Cross-correlation coefficient functions computed from velocity signals acquired simultaneously across the rake of hot-wires at $\alpha = 0°$ with Probe 1 used as reference.

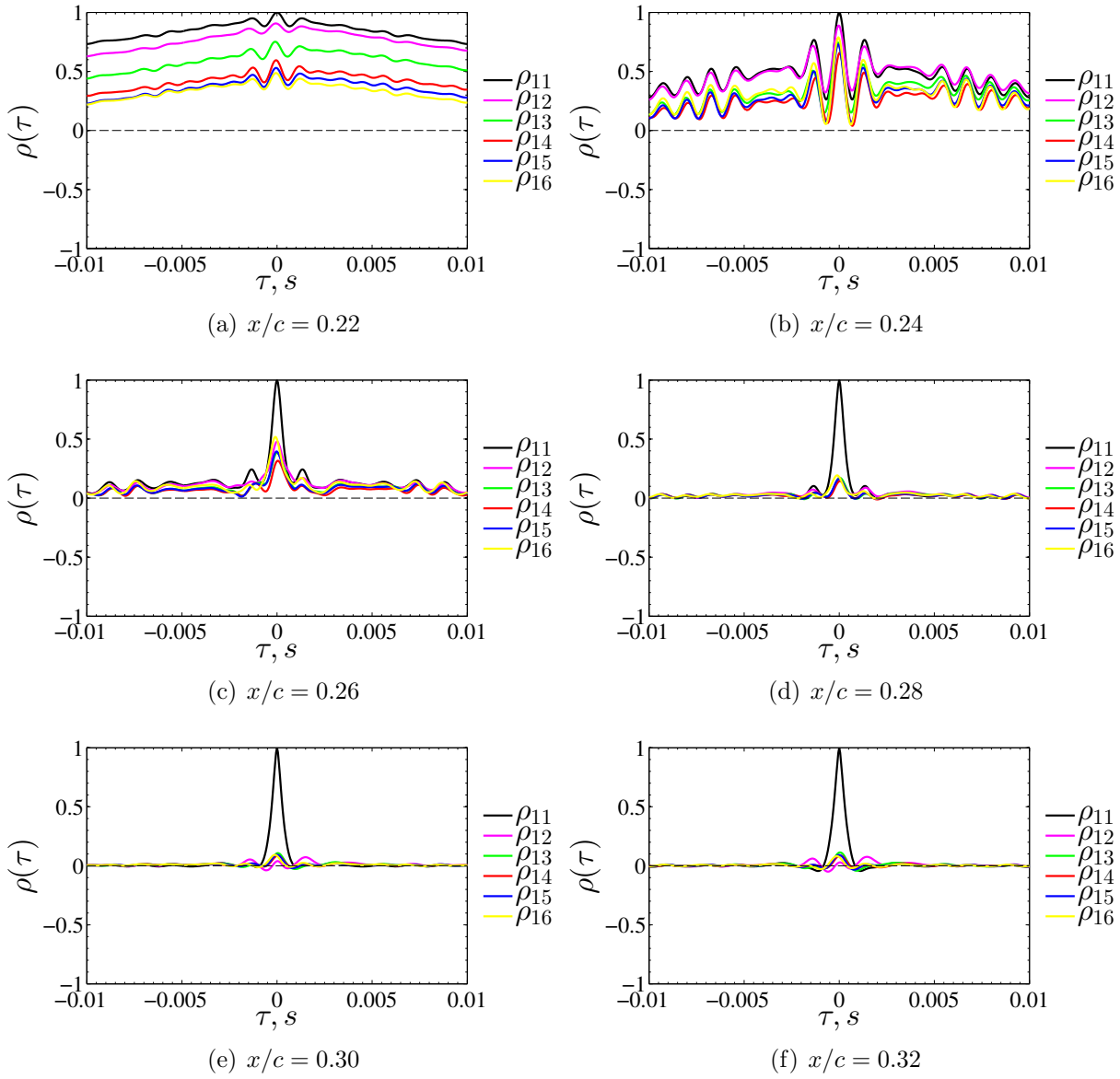


(a) $x/c = 0.34$ (b) $x/c = 0.38$

(c) $x/c = 0.40$ (d) $x/c = 0.42$

(e) $x/c = 0.44$ (f) $x/c = 0.48$

Figure 4.43: Cross-correlation coefficient functions computed from velocity signals acquired simultaneously across the rake of hot-wires at $\alpha = 5°$ with Probe 1 used as reference.



(a) $x/c = 0.22$ (b) $x/c = 0.24$

(c) $x/c = 0.26$ (d) $x/c = 0.28$

(e) $x/c = 0.30$ (f) $x/c = 0.32$

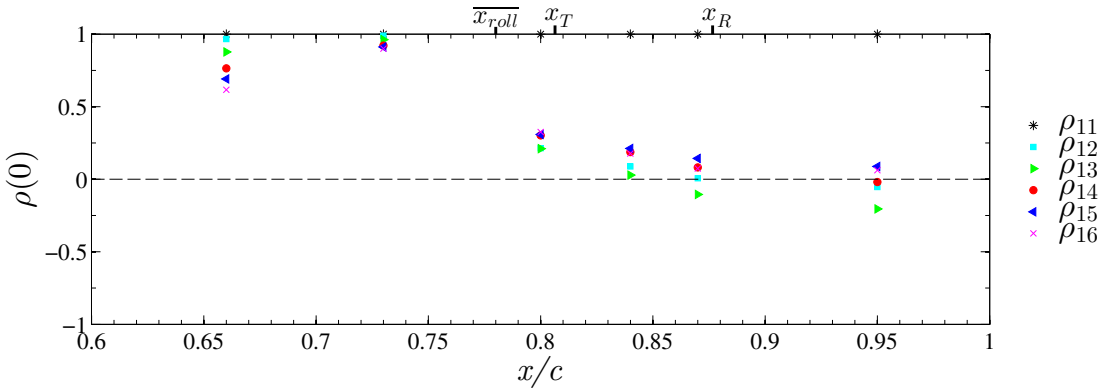
Figure 4.44: Cross-correlation coefficient functions computed from velocity signals acquired simultaneously across the rake of hot-wires at $\alpha = 8°$ with Probe 1 used as reference.

numbers of the probes in the rake diagram shown in Fig. 3.5. The plots give the correlation between two signals at given time lags, τ, with oscillations present within the functions an indication that similar frequency-centred activity is contained within the two cross-correlated signals. The functions may include oscillations from different frequencies, which become superimposed with the amplitude of the oscillations at these frequencies giving and indication as to which disturbances are most dominant within the signals.

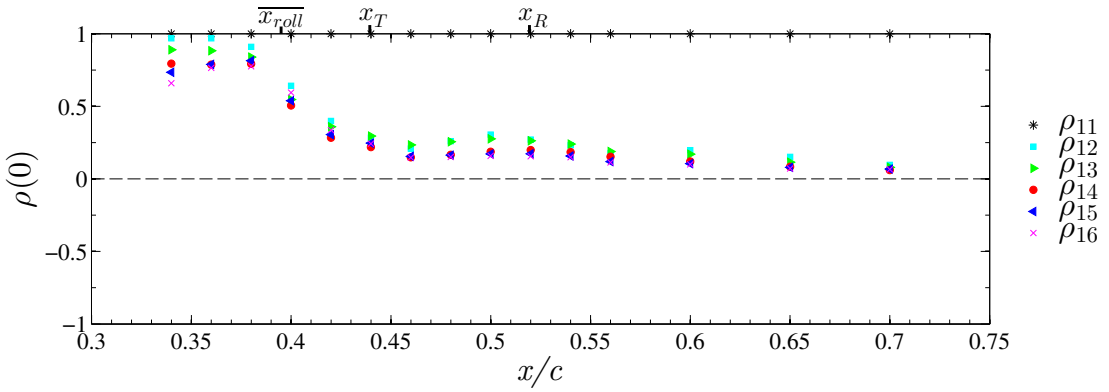
The figures show that cross-correlation functions, computed at $x/c = 0.66$,0.34 and 0.22 for α =0, 5, and 8° (Figs 4.42a, 4.43a, 4.44a), respectively, feature oscillations corresponding to frequencies within the unstable band of disturbances. These oscillations are superimposed onto low-frequency oscillations corresponding to energy content at frequencies below 100 Hz. Ahead of $\overline{x_{roll}}$ (Figs 4.42b, 4.43b, 4.44b), the oscillations pertaining to unstable disturbances become dominant as their amplitude increases. Downstream of $\overline{x_{roll}}$, at $x/c > 0.73$, 0.4 and 0.26 for α =0, 5, and 8°, respectively, the deformation and breakdown of vortices causes the amplitude of all oscillations to decrease significantly.

The figures show that the frequencies amplified in the cross-correlation functions are related to frequencies within the velocity spectra (Figs 4.26-4.28). At $\alpha = 0°$, only oscillations at $f \approx 190$ Hz and its first harmonic are present in the signals and correspond to the large peak within the unstable disturbance band. At $\alpha = 5°$, oscillations pertain to $f \approx 188$ Hz and its first two harmonics are present in each function, while at $\alpha = 8°$, oscillations near $f \approx 660$ Hz are contained within the functions.

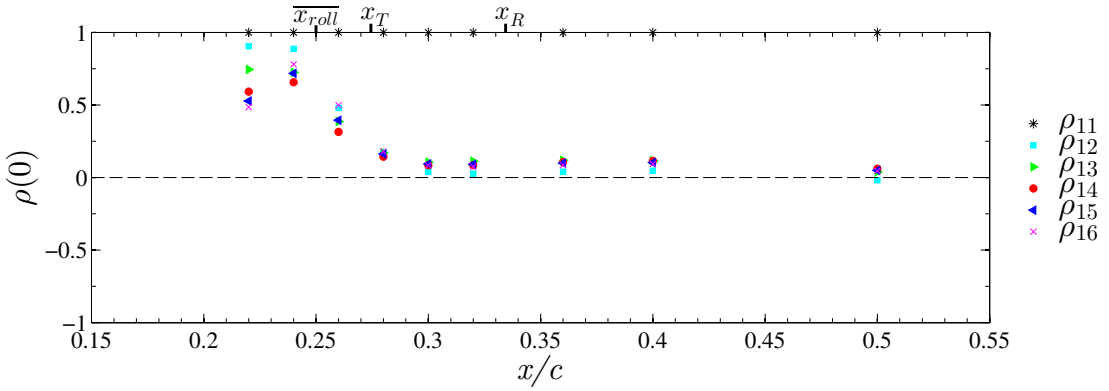
The cross-correlation coefficient, $\rho(0)$, may be used to quantify the degree of spanwise correlation between two signals. Figure 4.45 presents the streamwise progression of $\rho(0)$ at α =0, 5, and 8°. Mean separation, transition, reattachment, and roll-up locations have been marked on each plot. The results show that similar trends occur between the coefficients at each α. Upstream of $\overline{x_{roll}}$, the correlation coefficients are well-correlated across the span, which implies that a nearly two-dimensional growth of disturbances causes roll-up to occur coherently across the span. Past roll-up, the correlations decrease until they become essentially uncorrelated as roll-up vortices deform and break down. The extent over which the coefficients decay decreases with increasing angle of attack, which suggests that breakdown occurs over a shorter distance at larger angles of attack. Negative correlations are even observed at $\alpha = 0°$ between the signals acquired by Probes 1 and 3. The distance between these probes is on the order of half the spanwise wavenumber of c-shape vortices observed in the visualizations, which suggests that this negative correlation may be due to the deformation of these roll-up vortices.



(a) $\alpha = 0°$



(b) $\alpha = 5°$



(c) $\alpha = 8°$

Figure 4.45: Correlation coefficients computed from velocity signals acquired simultaneously with the rake of hot-wires at $y = \delta^*$ with Probe 1 used as reference. $\overline{x_{roll}}$, x_T, and x_R are marked on the plot.

Chapter 5

Conclusions

The later stages of separated shear layer transition within separation bubbles forming over a NACA0018 airfoil were investigated experimentally at a chord Reynolds number of $Re_c = 10^5$ and at angles of attack of $\alpha = 0$, 5, 8, and 10°. The main objectives of this investigation were (1) to study the formation and development of roll-up vortices and their role in separated shear layer transition, and (2) to link the results of flow visualizations obtained within the separation bubble to the streamwise and spanwise development of boundary layer measurements performed over the airfoil. A novel high-speed flow visualization technique with a smoke-wire placed within the separated shear layer across the span of the airfoil allowed for the formation and development of roll-up vortices to be studied through the qualitative and quantitative analysis of image sequences. Streamwise velocity measurements performed with a rake of hot-wire probes and fluctuating surface pressure acquired with microphones embedded into the airfoil model allowed for mean, fluctuating and spectral aspects of the flow field to be studied.

This investigation comprehensively shows how roll-up vortices fit into separation bubble dynamics in both streamwise and spanwise directions. The results show that the growth of unstable disturbances within the separated shear layer leads to the formation of roll-up vortices. Vortices emerge following the initial growth of disturbances and coincide approximately with the onset of nonlinear interactions between disturbances, which define the later stages of transition. Following formation, roll-up vortices proceed to convect downstream, while undergoing significant spanwise deformations. Top view flow visualizations show that the breakdown of vortices is linked to the formation of organized secondary structures, which persist downstream of reattachment. In some cases, interactions between roll-up vortices lead to the merging of up to three vortices.

The flow visualization results shows that laminar-to-turbulent transition does not occur at a fixed location but rather over a region, which may change cycle-to-cycle. Vortex

shedding within the separation bubble also implies that reattachment does not occur at a fixed location but rather over a range of time-varying locations [14, 15]. As a result, the benefit of mean transition and reattachment locations is questionable in certain engineering applications that must consider dynamic aspects of the flow. However, as vortices form an essential part of separated shear layer transition, there is still significant value towards engineering design applications in linking roll-up vortices to boundary layer measurements, which could lead to improved airfoil design and performance prediction tools. In particular, this investigation shows that, $\overline{x_{roll}}$ precedes the mean transition location estimated from surface pressure distributions and coincides approximately with several notable features present in boundary layer parameter (Fig. 4.24) and disturbance amplitude plots (Fig. 4.25). At $\alpha = 5$ and 8°, $\overline{x_{roll}}$ lies near the maximum values of the displacement thickness, δ^*, and where the streamwise rate of change in momentum thickness experiences a strong increase. While the location of the maximum displacement thickness within the separation bubble has been used to estimate mean transition [14, 42], in this investigation, it appears to indicate the onset of shear layer roll-up and the later stages of transition. The change in the streamwise growth of the momentum thickness suggests that roll-up vortices also contribute to the enhanced momentum exchange caused by transition. The results show that the RMS velocity and RMS fluctuating surface pressure may also be related to certain aspects of vortex formation. The nonlinear growth of disturbances, which precedes mean roll-up, coincides approximately to where the amplitude of the RMS velocity reaches about $0.1\,U_\infty$. Also, the magnitude of the RMS velocity at mean roll-up is similar to what was observed by Burgmann et al. [27] in their study over an SD7003 airfoil operating at $Re_c = 20{,}000$. This suggests that, once the amplitude of disturbances reaches a certain level, the onset of nonlinear interactions between disturbances initiates the roll-up of the separated shear layer. This knowledge could be applied towards the improvement of less-costly numerical simulations and models aimed at characterizing airfoil performance. The streamwise development of the RMS surface pressure demonstrates that there is a link between the increase in the streamwise growth rate of the RMS surface pressure and strong vertical velocity fluctuations, which directly precede the formation of shear layer vortices. This suggests that microphones may effectively detect the formation and decay of roll-up vortices, which could be useful in active flow control applications.

The results show that vortex shedding frequency increases approximately linearly with angle of attack and that the Strouhal number of vortex shedding falls within a similar range of values observed by Burgmann and Schröder [14]. The shedding frequency lies near the central frequency of the frequency band of unstable disturbances amplified within the separated shear layer, agreeing with the results of previous studies over airfoils [15, 16] and flat plates [47, 49]. Vortex drift velocity increases with angle of attack and lies between 33% and 44% of the edge velocity within the laminar portion of the separation bubble.

The increasing trend was also observed by Burgmann and Schröder [14] with values of U_{drift}/U_{infty} of a similar magnitude. The convection velocity of surface pressure disturbances obtained in this investigation shows a good agreement with the drift velocity of vortices at $\alpha = 8°$. At $\alpha = 5°$, U_c is approximately 20% lower than the vortex drift velocity estimated from the flow visualizations. This discrepancy could be related to the impact of vortex merging on convection velocity estimations as suggested by the presence of a valley in a plot of U_c/U_{infty} against α in a parametric study of pressure disturbances over the same model performed by Boutilier and Yarusevych [7].

The side view flow visualization sequences show that, at $\alpha = 5°$, up to three roll-up vortices can merge. Periods corresponding to high relative frequencies of double and triple vortex merging indicate that these types of mergers may occur cyclically. The spectra obtained at $\alpha = 5°$ show not only peaks near $f \approx 190$ Hz but at harmonics of this frequency. As the second harmonic lies within the unstable disturbance frequency band, it is hypothesized that forcing at this frequency may be causing triple vortex merging to occur and alternate with double merging due to a slight difference between f_0 and the second harmonic.

Spectra computed from the displacement of smoke within the separated shear show that the separated shear layer flaps vertically at frequencies contained within the unstable frequency band of disturbances. The frequency of the flapping motion at $\alpha = 0°$ matches the frequency of vortex shedding and of the most amplified disturbances within the separated shear layer. Also, at $\alpha = 5°$, a component of flapping is associated with $f \approx 190$ Hz, which corresponds to the low-frequency peak which lies outside the unstable disturbance band at this frequency. This agrees with the results of Dovgal et al. [10] and Hain et al. [20], who showed that a low-frequency component of flapping is related to a spectral peak centred on a frequency below the frequency band of unstable disturbances. However, while Dovgal et al. [10] and Hain et al. [20] associated this low-frequency flapping to disturbances contained within the free-stream, this does not appear to be the case in this study and the source of this energy content requires further investigation.

Top view separation bubble flow visualizations show that at $\alpha = 0$, 5, and 8°, shear layer roll-up occurs with spanwise uniformity. This is not the case at $\alpha = 10°$, where roll-up appears less coherent across the span. At $\alpha = 0$ and 5°, roll-up vortices deform significantly into c-shaped structures prior to breaking down, while at $\alpha = 8°$ the deformation across the span is minor. Furthermore, the streamwise and spanwise scale of the c-shaped vortices decreases between $\alpha = 0$ and 5°. These observations suggest that the magnitude of deformation experienced by roll-up vortices is influenced by angle of attack. This may be due to instability mechanisms, which can lead to vortex deformation based on the size of vortices [13, 15].

The breakdown of roll-up vortices leads to the formation of smaller-scale structures,

which persist into the reattached boundary layer. At $\alpha = 5$ and 8°, streamwise-oriented structures are visible within the flow visualizations during breakdown and may be related to streamwise-oriented vortices observed in past studies [13, 15, 21, 25], which have been linked to a hyperbolic instability generated within the braid region between consecutive vortices [15].

A cross-correlation analysis of velocity signals obtained within the separated shear layer shows that velocity signals are well-correlated across the span ahead of mean roll-up. This indicates that the initial disturbance growth occurs approximately two-dimensionally, which leads to the spanwise coherent roll-up visible in the top view flow visualizations and past studies on airfoils [21, 27] and flat plates [22–24, 26]. Downstream of $\overline{x_{roll}}$, the laminar-to-turbulent transition of roll-up vortices through their deformation and breakdown causes spanwise correlations to decrease and become essentially uncorrelated prior to reattachment.

Chapter 6

Recommendations

The results of this thesis have generated important questions regarding shear layer vortices within laminar separation bubbles. As a result, a number of recommendations pertaining to the flow physics have emerged from this investigation and are as follows:

1. Further investigate the link between roll-up vortices and surface pressure measurements. The results of this study show that the growth of the RMS surface pressure increases significantly at the mean onset of shear layer roll-up, and that these fluctuations begin to decay near the mean transition location. This has been linked to large vertical fluctuations introduced by these vortices closer to the wall, which suggests that vortices have a large effect on the fluctuating surface pressure. By performing simultaneously acquired flow visualizations and microphone measurements across the chord, the relationship between surface pressure signals and vortex shedding may be established. This could allow for future vortex detection algorithms to be developed, which could potentially improve the development and implementation of active flow control systems.

2. Investigate the development of roll-up vortices parametrically. While this study was not strictly parametric, the results show that there are some significant differences on how shear layer vortices are generated and subsequently develop depending on the angle of attack. Also, valleys present in the convection velocity plot in the parametric study of Boutilier and Yarusevych [33] over the same geometry could be related to vortex merging but this requires further investigation. A parametric study with simultaneous flow visualization and microphone measurements would help answer such questions, however, this may be very time consuming and difficult without boundary layer profile data at certain angles of attack. Thus, as an alternative to flow visualizations, time-resolved particle image velocimetry (TR-PIV) could be used instead.

3. Investigate the source of peaks near $f \approx 190$ Hz at $\alpha = 0$ and 5° and establish a definite cause as to why they occur at these angles and not at $\alpha = 8^\circ$. Fluctuations near this frequency appear to have a strong effect on the flow as demonstrated by the frequency of separated shear layer flapping at $\alpha = 0$ and 5° and the vortex shedding frequency at $\alpha = 0^\circ$. Such forcing may also be responsible for some of the observations relating to vortex merging observed at $\alpha = 5^\circ$. Thus, it is imperative that the source of these peaks be investigated further.

4. Investigate the effects of subharmonic forcing on the formation of vortices as part of a flow control study. The results of this investigation have shown that there are certain similarities between the merging of shear layer vortices at $\alpha = 5^\circ$ and the vortex merging observed in plane mixing layers undergoing subharmonic forcing by Ho and Huang [55]. By investigating the effect of selective artificial forcing, further insight into vortex merging and transition mechanisms may be obtained. This may be done with acoustic forcing [72] or perhaps locally on the suction side of the airfoil with disturbance strips or plasma actuators.

To facilitate further investigations, it may be worthwhile to improve upon the experimental and post-processing techniques described in this thesis through the following recommendations:

1. Perform future studies with TR-PIV. As shown in this study, flow visualizations are highly valuable tools that allow for a complex flow to be described and certain quantitative aspects to be investigated. However, obtaining at least a two-dimensional flow field would further enrich such results by allowing for vorticity, Reynolds stresses, and the turbulent kinetic energy within the flow to be computed. Also, more recent stereo-scanning [19, 27] and tomographic [77] PIV techniques have shown great promise in studying three-dimensional aspects of flow development and would be particularly useful in studying secondary instability mechanisms within separation bubbles.

2. Develop a vortex detection and tracking algorithm for flow visualizations and/or implement a pre-existing algorithm (e.g. Scarano et al. [78]) for TR-PIV measurements. The motivation behind this is that the extraction of quantitative data from the flow visualizations and/or PIV data relating to the formation and development of vortices is very time consuming and difficult. Having a reliable and accurate algorithm for the flow visualizations analyzed in this study would have reduced the data processing time and perhaps the uncertainty.

3. Improve the spatial resolution of the microphone array in the NACA0018 airfoil model. This outstanding recommendation was originally proposed by Boutilier [43]. In the case

of this study, more microphones placed near the trailing edge would have allowed for the surface pressure in the aft portion of the separation bubble at $\alpha = 0^\circ$ to be measured. Improving the spatial resolution across the chord of the airfoil would be generally useful in studying a variety of separation bubbles at different angles of attack. Also, the current microphone array is incapable of studying whether waves are being propagated upstream near the trailing edge as part of a feedback loop [10]. The results for flow over a splitter plate with a fence by Hudy et al. [73] have shown that detecting these waves is possible.

REFERENCES

[1] B. H. Carmichael. Low Reynolds Number Airfoil Survey. Technical report, NASA Contract Report No. 165803, 1981.

[2] P. B. S. Lissaman. Low-Reynolds-Number Airfoils. *Annual Review of Fluid Mechanics*, 15(1):223–239, January 1983.

[3] T. J. Mueller and J. D. DeLaurier. Aerodynamics of Small Vehicles. *Annual Review of Fluid Mechanics*, 35(1):89–111, January 2003.

[4] M. Gad-el Hak. Control of Low-Speed Airfoil Aerodynamics. *AIAA Journal*, 28(9): 1537–1552, 1990.

[5] M. Gad-el Hak. Flow Control: The Future. *Journal of Aircraft*, 38(3):402–418, May 2001.

[6] E. Nash. Boundary-Layer Instability Noise on Aerofoils. *Journal of Fluid Mechanics*, 382:27–61, 1999.

[7] M. S. H. Boutilier and S. Yarusevych. Parametric Study of Separation and Transition Characteristics over an Airfoil at Low Reynolds Numbers. *Experiments in Fluids*, 52 (6):1491–1506, February 2012.

[8] T. J. Mueller, L. J. Pohlen, P. E. Conigliaro, and B. J. Jansen. The Influence of Free-Stream Disturbances on Low Reynolds Number Airfoil Experiments. *Experiments in Fluids*, 1(1):3–14, 1983.

[9] F. Kody and G. Bramesfeld. Small UAV Design Using an Integrated Design Tool. *International Journal of Micro Air Vehicles*, 4(2):151–164, June 2012.

[10] A. Dovgal, V. Kozlov, and A. Michalke. Laminar Boundary Layer Separation: Instability and Associated Phenomena. *Progress in Aerospace Sciences*, 30:61–94, 1994.

[11] S. Yarusevych, J. G. Kawall, and P. E. Sullivan. Separated-Shear-Layer Development on an Airfoil at Low Reynolds Numbers. *AIAA Journal*, 46(12):3060–3069, 2008.

[12] M. S. H. Boutilier and S. Yarusevych. Separated Shear Layer Transition over an Airfoil at a Low Reynolds Number. *Physics of Fluids*, 24(8):084105–084105–23, 2012.

[13] O. Marxen, M. Lang, and U. Rist. Vortex Formation and Vortex Breakup in a Laminar Separation Bubble. *Journal of Fluid Mechanics*, 728:58–90, July 2013.

[14] S. Burgmann and W. Schröder. Investigation of the Vortex Induced Unsteadiness of a Separation Bubble via Time-Resolved and Scanning PIV Measurements. *Experiments in Fluids*, 45(4):675–691, August 2008.

[15] L. E. Jones, R. D. Sandberg, and N. D. Sandham. Direct Numerical Simulations of Forced and Unforced Separation Bubbles on an Airfoil at Incidence. *Journal of Fluid Mechanics*, 602:175–207, 2008.

[16] L. E. Jones, R. D. Sandberg, and N. D. Sandham. Stability and Receptivity Characteristics of a Laminar Separation Bubble on an Aerofoil. *Journal of Fluid Mechanics*, 648:257–296, April 2010.

[17] E. Wolf, C. Kähler, D. Troolin, C. Kykal, and W. Lai. Time-Resolved Volumetric Particle Tracking Velocimetry of Large-Scale Vortex Structures from the Reattachment region of a Laminar Separation Bubble to the Wake. *Experiments in fluids*, 50(4): 977–988, 2010.

[18] S. Burgmann, C. Brücker, and W. Schröder. Scanning PIV Measurements of a Laminar Separation Bubble. *Experiments in Fluids*, 41(2):319–326, May 2006.

[19] W. Zhang, R. Hain, and C. J. Kähler. Scanning PIV Investigation of the Laminar Separation Bubble on a SD7003 Airfoil. *Experiments in Fluids*, 45(4):725–743, September 2008.

[20] R. Hain, C. J. Kähler, and R. Radespiel. Dynamics of Laminar Separation Bubbles at Low-Reynolds-Number Aerofoils. *Journal of Fluid Mechanics*, 630:129, June 2009.

[21] W. Balzer and H. Fasel. Direct Numerical Simulation of Laminar Boundary-Layer Separation and Separation Control on the Suction Side of an Airfoil at Low Reynolds Number Conditions. In *40th Fluid Dynamics Conference and Exhibit*, Chicago, IL, 2010. AIAA.

[22] J. H. Watmuff. Evolution of a Wave Packet into Vortex Loops in a Laminar Separation Bubble. *Journal of Fluid Mechanics*, 397:119–169, October 1999.

[23] B. R. McAuliffe and M. I. Yaras. Transition Mechanisms in Separation Bubbles Under Low- and Elevated-Freestream Turbulence. *Journal of Turbomachinery*, 132(1):011004, 2010.

[24] J. R. Brinkerhoff and M. I. Yaras. Interaction of Viscous and Inviscid Instability Modes in SeparationBubble Transition. *Physics of Fluids*, 23(12):124102, 2011.

[25] I. E. Abdalla and Z. Yang. Numerical Study of the Instability Mechanism in Transitional Separating-Reattaching Flow. *International Journal of Heat and Fluid Flow*, 25(4): 593–605, August 2004.

[26] O. Marxen and D. S. Henningson. The Effect of Small-Amplitude Convective Disturbances on the Size and Bursting of a Laminar Separation Bubble. *Journal of Fluid Mechanics*, 671:1–33, March 2011.

[27] S. Burgmann, J. Dannemann, and W. Schröder. Time-Resolved and Volumetric PIV Measurements of a Transitional Separation Bubble on an SD7003 Airfoil. *Experiments in Fluids*, 44(4):609–622, November 2008.

[28] P. R. Spalart and M. Strelets. Mechanisms of Transition and Heat Transfer in a Separation Bubble. *Journal of Fluid Mechanics*, 403:329–349, 2000.

[29] M. Lang, U. Rist, and S. Wagner. Investigations on Controlled Transition Development in a Laminar Separation Bubble by means of LDA and PIV. *Experiments in Fluids*, 36(1):43–52, January 2004.

[30] V. Theofilis. Global Linear Instability. *Annual Review of Fluid Mechanics*, 43(1): 319–352, January 2011.

[31] R. J. Gerakopulos. *Investigating Flow over an Airfoil at Low Reynolds Numbers using Novel Time-Resolved Surface Pressure Measurements*. M.A.Sc. Thesis, University of Waterloo, 2011.

[32] R. Gerakopulos and S. Yarusevych. Novel Time-Resolved Pressure Measurements on an Airfoil at a Low Reynolds Number. *AIAA Journal*, 50(5):1189–1200, May 2012.

[33] M. S. H. Boutilier and S. Yarusevych. Effects of End Plates and Blockage on Low-Reynolds-Number Flows over Airfoils. *AIAA Journal*, 50(7):1547–1559, July 2012.

[34] M. M. O'Meara and T. J. Mueller. Laminar Separation Bubble Characteristics on an Airfoil at Low Reynolds Numbers. *AIAA Journal*, 25(8):1033–1041, 1987.

[35] M. Gaster. The Structure and Behaviour of Laminar Separation Bubbles. Aeronautical Research Council, RM 3595, 1966.

[36] S. Yarusevych, P. E. Sullivan, and J. G. Kawall. On Vortex Shedding from an Airfoil in Low-Reynolds-Number Flows. *Journal of Fluid Mechanics*, 632:245–271, July 2009.

[37] S. Yarusevych and M. S. H. Boutilier. Vortex Shedding of an Airfoil at Low Reynolds Numbers. *AIAA Journal*, 49(10), 2011.

[38] M. Alam and N. D. Sandham. Direct Numerical Simulation of 'Short' Laminar Separation Bubbles with Turbulent Reattachment. *Journal of Fluid Mechanics*, 410 (2003):223–250, 2000.

[39] T. J. Mueller. The Influence of Laminar Separation and Transition on Low Reynolds Number Airfoil Hysteresis. *Journal of Aircraft*, 22(9):763–770, September 1985.

[40] H. Horton. *Laminar Separation Bubbles in Two and Three Dimensonal Incompressible Flow*. Ph.d., University of London, 1968.

[41] H. Schlichting and K. Gersten. *Boundary-Layer Theory, 8th Revised and Enlarged Edition*. Springer-Verlag, Berlin, 2000.

[42] M. Brendel and T. J. Mueller. Boundary-Layer Measurements on an Airfoil at Low Reynolds Numbers. *Journal of Aircraft*, 25(7):612–617, 1988.

[43] M. S. H. Boutilier. *Experimental Investigation of Transition over a NACA 0018 Airfoil at a Low Reynolds Number*. M.A.Sc. Thesis, University of Waterloo, 2011.

[44] O. Marxen and U. Rist. Mean Flow Deformation in a Laminar Separation Bubble: Separation and Stability Characteristics. *Journal of Fluid Mechanics*, 660:37–54, 2010.

[45] O. Marxen, M. Lang, and U. Rist. Discrete Linear Local Eigenmodes in a Separating Laminar Boundary Layer. *Journal of Fluid Mechanics*, 711:1–26, September 2012.

[46] A. Boiko, A. Dovgal, S. Hein, and A. Henning. Particle Image Velocimetry of a Low-Reynolds-Number Separation Bubble. *Experiments in Fluids*, 50(1):13–21, May 2011.

[47] A. V. Boiko, G. R. Grek, A. V. Dovgal, and V. V. Kozlov. *The Origin of Turbulence in Near-Wall Flows*. Springer, 2002.

[48] J. B. Barlow, W. H. Rae Jr., and A. Pope. *Low-Speed Wind Tunnel Testing*. John Wiley & Sons, 3rd edition, 1999.

[49] L. Pauley, P. Moin, and W. Reynolds. The Structure of Two-Dimensional Separation. *Journal of Fluid Mechanics*, 220:397–411, 1990.

[50] Y. Kachanov. Physical Mechanisms of Laminar Boundary-Layer Transition. *Annual Review of Fluid Mechanics*, 26(1):411–482, January 1994.

[51] K. B. Chun and H. J. Sung. Visualization of a locally-forced separated flow over a backward-facing step. *Experiments in Fluids*, 25(2):133–142, July 1998.

[52] T. R. Troutt, B. Scheelke, and T. R. Norman. Organized structures in a reattaching separated flow field. *Journal of Fluid Mechanics*, 143:413–427, April 1984.

[53] C. D. Winant and F. K. Browand. Vortex Pairing: The Mechanism of Turbulent Mixing-Layer Growth at Moderate Reynolds Number. *Journal of Fluid Mechanics*, 63 (02):237, March 1974.

[54] L. Bernal and A. Roshko. Streamwise Vortex Structure in Plane Mixing Layers. *Journal of Fluid Mechanics*, 170:499–525, April 1986.

[55] C.-M. Ho and L.-S. Huang. Subharmonics and vortex merging in mixing layers. *Journal of Fluid Mechanics*, 119:443–473, April 1982.

[56] H. H. Brunn. *Hot-Wire Anemometry: Principles and Signal Analysis*. Oxford University Press, 1995.

[57] M. J. Bishop. *Experimental Investigation of the Effect of Wall Adaptation on Flow Over a Cylinder in a Modernized Adaptive-Wall Wind Tunnel*. University of Waterloo, MASc thesis, University of Waterloo, 2010.

[58] Y. Kubo, M. Miyazaki, and K. Kato. Effects of end plates and blockage of structural members on drag forces. *Journal of Wind Engineering and Industrial Aerodynamics*, 32(3):329–342, October 1989.

[59] P. D. Welch. The Use of Fast Fourier Transform for the Estimation of Power Spectra: A Method Based on Time Averaging over Short, Modified Periodograms. *IEEE Transactions on Audio and Electroacoustics*, AU-15(2):70–73, 1967.

[60] J. G. Kawall, M. Shokr, and J. F. Keffer. A Digital Technique for the Simultaneous Measurement of Streamwise and Lateral Velocities in Turbulent Flows. *Journal of Fluid Mechanics*, 133:83–112, 1983.

[61] H. Bruun and M. Khan. Velocity calibration relationships for hot-wire anemometry. *Journal of Physics E: Scientific Instruments*, 21:225–232, 1988.

[62] S. Yarusevych, P. E. Sullivan, and J. G. Kawall. Smoke-Wire Flow Visualization in Separated Flows at Relatively High Velocities. *AIAA Journal*, 47(6):1592–1595, 2009.

[63] S. M. Batill. Visualization of Transition in the Flow over an Airofil Using the Smoke-Wire Technique. *AIAA Journal*, 19(3):340–345, 1981.

[64] T. J. Mueller and S. M. Batill. Experimental Studies of Separation on a Two-Dimensional Airfoil at Low Reynolds Numbers. *AIAA Journal*, 20(4):457–463, 1982.

[65] A. V. Dovgal, V. V. Kozlov, and O. Simonov. Experiments on Hydrodynamic Instability of Boundary Layers with Separation. In *Boundary-Layer Separation: Proceedings of the IUTAM Symposium*, pages 109–130, London, 1987. International Union of Theoretical and Applied Mechanics.

[66] Y. Watanabe, H. Saeki, and R. J. Hosking. Three-dimensional vortex structures under breaking waves. *Journal of Fluid Mechanics*, 545(-1):291, December 2005.

[67] I. Tani. Low-Speed Flows Involving Bubble Separations. *Progress in Aerospace Sciences*, 5:70–103, 1964.

[68] F. Durst and E. Zanoun. Experimental Investigation of Near-Wall Effects on Hot-Wire Measurements. *Experiments in Fluids*, 33(1):210–218, 2002.

[69] C. P. Häggmark, A. A. Bakchinov, and P. H. Alfredsson. Experiments on a twodimensional laminar separation bubble. *Philosophical Transactions: Mathematical, Physical and Engineering Sciences*, 358(1777):3193–3205, 2000.

[70] C. P. Häggmark, C. Hildings, and D. S. Henningson. A Numerical and Experimental Study of a Transitional Separation Bubble. *Aerospace Science and Technology*, 5(5): 317–328, 2001.

[71] S. Pope. *Turbulent Flows*. Cambridge University Press, Cambridge; New York;, 1 edition, 2000.

[72] S. Yarusevych. *Investigation of Airfoil Boundary Layer and Turbulent Wake Development at Low Reynolds Numbers*. P.h.d. thesis, University of Toronto, 2006.

[73] L. M. Hudy, A. M. Naguib, and W. M. H. Jr. Wall-Pressure-Array Measurements Beneath a Separating/Reattaching Flow Region. *Physics of Fluids*, 15(3):706–717, 2003.

[74] L. M. Hudy, A. Naguib, and W. M. Humphreys. Stochastic estimation of a separated-flow field using wall-pressure-array measurements. *Physics of Fluids*, 19(2):024103, 2007.

[75] D. G. Mabey. Analysis and Correlation of Data on Pressure Fluctuations in Separated Flow. *Journal of Aircraft*, 9(9):642–645, 1972.

[76] T. M. Farabee and M. J. Casarella. Measurements of Fluctuating Wall Pressure for Separated/Reattached Boundary Layer Flows. *Journal of Vibration, Acoustics, Stress, and Reliability in Design*, 108(3):301–307, 1986.

[77] S. Pröbsting, F. Scarano, M. Bernardini, and Pirozzoli. A comparative study of turbulent boundary layer wall pressure fluctuations obtained from high-speed tomographic PIV and DNS. In *16th Int Symp on Applications of Laser Techniques to Fluid Mechanics*, pages 9–12, 2012.

[78] F. Scarano, C. Benocci, and M. L. Riethmuller. Pattern recognition analysis of the turbulent flow past a backward facing step. *Physics of Fluids*, 11(12):3808, 1999.

[79] R. J. Moffat. Describing the Uncertainties in Experimental Results. *Experimental Thermal and Fluid Sciences*, 1(1):3–17, 1988.

APPENDICES

Appendix A

Experimental Uncertainty

An uncertainty analysis of the quantitative data extracted from the high-speed flow visualization and the results of boundary layer measurements is presented in this section. The uncertainty analysis is based on the methodology described in Moffat [79] with uncertainty referring to a two-sided 95% confidence interval. Table A.1 presents a summary of estimated measurement uncertainties described in this section.

A.1 Uncertainty in Experimental Setup

Following the methodology described in Boutilier [43], the free-stream velocity at the model was calibrated against the pressure difference across the wind tunnel contraction. The chord Reynolds number was computed from the free-stream velocity obtained from this calibration. As the calibration and pressure difference across the contraction were both obtained with an inclined manometer of 0.25 Pa minor divisions, the uncertainty in setting the free-stream velocity is related to the precision of this instrument. Thus, the uncertainty of the incline manometer readings is less than 0.5 Pa, which corresponds to approximately 1.5% of the pressure difference at $Re_c = 10^5$. The free-stream velocity of the wind tunnel during experiments was subject to slight fluctuations of less than 1 % of the contraction pressure difference. Combining these sources of error results in a total uncertainty of approximately 2.5 %

The angle of attack of the airfoil, α, was set using a digital protractor with an angular resolution of 0.1°. Along with the accuracy of the protractor, the uncertainty in setting the angle of attack of the model is also influenced by the precision in obtaining aerodynamic zero, which may introduce a bias error. The aerodynamic zero of the airfoil model was set by (i) obtaining surface pressure distributions across a range of positive and negative

Table A.1: Summary of measurement uncertainty estimates

quantity	conditions	uncertainty	applicable tables & figures
C_P		± 0.021	Fig. 4.20
f_0		$\pm$60Hz	Figs. 4.26,4.27,4.28, 4.29, 4.30 & Table 4.3
$f_{shedding}$	α =0, 5, 8, & 10°	$\pm$ 1.4, 1.8, 2.7, & 9.2 Hz	Figs. 4.18, 4.29, & Table 4.1
H		$\pm 0.15H$	Fig. 4.24c
L/c	α =0, 5, 8, & 10°	$\pm$ 0.06, 0.035, 0.027, 0.025	Figs. 4.21
p'/q_∞		$\pm\sqrt{(0.02)^2 + (0.20p'/q_\infty)^2}$	Figs. 4.25b, & B.2
U/U_∞	for $U/U_\infty \gtrsim 0.25$	± 0.05	Figs. 4.22a, & 4.23a
U_c/U_∞	$\alpha = 5°$	± 0.061	
	$\alpha = 8°$	± 0.08	
U_{drift}/U_∞	α =0, 5, 8, & 10°	$\pm$ 0.13, 0.14, 0.18 & 0.27	Figs. 4.19a, & Table 4.1
u'/U_∞	for $U/U_\infty \gtrsim 0.25$	± 0.05	Figs. 4.22b, 4.23b, & 4.25a
Re_c		$\pm 2,500$	
x_R/c	$\alpha = 0°$	± 0.04	Figs. 4.20, & Table 4.2
	$\alpha = 5, 8, 10°$	± 0.02	
x_{roll}/c	α =0, 5, 8, & 10°	$\pm$ 0.013, 0.028, 0.011, & 0.013	Figs. 4.17, 4.21, 4.36, 4.36, & Table 4.1
x_S/c	$\alpha = 0$, and 5°	± 0.02	Figs. 4.20a-b, 4.2, 4.21, & Table 4.2
	$\alpha = 8, 10°$	± 0.01	Figs. 4.20c-d
x_T/c	$\alpha = 0°$	± 0.035	Figs. 4.20, & Table 4.2
	$\alpha = 5, 8,$, and 10°	± 0.02	
y/c		$\pm 2.8 \times 10^{-4}$	Figs. 4.22, & 4.23
Z/c	of hot-wires	± 0.001	
α		$\pm 0.22°$	
δ^*/c		$\pm 0.1\delta^*/c$	Figs. 4.22, 4.23, & 4.24a
$\Delta\tau$	$\alpha = 5°$	$\pm 1.5 \times 10^{-4}$ s	Fig. 4.31a
	$\alpha = 8°$	$\pm 1.41 \times 10^{-3}$ s	Fig. 4.31b
$\rho(0)$		± 0.14	Fig. 4.45
$\tau*$	$\alpha = 5°$	$\pm 1.6 \times 10^{-3}$ s	Fig. 4.32a
	$\alpha = 8°$	$\pm 2.8 \times 10^{-3}$ s	Fig. 4.32b
θ/c		$\pm 0.1\theta/c$	Figure 4.24b

angles near $\alpha = 5$ and 10°, (ii) determining which distributions displayed the best symmetry by comparing the results and lastly, (iii) selecting the angle between the most symmetric distributions [31, 43]. The comparisons were made at angles of attack near $\alpha = \pm 5$ and $\pm 10°$ for distributions obtained over increments of 0.1°, or, the angular resolution of the digital protractor. The estimated error in determining this zero angle is within $\pm 0.1°$. Combined with the angular resolution of the digital protractor, the total error in determining the aerodynamic zero is 0.22°, which agrees with the uncertainty estimates estimated by Boutilier [43].

A.2 Uncertainty in Flow Visualizations

The uncertainty in estimating the streamwise position of shear layer roll-up, x_{roll}, is due to the accuracy of estimating the position the breaking wave feature depicted in Figure 4.17. This quantity is also subject to discretization errors related to the sampling rate of images with the uncertainty in the time at which roll-up occurs within the sampling period of images. Still, it is assumed that the discretization errors caused by the sampling rate will not have a large impact on the roll-up position quantities. Based on this assumption, the bias error in the position of roll-up at each angle of attack is estimated to be within $\pm 0.005c$. The precision error was computed as $0.006c$, $0.014c$, $0.005c$, and $0.006c$ at $\alpha = 0$, 5, 8, and 10°, respectively. This results in a total uncertainty of $0.013c$, $0.028c$, $0.011c$, and $0.013c$ at $\alpha = 0$, 5, 8, and 10°, respectively.

The uncertainty in $f_{shedding}$ was estimated by computing the quantization (or gating error) associated to the frequency calculation. The gating error is estimated by the reciprocal of twice the timing interval and was computed as 1.39, 1.8, 2.7, and 9.21 Hz for α =0, 5, 8, and 10°, respectively.

The total uncertainty in the estimated vortex drift speed, U_{drift}, was computed with the bias error associated to the spatial accuracy of tracking vortex cores and the precision error based on the standard deviation of measurements. The uncertainty of tracking vortices was estimated based on the error in the vortex core displacement between frames. At angles of attack of $\alpha = 0$, and 5°, the estimated uncertainty in the displacement is within 0.5 % of the chord. At angles of attack of $\alpha = 8$ and 10°, the estimated uncertainty is within 0.25 % of the chord. For $\alpha = 0$, 5, 8, and 10°, the resulting bias error in estimating the vortex drift velocity is within 10, 14, 27, and 22% of the free-stream velocity, respectively. Combined with the precision error, the total uncertainty is within 13, 14, 18, and 27% of the free-stream velocity for $\alpha = 0$, 5, 8, and 10°, respectively.

A.3 Uncertainty in Static Pressure Measurements

Static pressure measurements are subject to various sources of error, which contribute to the total uncertainty in surface pressure distributions presented in this study. A detailed approach of this uncertainty analysis may be found Boutilier [43] and are summarized in this section.

The largest source of uncertainty in static pressure measurements is related to the calibration of the pressure transducers. The pressure transducer output voltages were calibrated against an inclined manometer of 0.25 Pa minor divisions, which results in a 0.5 Pa uncertainty. Pressure transducers are also sensitive to changes in temperature and to compensate for the difference between the temperature at calibration and during experiments, a zero pressure offset was obtained prior to obtaining surface pressure distributions. The calibration curve was then shifted by the voltage difference between the zero pressure difference at calibration and zero pressure offset. The Lucas Schaevitz P3061-2WD pressure transducers have a manufacturer specified pressure-voltage response of 0.02%/°C. Over the course of the experiments, the ambient temperature stayed within 5°C of the calibration temperature. This variation has an effect on the pressure-voltage slope of measurements, which is not accounted by the calibration. As a result, the maximum variation in the pressure-voltage slope throughout the experiments is 0.5 Pa.

The surface pressure distributions are also subject to error introduced by changes in the ambient temperature during measurements. The changes in ambient temperature during calibration are considered negligible due to the short time period over which calibration take place. On the other hand, a surface pressure distribution may be obtained in approximately one hour. Yet, as temperature changes within this time period are generally minor and fall within 0.2%/°C, the effect of changing ambient temperature was neglected.

Other sources of error in the static pressure measurements are due to static pressure tap geometry, long-term variations in the measurements, the uncertainty of setting the zero pressure offset, the general repeatability of the experiments, and uncertainty in the angle of attack [43]. Boutilier [43] estimated the uncertainty introduced the static pressure tap geometry and long term variations in the measurements to be less than 0.14 Pa and 0.13 Pa, respectively. The zero pressure voltage offset is subject to a discretization errors of less than 0.05 Pa, and long term variation in the ensemble average of less than 0.13 Pa. The discretization errors also affect the measurement of static surface pressure. Boutilier [43] performed three repeatability tests on different days over a month period and determined that the second standard deviation between each set of measurements was less than 0.03 Pa.

By combining the different source of uncertainty following the technique of Moffat [79], the estimated total uncertainty in the static pressure measurements is 0.74 Pa, or, less than 2.1 % of the free-stream dynamic pressure.

The uncertainty in estimating separation, transition, and reattachment locations from surface pressure distributions was computed by taking one half of the distance between the estimated location and the furthest adjacent tap. While the methodology used to estimate these locations can also have an effect on these estimations, the surface pressure distributions investigated in this thesis show clear features, which reduce the error associated to the methodology, and as a result, was neglected. Based on the spatial resolution of the pressure taps, the estimated uncertainty of the separation, transition, and reattachment locations is within $\pm 0,04c$. Locations estimated near the leading edge of the airfoil have lower uncertainties due to the increasesd spatial resolution of the static pressure taps and is reflected in Table A.1. The uncertainty of the separation bubble length, $L = x_R - x_S$, was estimated by propagating the uncertainty of the separation and reattachment locations and are within 6, 4, 3 and 2.5% of the chord at $\alpha = 0$, 5, 8 and 10°, respectively.

A.4 Uncertainty in Microphone Measurements

The total error in the fluctuating surface pressure measurements is based on calibration error and error associated to background noise in the signals caused by the wind tunnel generator, the wind tunnel fan, electrical noise, and electrical interference. The microphone array was calibrated by Gerakopulos [31], who assumed a linear response between the pressure and the voltage and that the sensitivity of each microphone is constant and independent of frequency. Gerakopulos [31] verified the validity of these assumptions and determined uncertainties of the sensitivity coefficients for each microphone individually. In this study, the more conservative approach of Boutilier [43] was used to estimate the uncertainty in obtaining p'/q_∞. As the largest estimated uncertainty in the microphone calibration data of Gerakopulos [31] is approximately 20 % of the sensitivity coefficient, this value was used as the estimated error due to calibration. An uncertainty of $p'/q_\infty \approx 0.02$ due to background noise was estimated from the lowest value of p'/q_∞ measured during experiments [43]. Combining these values, the total uncertainty in determining p'/q_∞ may be estimated as $\pm\sqrt{(0.02)^2 + (0.20p'/q_\infty)^2}$.

The uncertainty in time lag, $\Delta\tau$, computed in the cross-correlation analysis of simultaneously sampled pressure signals is related to discretization errors introduce by the sampling rate (±0.0001 s for a sampling rate of 10,000 Hz) and the variation in the values obtained between the 256 windows that were averaged to obtain this quantity. The variability of the computations was computed from the standard deviation of the time lags computed for each window and are 1.1×10^{-4}s and 1.4×10^{-3}s at $\alpha = 5$ and 8°, respectively. The total uncertainty was estimated to be within 1.5×10^{-4}s and 1.41×10^{-3}s at $\alpha = 5$ and 8°, respectively.

The uncertainty in computing the accumulated time lag, τ^*, is based on the uncertainty of the time lag and the variability in computing the accumulated time lag between windows used to obtain this average value. The uncertainty due to the variability between windows is 1.6×10^{-3}s and 1.4×10^{-4}s at $\alpha = 5$ and 8°, respectively. Combined with twice the uncertainty of time lag, the total uncertainty of the accumulated time lag is within 1.6×10^{-3}s and 2.8×10^{-3}s at $\alpha = 5$ and 8°, respectively.

The convection velocity of surface pressure disturbances, U_c, was computed by obtaining the slope of a linear least squares line of best fit between the accumulated time lag obtained from averaged cross-correlation functions and the streamwise coordinate. Thus, the uncertainty in computing U_c is based on the uncertainty introduced by the accumulated time lag in estimating the slope of this linear fit. The total uncertainty was estimated to be within 6.1% and 8% of free-stream velocity at $\alpha = 5$ and 8°, respectively.

A.5 Uncertainty in Velocity Measurements

Hot-wire measurements uncertainty may be attributed to various sources of error, which have been the subject of various investigations, e.g. [22, 43, 60, 61]. Based on the results of the study by Kawall et al. [60], for the levels of turbulence intensity obtained in this study, the uncertainty of mean and RMS velocity measurements is estimated to be within 5% of the free-stream velocity for mean velocity measurements greater than approximately 25% of the frees-stream velocity [43]. For velocity measurements below this threshold, the uncertainty is much larger and is affected by low-speed calibration errors [61], hot-wire rectification errors [22], a strong vertical component of velocity within the separation bubble [43], and error due to heat conduction for measurements taken near the airfoil surface [43].

The alignment of probes in the rake was performed optically in situ with a Nikon D300 fitted with a Nikon UV-Nikkor 105 mm f/4.5 macro lens. The rake was placed closely above the model and the airfoil surface was used as a visual reference to estimate the vertical position of each probe. A ruler was placed in the field of view to obtain a millimetre per pixel calibration. The vertical position of each probe was then computed using this calibration, and the vertical alignment was evaluated and adjusted. The vertical alignment of the probes was estimated to be within ±0.1 mm. The streamwise alignment of the rake was also evaluated optically by eye with the aid of a visual reference and was estimated to be within ±0.1 mm. The images obtained during rake alignment revealed small differences and imperfections between each of the probes, such as slight skewness introduced during manufacturing. As a result, the spanwise alignment of the probes was not perfect and the uncertainty in the spanwise position of the probes was estimated at ±0.2 mm. As the probes have a width between the prongs of approximately 2 mm, this was deemed acceptable.

The vertical position of the rake y/c, was determined optically using 12.3 megapixel photos of Probe 1 in the rake taken with a Nikon D300 fitted with a Nikon UV-Nikkor 105 mm f/4.5 macro lens and a Nikon SB-600 speedlight, which were placed outside the test section. A millimetre-per-pixel calibration was obtained by moving the probe approximately 0.1 mm near the surface of the airfoil. The distance between the end of Probe 1 and it's reflection off the surface of the airfoil was used to estimate the vertical position of the probe. Previous studies at the same facility used a calibration grid to estimate the vertical position of the probes [31, 43]. It was determined that the uncertainty in using either of these techniques are comparable and within ± 0.05 mm. This is attributed to the accuracy in determining a pixel to millimetre calibration using the traverse system, and the perspective of the camera in relation to the airfoil, which introduces a slight error. Also, the rake alignment images showed that wires are not perfectly straight between the prongs. The uncertainty introduced by these imperfections in the vertical position of the rake is estimated at 0.025 mm. As a result the combined uncertainty is 0.056 mm or 0.028 % of the chord.

The uncertainty of boundary layer parameters computed from hot-wire measurements is based on errors associated to hot-wire measurements and the computational technique. These parameters were computed, first, from individual profiles and then averaged at each streamwise location. This allows for the variation between estimations of these quantities to be used in the uncertainty analysis. Estimated values of the vertical position of the edge velocity were used to compute the displacement thickness, δ^*, and momentum thickness, θ, for each profile, Any errors introduced in estimating this position resulted in negligible error in these calculations as the velocity of the flow is approximately equal to the edge velocity in this region. Also, errors introduced by not traversing the rake at an angle normal to the curvature of the airfoil are considered negligible in the region of the separation bubble, where the angle between the normal vector and the traverse's trajectory is low, and below 10% in measurements taken towards the trailing edge at angles of attack of $\alpha = 5$ and 8°. It is the uncertainty of hot-wire measurements in the low-speed and reverse flow regions due to the accuracy of low-speed calibration and rectification errors, which introduce the most error in these calculations. Boutilier [43] estimated that these uncertainties affect the displacement and momentum thickness calculations by introducing a bias error in the order of 10% of the free-stream velocity over half of the vertical distance of the displacement thickness in the separation bubble region. Based on the velocity profiles presented in Section 4.2.2, this bias error is also a reasonable estimate for the separation bubbles in this investigation and introduces an estimated less than 5% uncertainty in the displacement and momentum thickness estimation. This, combined with the variation of these parameters computed between probes, results in a total uncertainty of 10% in the estimation of the displacement and momentum thickness at $\alpha = 5$ and 8°, respectively. The total uncertainty

of the shape factor, H, is based on the uncertainty of these parameters and is estimated at 15%.

A.6 Uncertainty in Determining the Central Frequency of the Unstable Disturbance Growth Frequency Band

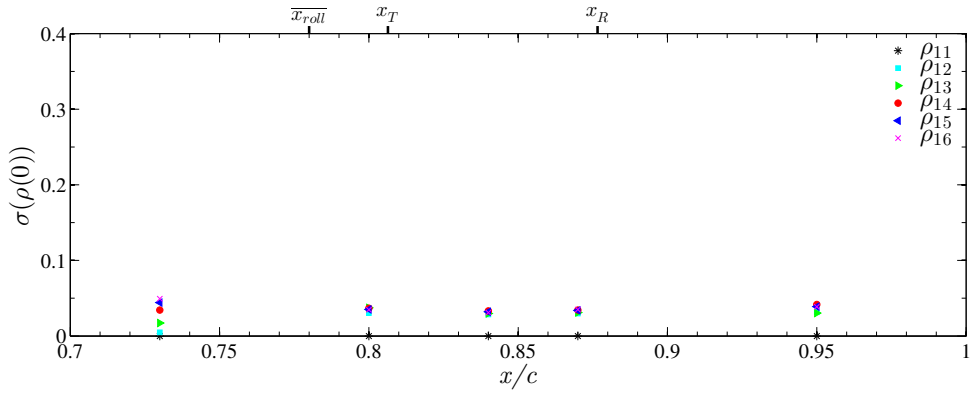
It is common for studies to define a fundamental or central frequency of unstable disturbances to study the scaling of disturbance growth in separated shear layers. This quantity may be subject to substantial variability depending on the technique and the energy content of the spectra, especially in cases with multiple spectral peaks [31, 43].

In this study, the central frequency of the unstable disturbances, f_0, was obtained by first estimating the range of the unstable and then taking f_0 at the centre. Values of the central frequency were obtained from both velocity and surface pressure spectra resulting in differences of up to 32 Hz between f_0. Combined with the uncertainty in estimating the bandwidth disturbance band, which is estimated at ±25Hz, a conservative estimate of the total uncertainty for all values f_0 is ±60Hz.

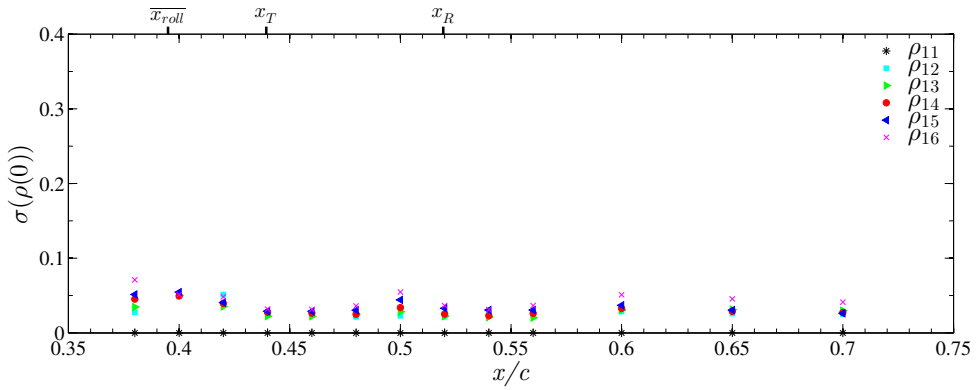
A.7 Uncertainty in Estimating Cross-Correlation Coefficients

Cross-correlation coefficients, $\rho(0)$, were obtained from cross-correlation functions computed from simultaneously sampled velocity signals. As the functions were normalized by the standard deviations of the cross-correlated velocity signals, any bias or calibration errors in the velocity signals should not affect these computations. Furthermore, the velocity signals were obtained at the displacement thickness of each profile, which would reduce any calibration errors. As a result, is difficult to establish the uncertainty of $\rho(tau)$. The cross-correlation coefficients were obtained from cross-correlation functions obtained with 256 windows, which allows for the variation of the cross-correlation coefficients computed between windows to be studied.

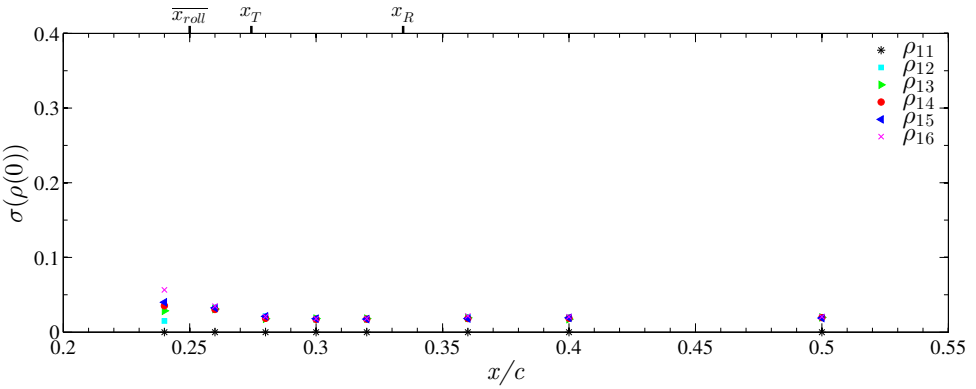
The streamwise development of the standard deviation of cross-correlation coefficient across these windows is presented in Figure A.1. The figures show that the standard deviation between windows are within $0.07\rho(0)$ at all angles of attack and all streamwise locations. A two-sided 95% confidence interval based on this precision error results in an uncertainty within $0.14\rho(0)$.



(a) $\alpha = 0°$



(b) $\alpha = 5°$



(c) $\alpha = 8°$

Figure A.1: Standard deviations of cross-correlation coefficients, $\rho(0)$ computed individually from the 256 windows used in computing the averaged value of $\rho(\tau)$.

Appendix B

Influence of Experimental Setup

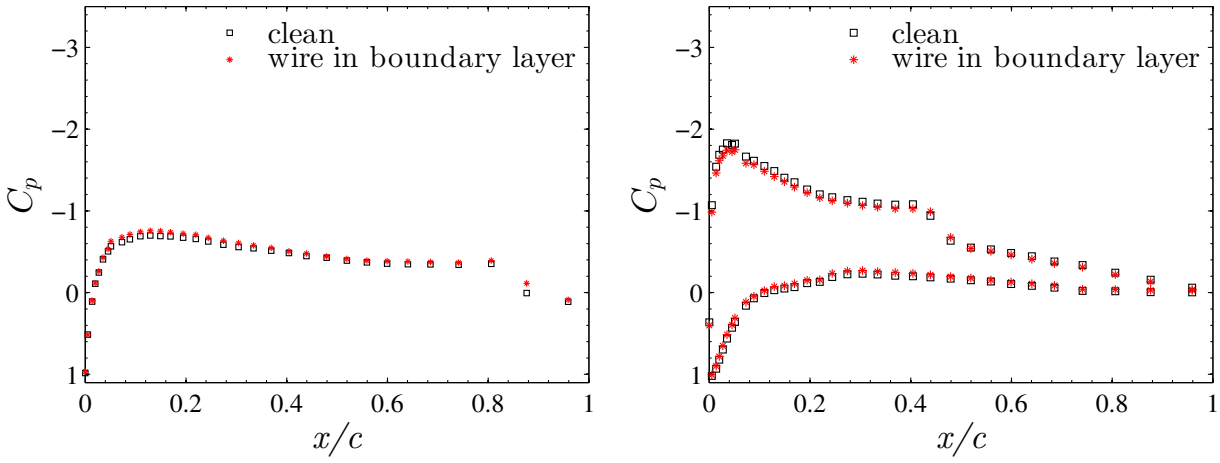
The intrusiveness of the experimental techniques employed in this study requires that the effect of the experimental setup on the flow be evaluated. Specifically, the effect of placing (i) a smoke-wire across the span, and (ii) a rake of six boundary layer hot-wire probes within the separation bubble must be evaluated. Previous studies have shown that placing a single hot-wire probe within a separation bubble forming over an airfoil does affect the flow [42, 43]. While the effect of placing a single hot-wire probe within a separation bubble is usually minor [42, 43], Boutilier [43] showed that this is not the case for bubbles forming towards the leading edge of an airfoil.

The airfoil model allows for the influence of the experimental setup to be evaluated through static and dynamic surface pressure measurements [31, 33, 43]. By comparing the measurements made between different configurations, the intrusiveness of the experimental methods may be evaluated. This section presents the results of these comparative measurements.

B.1 Intrusiveness of Flow Visualization

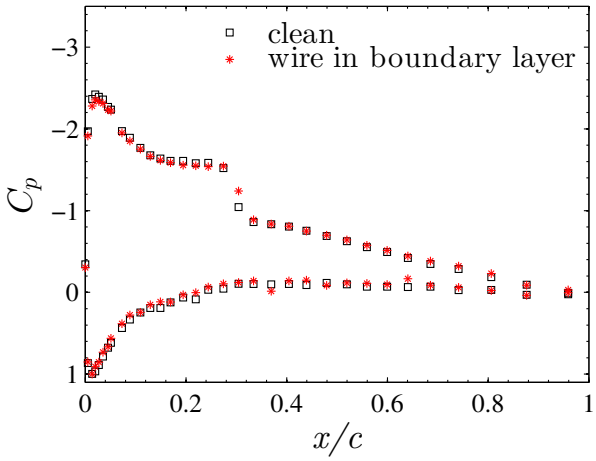
To evaluate the intrusiveness of the smoke-wire placed within the separation bubble surface pressure measurements were performed with (i) a clean airfoil model with end caps and (ii) the smoke-wire placed within the boundary layer across the span. In both configurations, the airfoil model did not have end plates installed. When running measurements in the second configuration, the smoke-wire did not have oil applied. The streamwise and vertical position of the smoke-wire is marked in each figure presented.

Figure B.1 presents model surface pressure distributions for the clean airfoil model and the model with the smoke-wire placed within the boundary layer across the span.

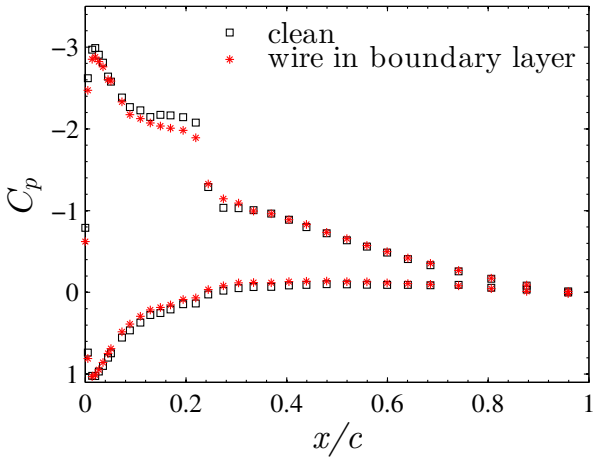


(a) $\alpha = 0°$

(b) $\alpha = 5°$



(c) $\alpha = 8°$



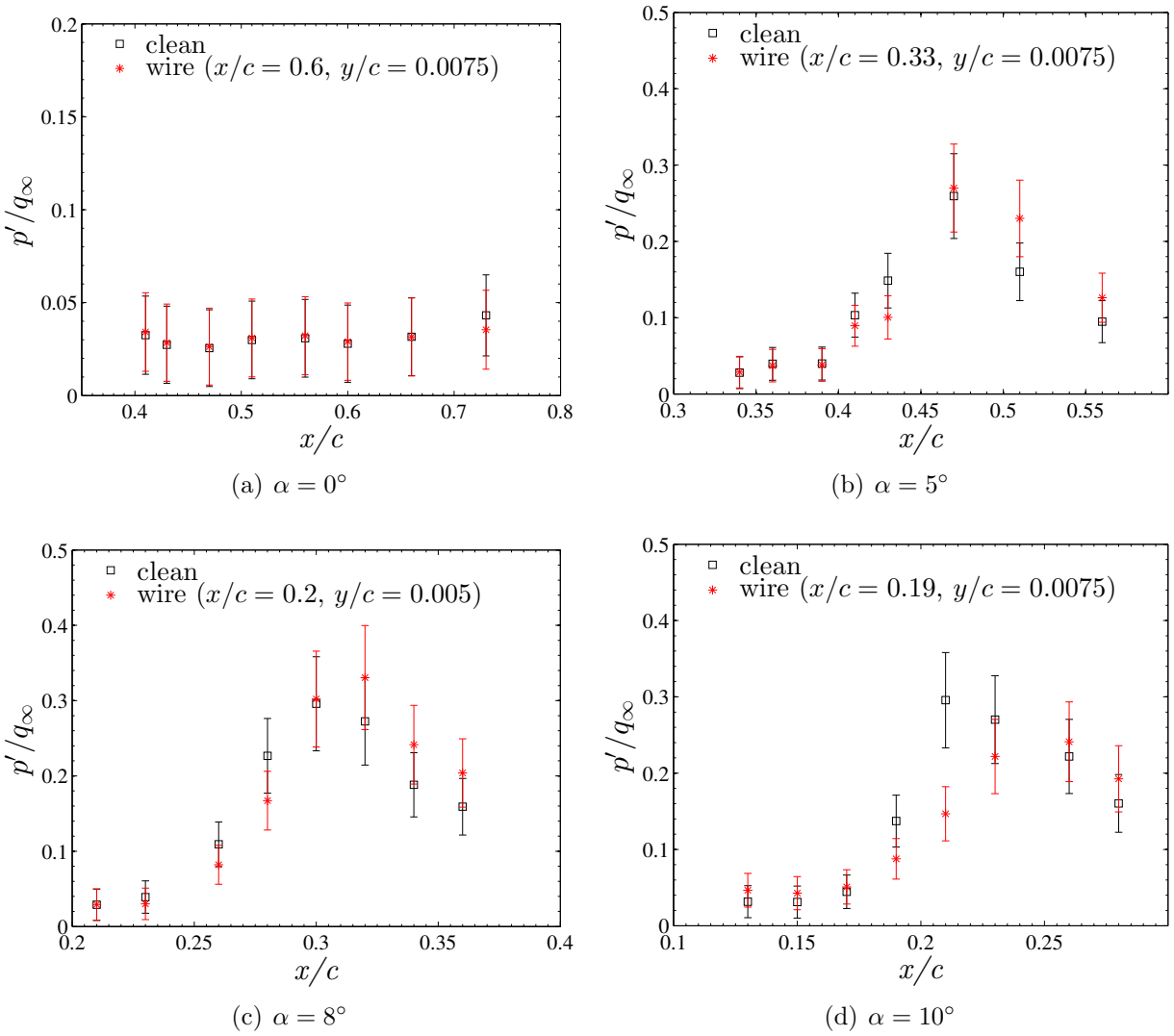
(d) $0\alpha = 10°$

Figure B.1: Model surface pressure distributions acquired with the airfoil fitted with just end caps and with the smoke-wire placed within the separated shear layer over the airfoil.

Qualitatively, between $0° \leq \alpha \leq 8°$, the distributions compare well over both suction and pressure sides of the model. At $\alpha = 8°$, the maximum difference over the pressure side ($\Delta C_P = 0.2$) occurs at $x/c = 0.3$ ahead of mean reattachment. This suggests that the introduction of the smoke-wire results in a slightly earlier transition. At $\alpha = 10°$, the smoke-wire causes a slight change in the slope of the pressure plateau ahead of mean transition when compared to the clean model measurements. This indicates that the wire causes the flow to transition slightly more upstream [43]. However, since reverse flow is visible in the high-speed image sequences, separation and reattachment still occur and the change of the slope of the pressure plateau suggests that the flow in reverse flow accelerates at a larger rate upstream. This behavior is not unusual since flow development is most sensitive to intrusive methods at angles of attack ahead of stall [43]. In general, the percent difference of the surface pressure distributions between the configurations is within $\pm 10\,\%$.

Figure B.2 presents the RMS surface pressure within the growth region of surface pressure fluctuations for the clean airfoil model and the model with the smoke-wire placed within the boundary layer across the span. Error bars demonstrating the estimated uncertainty of the values ($\pm\sqrt{(0.02)^2 + (0.20p'/q_\infty)^2}$) are plotted for both configurations. While the uncertainty of these measurements is large, they may still be used to evaluate the intrusiveness of the smoke-wire on the flow. At $\alpha = 0°$ (Fig. B.2a), the RMS fluctuating surface pressure for both configurations falls well within the estimated uncertainty at all locations. At $\alpha = 5$ and $8°$, the values begin to deviate following the growth of disturbances. Still, the experimental uncertainty of the measurements at these angles overlap, indicating that the effect of the wire does have a strong effect on the flow. At $\alpha = 10°$, measurements in the growth region deviate significantly between the configurations suggesting that the wire has a larger effect at this α.

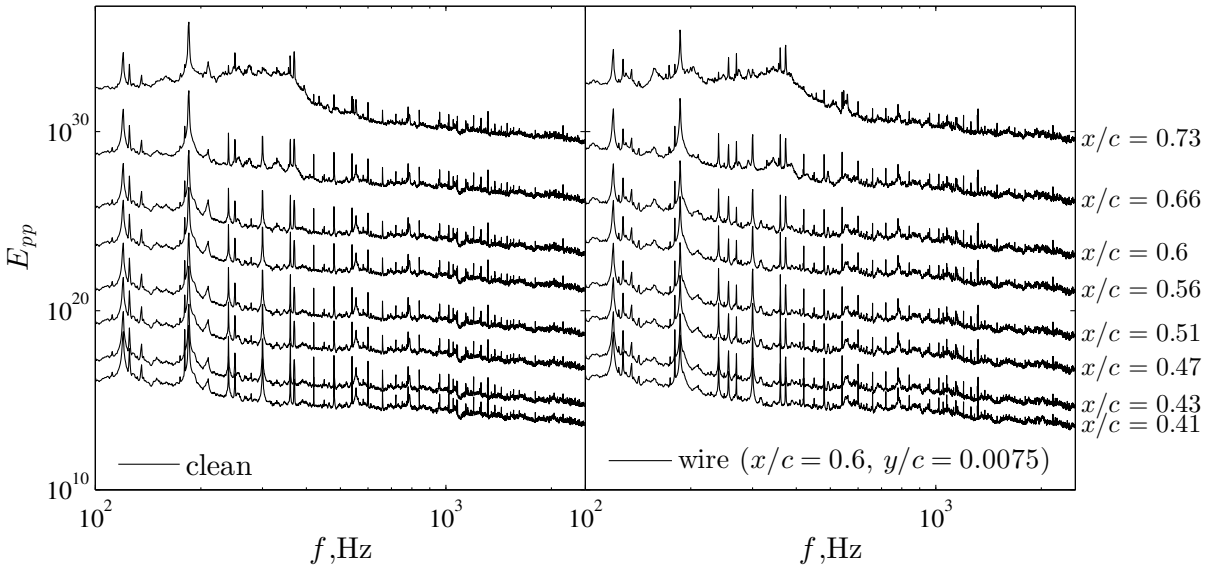
Figure B.3 presents fluctuating surface pressure spectra obtained with both configurations. Each spectrum has been normalized by their respective energy content and shifted proportionally to $10^{x/c}$ for clarity. The spectra do not show any major differences between the configurations. In Figures B.3b-d, the spectra flatten due to transition at the same x/c location. The growth of the most unstable disturbances occurs across approximately the same band with peaks present at the same frequencies. A notable difference is the appearance harmonic and slight subharmonic energy growth of the instability band, which are visible prior to transition. One theory for the appearance of these harmonics is due to sound reflecting off the smoke-wire, which might cause some out-of-phase sound waves to be recorded by the microphones. These results suggest that placing a smoke-wire within the boundary layer does not have a large effect on the results of the flow visualizations.



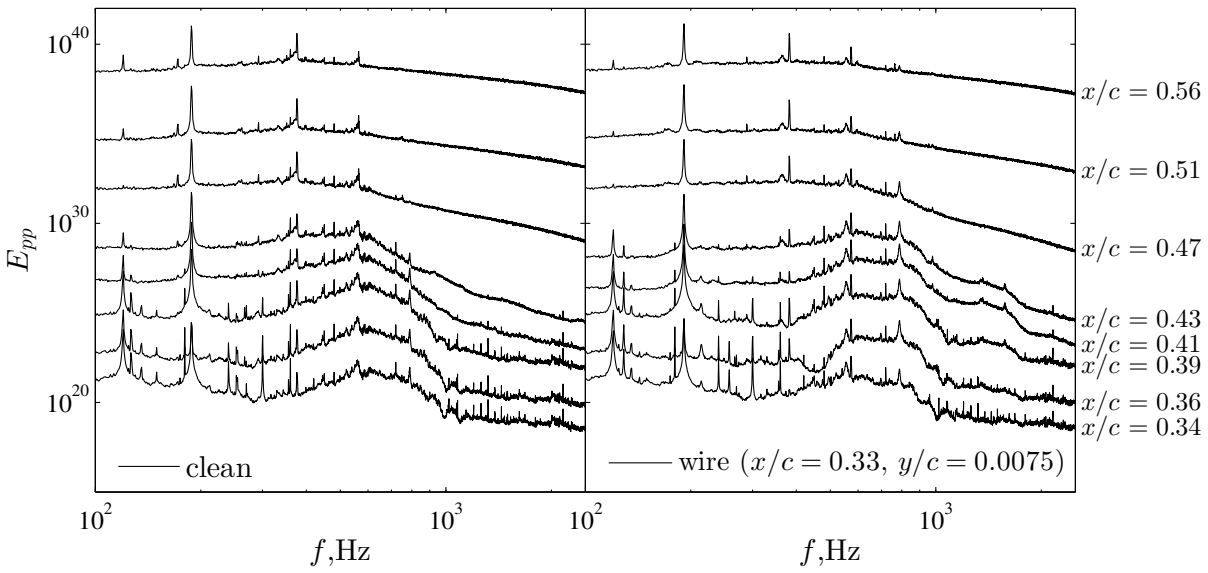
(a) $\alpha = 0°$ (b) $\alpha = 5°$

(c) $\alpha = 8°$ (d) $\alpha = 10°$

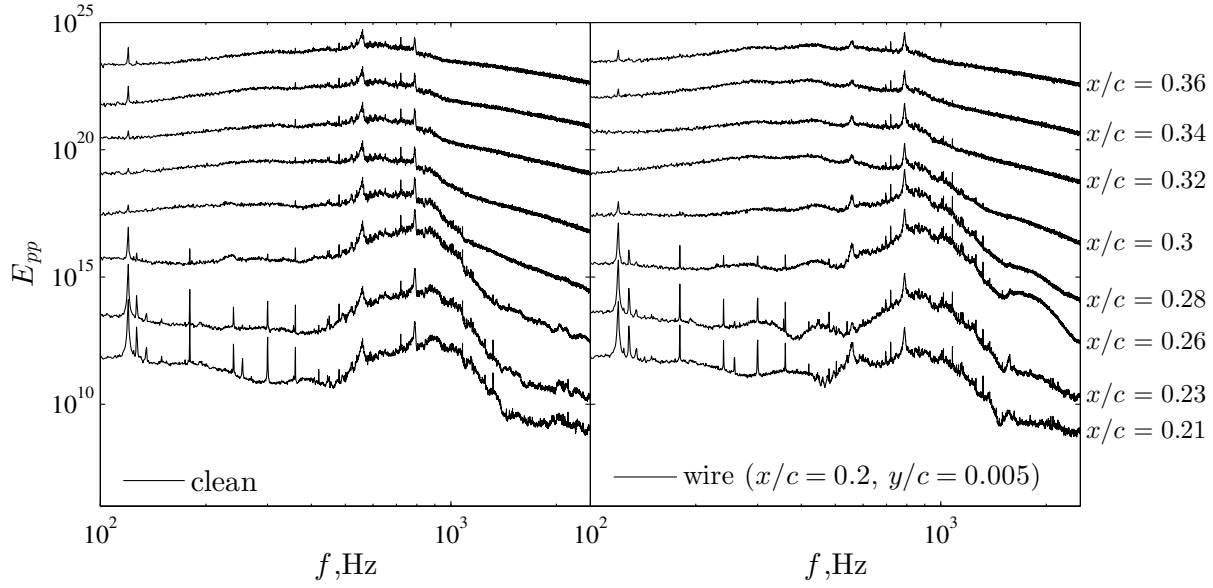
Figure B.2: Streamwise development of RMS fluctuating surface pressure, p'/q_∞, acquired with the airfoil fitted with just end caps and with the smoke-wire placed within the separated shear layer over the airfoil.



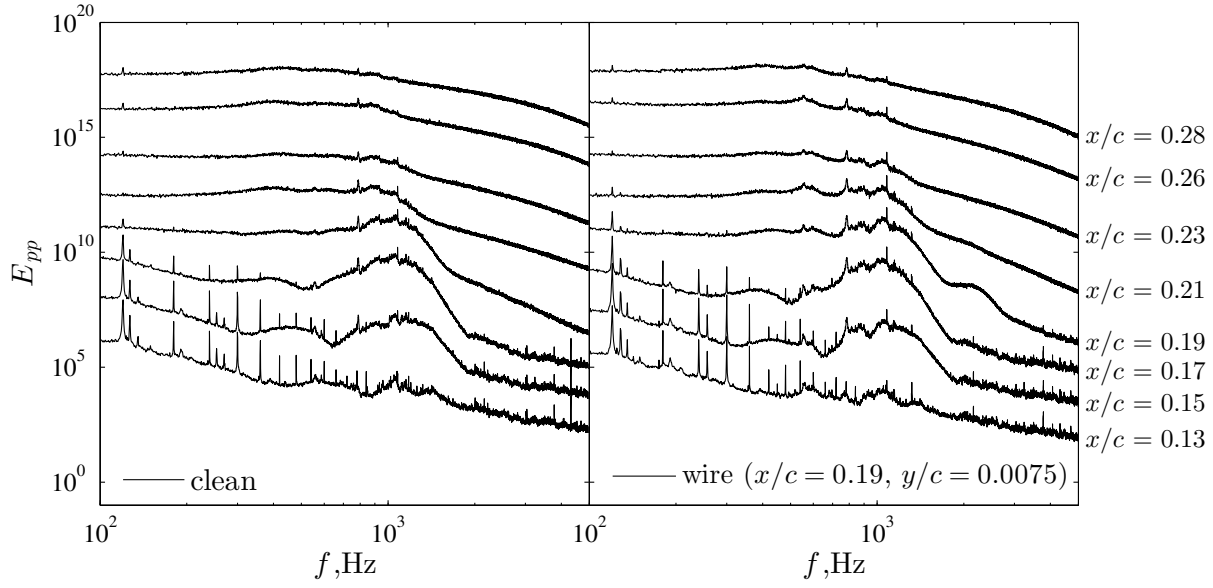
(a) $\alpha = 0°$



(b) $\alpha = 5°$



(c) $\alpha = 8°$



(d) $\alpha = 10°$

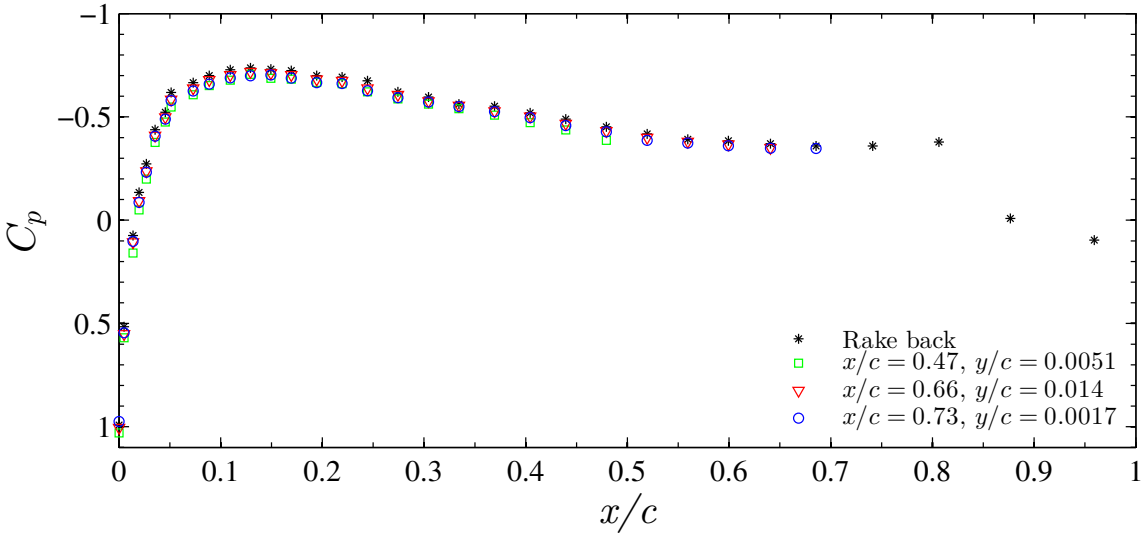
Figure B.3: Fluctuating surface pressure spectra computed from signals acquired with the airfoil fitted with just end caps and with the smoke-wire placed within the separated shear layer over the airfoil.

B.2 Intrusiveness of Velocity Measurements

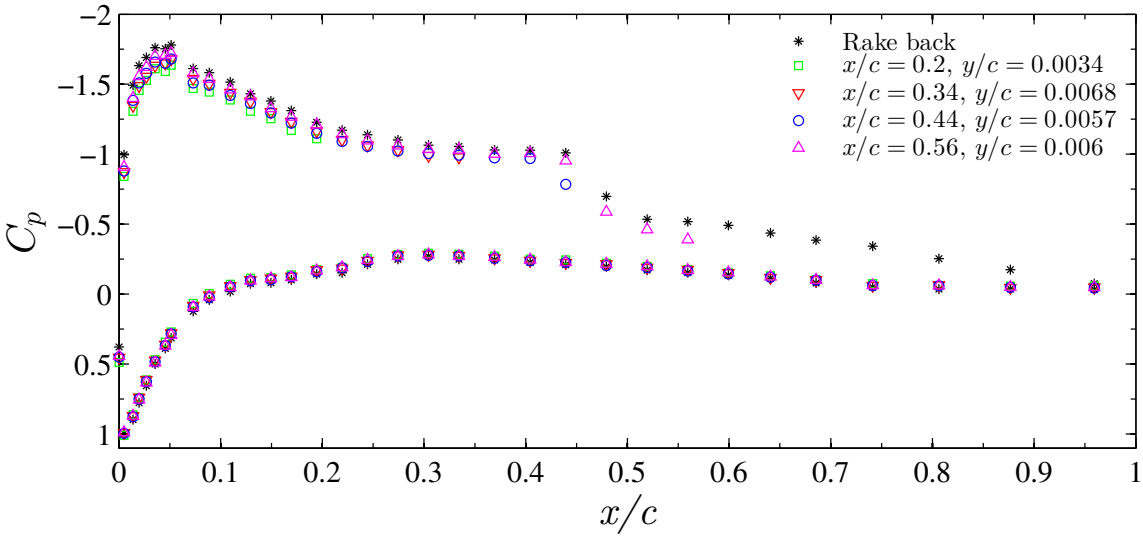
The intrusiveness of the rake of hot-wire probes on the flow was studied via surface pressure distributions and microphone measurements performed with the rake placed within the boundary layer. The measurements were performed with end plates mounted on the airfoil model (Fig. 3.2a).

Figure B.4 presents surface pressure distributions acquired with the rake placed at streamwise locations within or near the separation bubble at δ^* compared to surface pressure distributions acquired with the rake towards the back of the wind tunnel. The distributions have only been plotted up to the streamwise position of the rake, as the main concerns regarding intrusiveness lie with the upstream development of the flow. At $\alpha = 0°$, inserting the rake has a minor effect on the surface pressure distributions and causes the mininum pressure to increase by approximately 5%. At $\alpha = 5°$, the plots show that placing the rake near separation $x/c = 0.34$) appears to shift the beginning of the pressure plateau slightly upstream. Placing the rake near transition ($x/c = 0.44$) causes the end of the plateau, where the mean transition location is estimated, to also shift upstream. Placing the rake near reattachment ($x/c = 0.56$), causes an increase in the surface pressures beyond $x/c > 0.4$, indicating that there is a slight effect on the flow past transition. At this angle, the magnitude of the surface pressure within the separation bubble increases by approximately 10%. At $\alpha = 8°$, placing the rake within the separation bubble causes the surface pressure to also increase by approximately 10%. The surface pressure distributions at these angles indicate that while the rake does have an effect on the flow, it is minor and does not affect the overall shape of the distributions. This is not the case at $\alpha = 10°$ (Fig. B.4 d), where placing the rake within the separation bubble ($x/c = 0.16$) alters the surface pressure distribution dramatically, which is why velocity measurements were not performed at this angle of attack. Further downstream, within the separation bubble and past reattachment, the profiles are not as affected. This suggests that placing the rake further upstream towards separation has a larger effect on the flow at this angle of attack. The changes observed in the surface pressure distributions at these angles of attack are consistent with the results of Boutilier [43], who observed similar behaviour and increases in the surface pressure of a similar magnitudes while testing the intrusiveness of a single boundary layer hot-wire probe. Boutilier [43] also observed that placing a hot-wire probe near the separation point has large effect on the flow at $\alpha = 10°$.

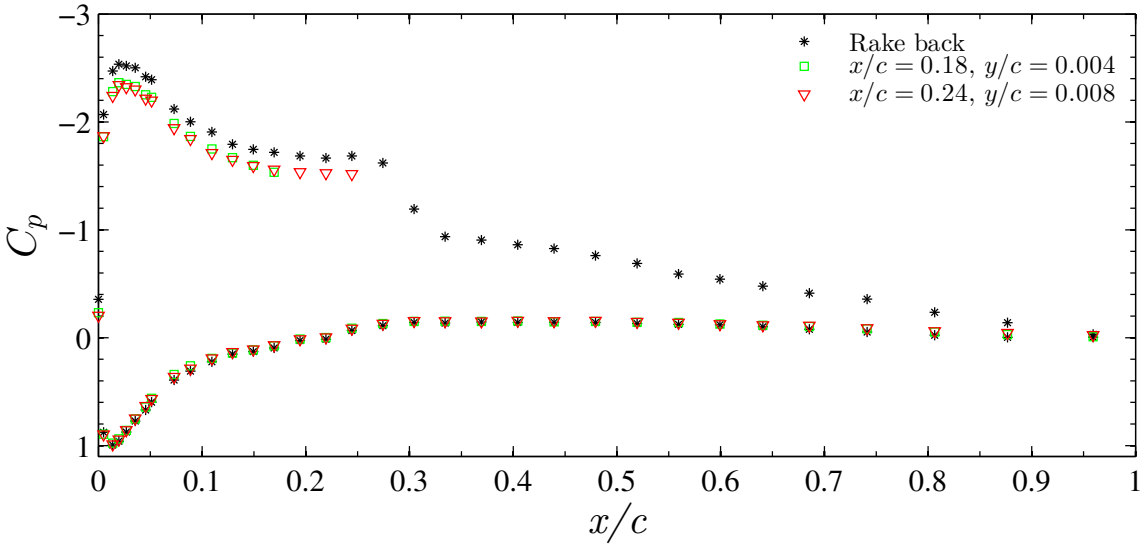
Figure B.5 presents fluctuating surface pressure spectra obtained at $\alpha = 5°$ with the rake positioned within the separation bubble boundary layer at δ^*. The spectra have been normalized such that their energy content is unity and have been scaled proportional to $10^{x/c}$ for clarity. The figure shows that placing the within the boundary layer has a negligible effect on the frequency distribution of the energy content of microphone signals acquired



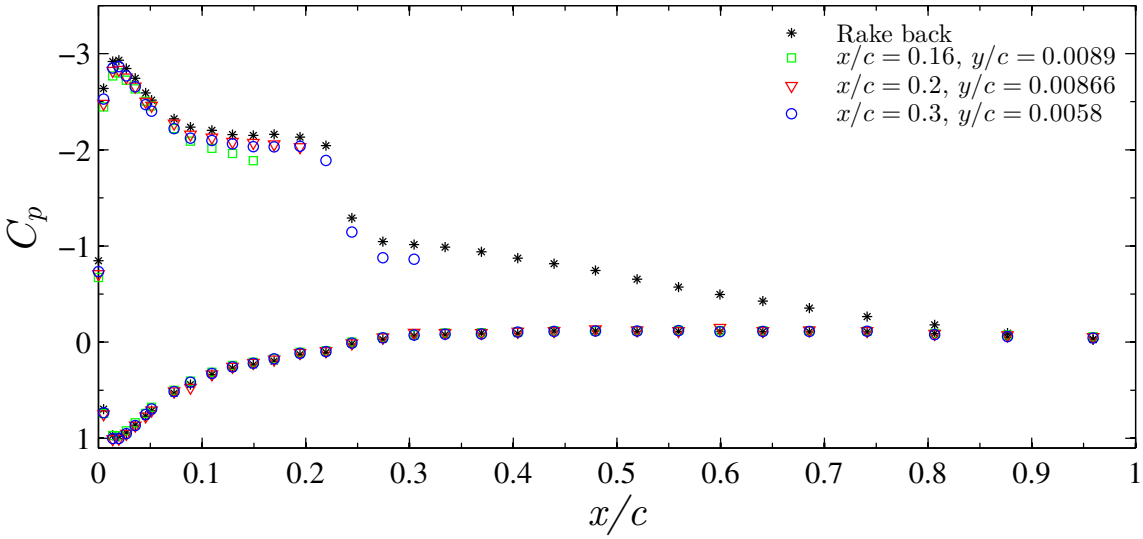
(a) $\alpha = 0°$



(b) $\alpha = 5°$



(c) $\alpha = 8°$



(d) $\alpha = 10°$

Figure B.4: Influence of rake of hot-wire probes on surface pressure distributions when placed within the boundary layer. The legends in each plot indicate the streamwise and vertical position of the rake of hot-wires.

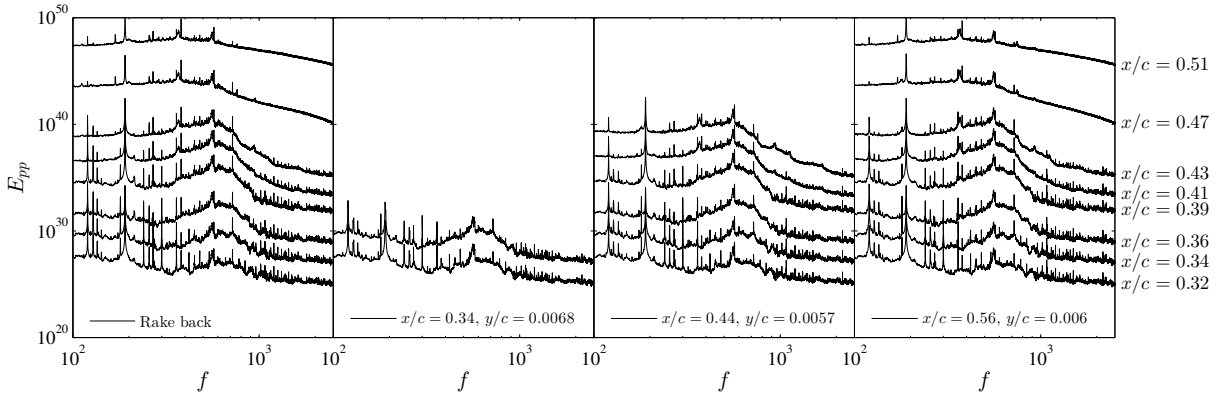


Figure B.5: Influence of the rake of hot-wire probes on fluctuating surface pressure spectra when placed within the boundary layer at $\alpha = 5°$. The legend in the plot indicates the streamwise and vertical position of the rake of hot-wires.

upstream of the rake. This shows that the rake does not have a large effect on the scale and frequency band of the disturbance growth that occurs within the separated shear layer.

B.3 Effect of Wind Tunnel Free-stream

The results of this investigation have shown that low-frequency peaks near $f = 190$ Hz are contained within the energy spectra at $\alpha = 5°$ (Fig. 4.27). Also, a peak at a similar frequency is visible within the unstable disturbance frequency band at $\alpha = 0°$ (Fig. 4.26). In Section 4.2.4, the separated shear layer was shown to have a component of flapping at this frequency at both angles. Experimental studies on airfoils have shown that the free-stream disturbances may causes the separated shear layer to flap at a similar frequency [10, 20].

To verify whether fluctuating within free-stream at a similar frequency may be causing these peaks, velocity measurements were acquired within the free-stream in an empty test section at $X/c = 0$ with the tunnel set such that velocity was $U/U_\infty = 1$, where U_∞ is the free-stream velocity required for a chord Reynolds number of $Re_c = 10^5$ over the airfoil model. Also, to verify whether the wind tunnel generator may be forcing the flow acoustically, measurements were also taken with the fan off. Figure B.6 shows fluctuating velocity spectra obtained with the wind tunnel free-stream velocity set to $U/U_\infty = 1$ and with the wind tunnel fan off. The spectra have each been normalized by the energy content and shifted for clarity. The figure shows that free-stream measurements contain peaks below

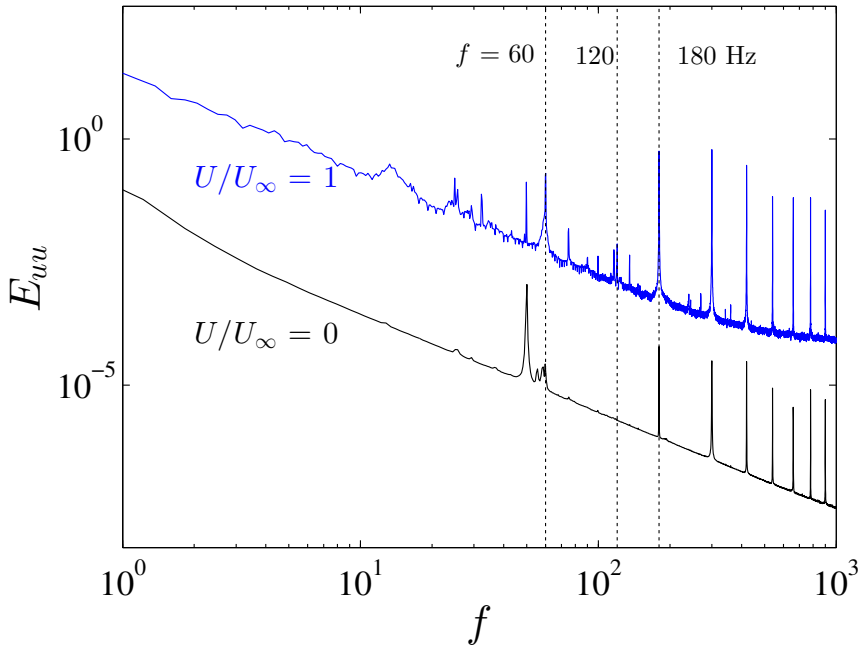


Figure B.6: Spectra of hot-wire velocity measurements obtained within the free-stream of the empty test section and within the test section with the fan off.

$f < 100$ Hz, which correspond to electrical noise and the blade-pass frequency of the fan. A peak is visible at $f = 60$ Hz, and at harmonics of this frequency, including $f = 180Hz$. In the measurements performed with the wind tunnel off, a similar peak appear at $f = 180$ Hz. Since a peak appears at 180 with the fan off, and does not match the blade-pass frequency near operation, the source of this frequency content is deemed unrelated to the fan, and likely caused to noise sources (e.g. electrical). Further testing with farfield acoustic forcing at $f = 180Hz$ (i.e. speaker) performed on a stationery hot-wire with the wind tunnel fan off, confirmed that peaks within the spectrum of measurements acquired with the fan off are unrelated to external noise sources. Further tests were performed to check whether tonal noise off the airfoil trailing edge may cause these peaks to appear. These tests investigated the energy content within the flow after tripping the pressure side of the airfoil. The results suggest that tonal noise is not the cause and as a result, this phenomenon requires further investigation.